Computational Modeling of DLR Micro Gas Turbine Spray Burner

Report Number: 2789

Sagar Kulkarni

TUDelft
Delft
University of
Technology

Challenge the future
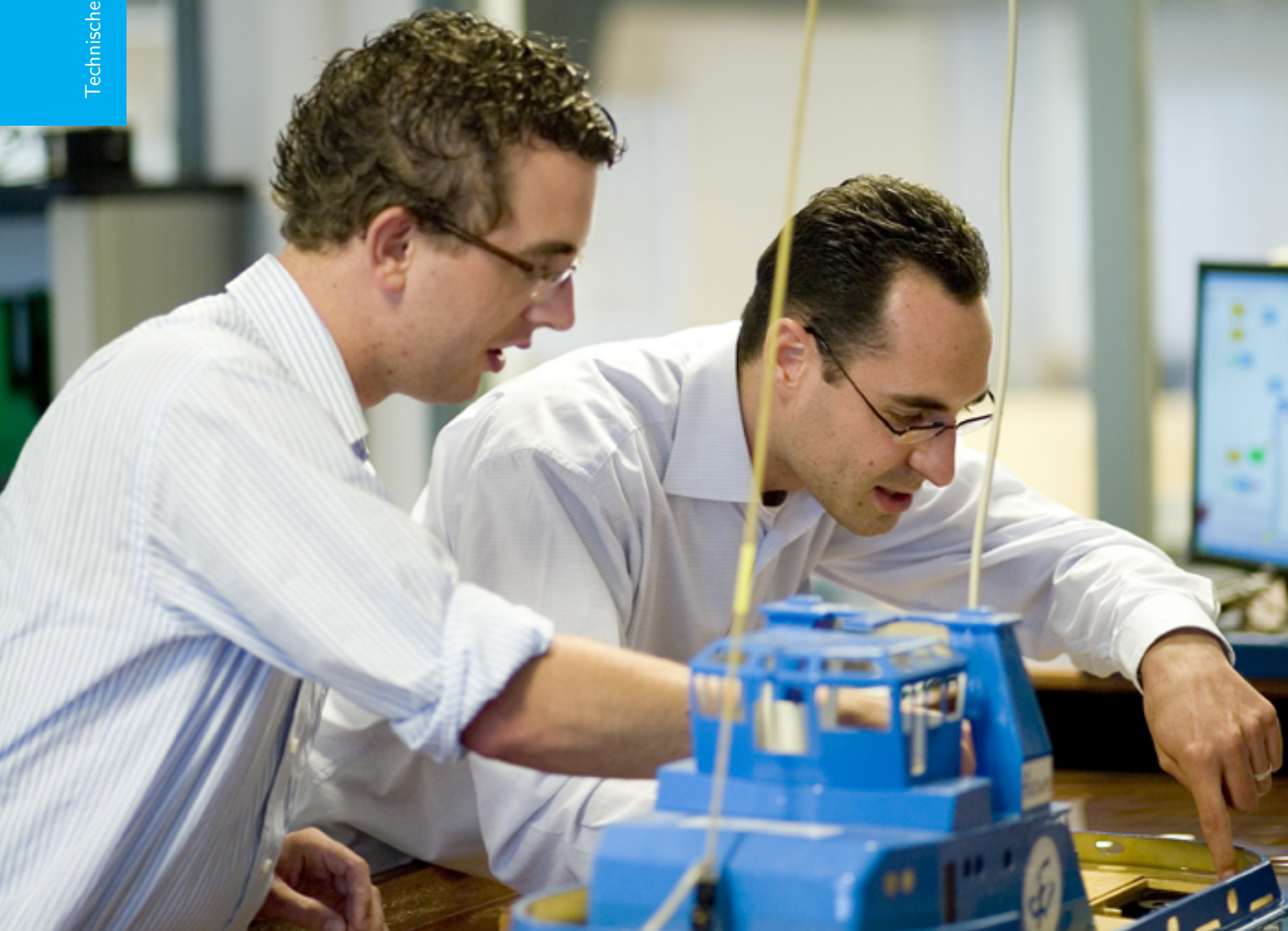
Computational Modeling of DLR Micro Gas Turbine Spray Burner

Report Number: 2789

by

Sagar Kulkarni

in partial fulfillment of the requirements for the degree of

Master of Science

in Mechanical Engineering

at the Delft University of Technology,

Student number:	4419014	
Supervisor:	Prof. dr. D. J. E. M. Roekaerts,	TU Delft
Thesis committee:	Dr. ir. R. Pecnik,	TU Delft
	Dr. A. Gangoli Rao ,	TU Delft
	Dipl.-Ing. M. Rachner,	DLR Institute of Combustion Technology

An electronic version of this thesis is available at http://repository.tudelft.nl/.

TUDelft Delft
University of
Technology

ACKNOWLEDGMENT

ABSTRACT

The current automobile industry is undergoing a paradigm shift from the conventional internal combustion engines to electric vehicles. Electro mobility is a greener alternative compared to the conventional engines. But one of the negative factors for the demand of electric cars is the maximum range which they can offer in a single battery charge. To extend the maximum range of electric cars Micro Gas Turbines are used due to their small size, better performance and lower emission compared to their internal engine counterparts. The automobile industry as any other industry is governed by stringent emission norms and to adhere to these emission levels, Flameless Oxidation (FLOX) combustion technology is employed. In this kind of combustors FLOX type of combustion is achieved based on high internal flue gas recirculation that is driven by high momentum of the air and fuel jet entering the combustion chamber. By doing so the chemical reactions are delayed and the combustion is rather distributed over a large volume leading to lower peak temperatures and NO_x emissions. This concept has been applied on conventional gas turbines however the application of this to a liquid fueled Micro Gas Turbine offers additional challenges which affects the physical processes of atomization, evaporation, fuel/air mixing etc. The objective of this thesis is to investigate these effects computationally and validate it against the experimental data measured at a DLR (German Aerospace Center) test facility to gain better understanding of the underlying physics.

Experimental data are available for a model combustor at DLR Stuttgart on light heating oil. Spray characteristics have been measured which in this study are used for validation of the combination of CFD models for turbulence, combustion and dispersed liquid phase flow. CFD results for droplet size, velocity, volume flux are compared against the measurements and additionally temperature and other flow characteristics are computed that are not measured which helps in developing further insight into the combustion process inside the burner. Further additional CFD simulation is done with higher air preheat temperature to study its effect on the combustion process.

For the validation study in this thesis, 3D steady state Reynolds-Averaged-Navier-Stokes (RANS) Eulerian-Lagrangian simulations are performed where gas phase computations are performed within Eulerian framework and dispersed phase is treated in Lagrangian framework. Two different combustion models are used: combined Eddy Dissipation and Finite Rate Chemistry (ED/FR) and Eddy Dissipation Concept (EDC). These combustion models are used with two different turbulence models of Reynolds Stress Model and Shear Stress Transport turbulence models with various other models for modeling dispersed phase. It was observed that the combined ED/FR model predicted early spatial heat release leading to inaccurate droplet velocity predictions while EDC model predicted proper heat release leading to better prediction of velocity profiles. Further, the applicability of Flamelet approach was investigated through Flamelet Generated Model (FGM) and Steady Flamelet Model (SFM). While SFM predicted combustion much upstream of the combustion chamber, FGM model predicted proper reaction zone. However, the FGM model predicted early spatial heat release due to the prediction of near equilibrium chemical time scales as the Damköhler number is close to unity. Further effects of turbulent two-way coupling are investigated and are found to be important. Radiation is found to have only a minor role in this case.

CONTENTS

LIST OF FIGURES

LIST OF TABLES

1

INTRODUCTION

The current population is said to increase from 6 billion to 10 billion in the coming 50 years and with that the vehicle population is said to increase from 700 million to 2.5 billion [5]. If all these vehicles will be propelled by Internal Combustion Engines running on conventional fuels which is said to be depleted by 2038 with the current trend of oil discovery and consumption [6] then the future of earth would be grim. This situation has compelled the research community to find greener solutions for transportation industry. Worldwide, according to the recent statistics of International Energy Agency (IEA), of the total world oil consumption, a whopping 63.8% is consumed by the transportation sector in 2013, an increase from 45.4% in 1973 [1] as shown in fig. 1.1. According to the International Energy Outlook published by the Energy Information Admin-
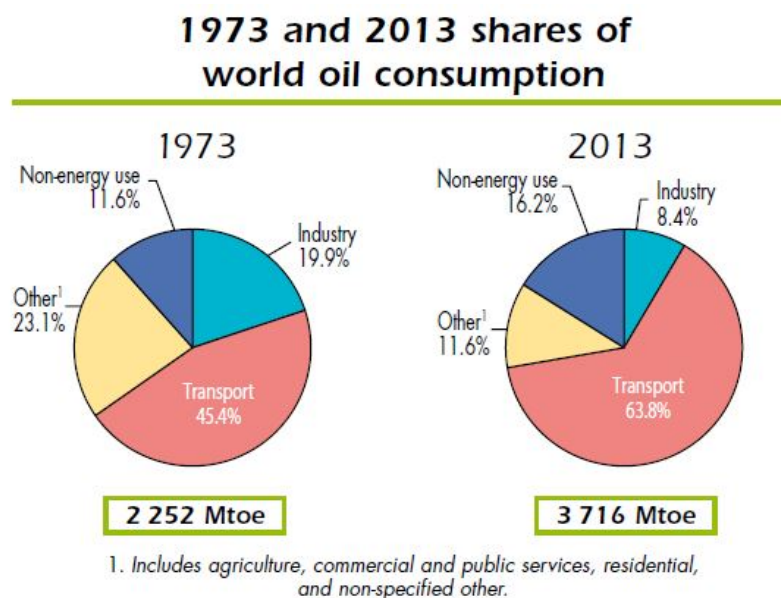
Figure 1.1: Sector wise oil consumption [1]

istration, USA, the contribution of liquid petroleum fuels including biodiesel is set to be still the dominant source of energy for transportation sector in the future [7]. Dwindling oil resources and rise in demand of petroleum fuels calls for a search of non-petroleum, greener solution. With regards to addressing this issue,

1

people have switched their attention from ICE to Electric Vehicles (EV) which are greener and efficient and this is slowly manifesting in people buying plug-in electric vehicles. However, the range of modern electric vehicles is limited and to give a perspective, the Tesla Model S 85D's range is 270 miles with one complete battery charge [8]. Thus in order to enhance the range a MGT (Micro Gas Turbine) on board can be used to recharge the battery as proposed by companies involved in this business which should have low emissions and better performance [9]. One such MGT range extender which is built by Bladon Jets, UK is shown in Fig. 1.2. Gas Turbines working at most efficient point produce lower emissions as compared to IC engines and also the weight of the MGT for same power specification is less compared to ICE [10]. Hence a MGT combustor which produces low emission and is fuel flexible is studied in this thesis.

Figure 1.2: Micro Gas Turbine by Bladon Jets, UK

1.1. EXPERIMENTAL SETUP

The stationary and propulsion gas turbines of today's generation are subject to stringent emission norms without compromising on the efficiency and performance of the systems itself. This has led to the use of lean premixed combustion technology which offers benefits of lower NO_x emissions compared to nonpremixed combustion [11]. In most of these cases the flames are aerodynamically stabilized by swirl which are susceptible to thermo-acoustic instabilities and sensitive to the fuel composition changes and risk of flashback are some of the limitations for a safe and reliable operation [2].

On the other hand gas turbines based on Flameless Oxidation principle (FLOX) have proven to be an alternative for reliable, fuel flexible and low emission combustors [12, 13]. The combustion process in the current combustor does not completely meet the characteristics of flameless oxidation due to its high power density and higher adiabatic flame temperatures. However, the FLOX term denotes a certain model type of gas turbine burner which offers benefits of low emissions and fuel flexibility [2, 12, 14]. This type of combustor is characterized by high momentum jets which are discharged through the orifices arranged on a circle into the combustion chamber. The axial momentum jets provide distinct recirculation in the combustion chamber as

shown in the work of Lammel et al. in Fig. 1.3. This leads to intense mixing of burnt gases with fresh fuel-air mixtures and thus stabilizes the flame.
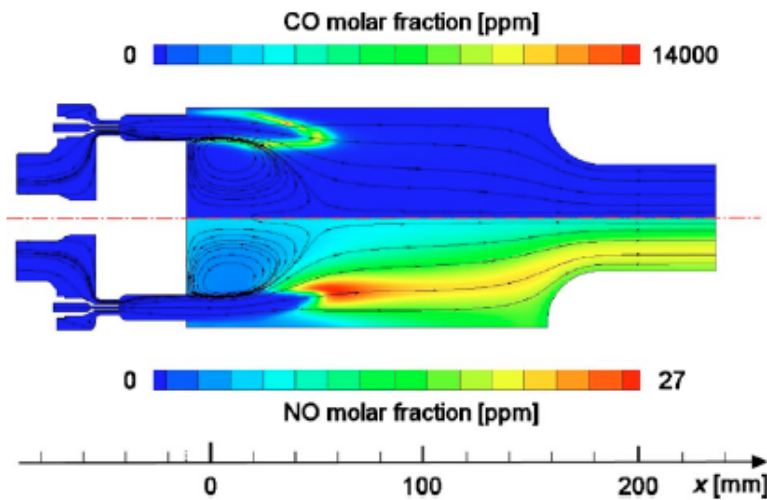
Figure 1.3: FLOX based combustor showing CO and NO molar fraction distribution with streamlines representing the flow [2]

The liquid FLOX burner which is based on the earlier work of Zizin et al. [15] was specifically designed to be tested at the High Pressure Optical Test Rig (HIPOT) at DLR Stuttgart. The burner was designed to operate at a thermal power load of 155 kW at 3.5 bars operating pressure corresponding to electric power output of 48 kW_{el}. Fig. 1.4 shows the sectioned view of the burner in the yz plane taken in the middle of the combustion chamber. The liquid FLOX burner consists of 8 nozzles equally spaced on a circle of radius 34 mm as shown in the figure. The diameter of each nozzle is 7 mm and each nozzle is equipped with a pressure atomizer from Steinen (0.25−45°) GPH MST MICRO-FLO mounted 139 mm upstream of the nozzle exit plane as shown in the Fig. 1.5. Fig. 1.5 shows the main parts involved: the injector, the mixing chamber where the inlet preheated air mixes with the atomized fuel, mixing tube and finally the combustion chamber where combustion occurs. The preheated air enters the plenum and the atomized fuel from each injector is carried by stream of preheated air through a contraction into the mixing tube for respective nozzle before entering the combustion chamber. In the Fig. 1.5 the contraction part upstream of the mixing tube is not shown as the design is under patent application and with the grant of patent, the design will be made public. The inlet section of the nozzle also has some holes which pick up the main air and create a thin film of air along the nozzle walls. The fuel used in this study is light heating oil and the differences between diesel and light heating oil were found to be small [16]. The operability limits of the burner at 3.5 bars operating pressure was carried out in previous study by Gounder et al. [16] and one of the BOP (Burner Operating Point) has been chosen for detailed experimental and numerical analysis. The initial conditions of the BOP is given in table 1.1 and this will be referred to as the test case in this study hereafter.

In this study, only the spray measurement over nozzle 6 was made using a point measurement method: Phase Doppler Interferometry (PDI) to obtain droplet size and velocity at different axial locations in the combustion chamber which are demarcated in Fig. 1.5. In the Fig. 1.4 it can also be seen that the planar measurement technique of Particle Image Velocimetry (PIV) was also used on nozzles 5 and 8. In the experiments it was observed that the radial profiles of the axial velocity at different axial locations were in good agreement with the bulk velocity of the test case of 120 m/s when measured with PIV on nozzle 5 and 8 and with PDI on nozzle 6. For numerical model validation the spray data obtained from the PDI measurement over nozzle 6 will be used. Fig. 1.6a shows the mean OH^* chemiluminescence of different nozzles and Fig. 1.6b show the
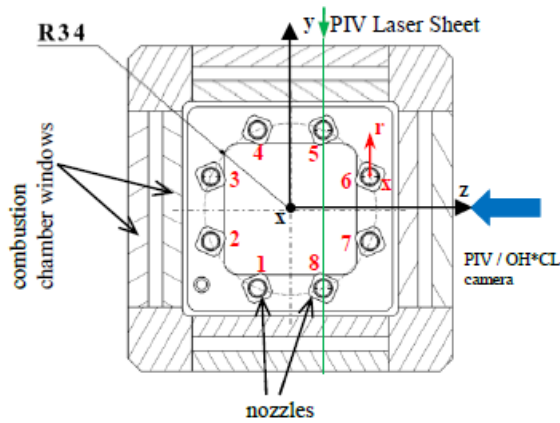
Figure 1.4: View of combustion chamber in xz plane showing the arrangement of the nozzles
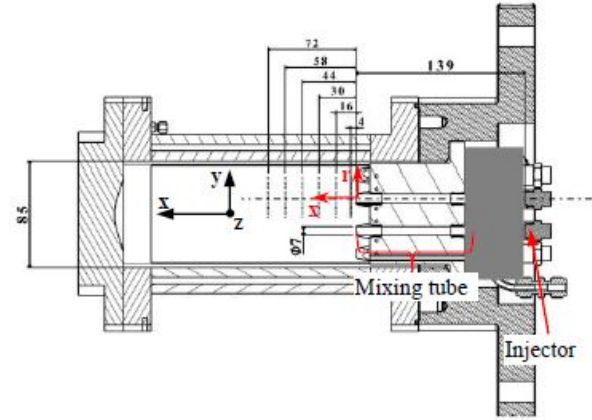
Figure 1.5: Sectioned view of combustion chamber in xr plane across nozzle 6 and 7 showing the PDI measurement locations

Table 1.1: Boundary Conditions for nozzle 6

Parameter	Value
Pressure (bar)	3.5
$T_{air}(K)$	573
λ_G	1.45
$V_{bulk}(m/s)$	120
$P_{th}(kW)$	186
$T_{fuel}(K)$	310
Fuel mass flow rate over 8 nozzles (g/s)	4.3
Air mass flow rate over 8 nozzles (g/s)	91.4

rms image of Mie signal from spray particles exiting nozzles 5 and 8. From mean OH^* image it is visible that the flame stabilizes close to the nozzle exit plane and the length of flame covers almost two third of combustion chamber length. No temperature measurements were made in the combustion chamber. It should be mentioned here that no temperature measurements were made and also no gas phase velocity measurements were made.

1.2. OBJECTIVE OF THE WORK

As seen from above, numerous works have been carried out on FLOX based combustors with gaseous fuels for generic gas turbines. But, implementing liquid fueled FLOX based combustor to Micro Gas Turbine (MGT) poses additional challenges as MGT's are not well equipped to operate in low emission regime with liquid fuels. With the use of liquid fuels the small size constraint of MGT brings problems to physical processes of atomization, evaporation and fuel-air mixing in the combustion chamber. With the completion of liquid fuel FLOX based MGT design at atmospheric pressure, further development of this combustor at high pressure application requires deeper understanding of the underlying phenomena of fuel-air mixing, temperature distribution etc. With this work, the available numerical models for various physical phenomena are validated against the experimental data which are measured at DLR test facility in Stuttgart, Germany and as a result the unmeasured quantities of interest such as temperature field, recirculation zones, cooling air distribution and effect of air preheating temperature are obtained which will aid in the development of the burner. The validation study leads to the study of following points in this work.
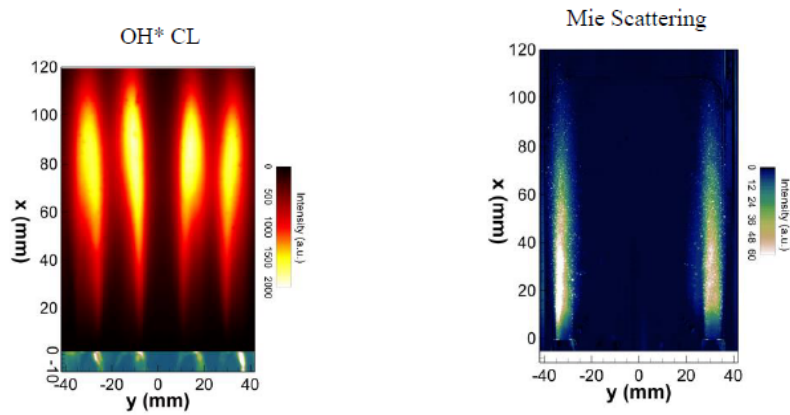
(a) Mean OH^* chemiluminescence signal

(b) RMS image of Mie signal from spray droplets exiting nozzles 5 and 8

- Importance of combustion models to model this type of combustors

- Accuracy of turbulence models

- Modeling of drop size distribution function for spray boundary conditions in CFD simulation

- Problems with the current numerical models to predict the proper physics

In order to achieve the objective the turbulent spray combustion CFD simulation is carried out in two different commercial codes: ANSYS CFX and ANSYS FLUENT. In the first stage of this thesis, the simulations will be carried out with gas phase code of ANSYS CFX-16 and the liquid phase simulation code- SPRAYSIM. The SPRAYSIM-code is the development platform of the DLR Institute of Combustion Technology for unsteady or steady Lagrangian particle simulation. A brief description will be given in chapter 3 In the second stage, the commercial code of ANSYS FLUENT-16 is used for both gas phase and liquid phase simulation. The computational approach is quite similar to the ANSYS CFX - SPRAYSIM combination. The Lagrangian tracking of droplets is done by FLUENT itself and the droplet parcel raw data which is captured at desired registration planes are then processed in SPRAYSIM postprocessing tool to obtain quantities of interest. The main difference with the combination of CFX - SPRAYSIM and FLUENT is present mainly in the combustion modeling which is discussed in this work.

Hereafter, the work carried out in this thesis is delineated. Chapter 2 reviews the theory behind the various numerical models related to modeling of turbulence, combustion, radiation and liquid phase. In subsequent chapters the application of these models to predict the experimental observations is presented and the results are deliberated to understand the reasons behind the obtained results. Finally, some conclusions are drawn and recommendations based on this work are given.

2

COMPUTATIONAL MODELS

Turbulent reacting flows is an ensemble of various fluid dynamic phenomenon including one or more of the following: turbulence, combustion, radiation heat transfer and acoustic instabilities. As such the scales involved in the flow are widely different and has to be captured in order to understand the physics behind the turbulent combustion. Further, turbulent spray combustion adds additional physical processes such as atomization, droplet dispersion, evaporation which change the turbulent reacting flow phenomena. Robust computational models are required to properly describe and mimic these processes.

Turbulent numerical simulations can be broadly classified into: Reynolds Averaged Navier Stokes simulation popularly known as RANS simulations, Large Eddy Simulation (LES) and Direct Numerical Simulation (DNS) depending on the resolution of grid and how the turbulence is modeled. The main focus in this thesis work is RANS simulation and thereby turbulence modeling is one of the key issues in the simulations. In this work, various turbulence models are used namely: $k - \epsilon$, $k - \omega$ based Shear Stress Transport (SST) and Reynolds Stress Model.

Then, the next thing is the modeling of chemical reactions and their interaction with the turbulence present in the flow. This is achieved through combustion models. In this work, different combustion models are discussed: Eddy Dissipation Model combined with Finite Rate Chemistry (EDM/FRC), Eddy Dissipation Concept (EDC), Steady Diffusion Flamelet (SFM) and Flamelet Generated Manifold (FGM).

Radiation heat transfer can be an important important phenomena at high temperatures which are experienced in these kind of combustion devices. Radiation can affect the temperature field and hence the other processes such as evaporation, flame structure which depend on temperature. In this section brief description is given about the modeling of radiation heat transfer which will be used in this work to assess the effect of radiation.

The liquid phase modeling involves the atomization of the bulk liquid into droplets, evaporation of the droplets and the droplet dispersion which is due to the turbulence in the flow. In this work, the atomization process is not taken into account as the flow physics of injectors used in gas turbine configuration is very expensive to calculate[17, 18] and thus an injection model is used instead which provides the necessary boundary conditions for CFD simulations. In certain cases, there might be secondary breakup of the droplets due to the higher aerodynamic Weber number and this is modeled by secondary atomization models. After the droplet injection, the droplets are heated and undergo an evaporation process where mass transfer from the liquid phase to gas phase and energy from gas phase to liquid phase occurs. This reduces the local

gas phase temperature. Along with heat and mass transfer, the momentum transfer from liquid phase to gas phase occurs through droplet drag force. The evaporated fuel then mixes with the oxidizer and then burns. While, mass, momentum and heat is being exchanged with the gas phase, in turbulent flow the droplets modify the mean gas field and modulate turbulent scales and in turn the gasfield has strong influence on the droplet motion, heating and evaporation. This is known as the turbulent two way coupling and changes the flow physics significantly. All the models from injection to evaporation and combustion used in this work are explained in this chapter.

In the following sections, the governing equations for the gas phase are given and the closure of these equations: turbulence models, turbulence-chemistry interaction models are discussed. Finally, the liquid phase governing equations are treated and various processes of liquid phase modeling which are mentioned above are also discussed.

2.1. GOVERNING EQUATIONS

The natural starting point to solving any fluid dynamics (non-reacting) related problems is the solution of the governing equations namely mass and momentum conservation which are enough to describe the flow without any heat transfer. This would already result in solution of 4 Partial Differential Equations (PDE) (3 momentum and 1 mass conservation). In addition, if there is heat transfer at play then an additional PDE has to be solved for energy conservation. Hence 5 partial differential equations have to be solved for a spatially 3 dimensional problem.

In reacting flow, chemical species are present and chemical components conservation is accounted for by solving the transport equations for species mass fractions which is defined as $Y_k = \rho_k / \rho$ where ρ_k is the mass density of the species k. The density of the mixture is the summation of the densities of various species in the mixture $\rho = \sum_{k=1}^{N_s} \rho_k$ and N_s is the number of species present in the gas mixture. In reacting flows, in total $N_s + 5$ equations have to solved in order to completely describe the system. The instantaneous balance equations for mass, momentum, energy and species are given below:

$$\frac{\partial \rho}{\partial t} + \frac{\partial (\rho u_j)}{\partial x_j} = S_\rho^v \tag{2.1}$$

$$\frac{\partial (\rho u_i)}{\partial t} + \frac{\partial (\rho u_i u_j)}{\partial x_j} = -\frac{\partial p}{\partial x_i} + \frac{\partial}{\partial x_j} \left[-\mu \left(\frac{\partial u_i}{\partial x_j} + \frac{\partial u_j}{\partial x_i} + \frac{2}{3} \mu \frac{\partial u_m}{\partial x_m} \delta_{ij} \right) \right] + \rho g_i + S_{u_i}^v \tag{2.2}$$

$$\frac{\partial (\rho h)}{\partial t} + \frac{\partial (\rho h u_j)}{\partial x_j} = \frac{Dp}{Dt} - \frac{\partial q_j}{\partial x_j} + \tau_{ij} \frac{\partial u_i}{\partial x_j} + Q + S_h^v \tag{2.3}$$

$$\frac{\partial (\rho Y_k)}{\partial t} + \frac{\partial (\rho Y_k u_j)}{\partial x_j} = -\frac{\partial J_{k,j}}{\partial x_j} + \dot{\omega}_k + S_{Y_k}^v \tag{2.4}$$

In equations 2.1- 2.4 the Einstein summation convention is observed where the sum is taken over the repeating indices. ρ, u, Y, h is the density, convective velocity, mass fraction and enthalpy respectively and these are the unknowns which are solved for. Index k denotes the number of the species and index i denotes the spatial directions. p is the pressure, second term on RHS of eqn. 2.2 is the stress tensor. The bulk viscosity (μ_v) is assumed to be zero[19]. g is the acceleration due to gravity (body force). Heat flux q_j in eqn. 2.3 takes into account the heat transfer through heat conduction and diffusion of species with different enthalpies. First and third term in the energy equation (eqn. 2.3) represents the pressure and viscous work. Q is the heat source term due to radiation or other sources. $\dot{\omega}_k = \rho S_k$ is the chemical source term which is defined as the

production (or consumption) of species k per unit volume per unit time. $J_{k,j}$ is the diffusion flux of species k. In the above equations the superscript "v" denotes the source terms due to the droplet evaporation. In further sections the method of solving this set of equations for turbulent flow will be explained. Finally, the relationship between thermodynamic variables is obtained through the assumption of multicomponent ideal gas and thermodynamic equilibrium at the liquid-gas interface. Equation of state is used which relates the two state variables say for example, ρ, T with other variables. Ideal gas equation of state is given by:

$$p = \rho R T \tag{2.5}$$

where $R = R_u/W$ is the gas constant and W is the mean molecular weight. $R_u = 8.314 J/(mol \cdot K)$ is the universal gas constant. In order to model turbulent reactive flows, RANS approach is followed as mentioned earlier. Typically in turbulent flows, local properties will have a mean value and a fluctuating part around this mean. By this principle, any property f can be split into two parts: $f = \bar{f} + f'$. By applying this to the instantaneous balance equations for constant density flows, following equations for mass and momentum are obtained.

$$\frac{\partial \overline{\rho}}{\partial t} + \frac{\partial \left(\overline{\rho u_j} \right)}{\partial x_j} = \overline{S}_{\rho}^{v} \tag{2.6}$$

$$\frac{\partial \left(\overline{\rho u_i} \right)}{\partial t} + \frac{\partial \left(\overline{\rho u_i u_j} \right)}{\partial x_j} = -\frac{\partial \overline{p}}{\partial x_i} + \frac{\partial \overline{\tau}_{ij}}{\partial x_j} + \overline{\rho} g_i + \overline{S}_{u_i}^{v} \tag{2.7}$$

In the eqn. 2.6 & eqn. 2.7 the average of products when expanded gives terms such as $\overline{\rho' u'}$ which are correlation of density and velocity fluctuations. In modeling reacting flows, where variable densities are encountered, the density and velocity fluctuation correlations are awkward to handle. Thus another approach is used where in these density fluctuations do not appear as the averaging is mass-weighted. This type of averaging is known as Favre averaging.

$$\tilde{f} = \frac{\overline{\rho f}}{\overline{\rho}} \tag{2.8}$$

Again, any quantity f can be split into mean and fluctuating quantity as:

$$f = \tilde{f} + f'' \tag{2.9a}$$

$$f'' = 0 \tag{2.9b}$$

Using this averaging technique following averaged conservation equations are obtained:

$$\frac{\partial \overline{\rho}}{\partial t} + \frac{\partial \left(\overline{\rho} \widetilde{u_j} \right)}{\partial x_j} = \widetilde{S}_{\rho}^{v} \tag{2.10}$$

$$\frac{\partial \left(\overline{\rho} \widetilde{u_i} \right)}{\partial t} + \frac{\partial \left(\overline{\rho} \widetilde{u_i} \widetilde{u_j} \right)}{\partial x_j} = -\frac{\partial \overline{p}}{\partial x_i} + \frac{\partial \overline{\tau}_{ij}}{\partial x_j} + \overline{\rho} g_i - \frac{\partial \left(\overline{\rho \widetilde{u_i'' u_j''}} \right)}{\partial x_j} + \overline{S}_{u_i}^{v} \tag{2.11}$$

$$\frac{\partial \overline{\rho} \widetilde{Y_k}}{\partial t} + \frac{\partial \left(\overline{\rho} \widetilde{Y_k} u_j \right)}{\partial x_j} = -\left[\frac{\partial \overline{J}_k}{\partial x_j} + \frac{\partial \left(\overline{\rho \widetilde{u_j'' Y_k''}} \right)}{\partial x_j} \right] + \overline{\dot{\omega}}_k + \overline{S}_{Y_k}^{v} \quad k = 1 \cdots N_s \tag{2.12}$$

$$\frac{\partial \overline{\rho} \widetilde{h}}{\partial t} + \frac{\partial \left(\overline{\rho} \widetilde{h} u_j \right)}{\partial x_j} = \frac{D \widetilde{p}}{Dt} - \frac{\partial}{\partial x_j} \left(\widetilde{q}_j + \overline{\rho \widetilde{u_j'' h''}} \right) + \overline{\tau_{ij} \frac{\partial u_i}{\partial x_j}} + \overline{Q} + \overline{S}_{h}^{v} \tag{2.13}$$

In eqn. 2.10 - eqn. 2.13 there are some unclosed terms which needs further modeling. In turbulent combus-

tion simulation closure of these equations is the main objective. The term $-\overline{\rho u_i'' u_j''}$ in eqn. 2.11 is known as Reynolds stress. Generally, Reynolds stresses represent the flux of momentum of ith component in the jth direction due to fluctuating velocity field caused by turbulence. Closure of Reynolds stress manifests into different turbulence models which will be discussed further in some detail. Terms $\overline{\rho u_j'' Y_k''}$ and $\overline{\rho u_j'' h''}$ represents the turbulent fluxes which are modeled using gradient diffusion hypothesis. The term $\overline{\dot{\omega}_k}$ represents the mean chemical source term and is the main subject of combustion models which deal with the closure of this term.

In the following sections different turbulence models are discussed which are used in this study. Further, the closure of turbulent scalar fluxes is discussed. Finally, the closure of the mean chemical source term is elucidated.

2.2. TURBULENCE MODELS

As seen earlier, the averaging process of instantaneous balance equations produces a new unclosed term in the momentum equation known as Reynolds Stress. In order to close this, either a model equation for every component of the Reynolds stresses themselves can be solved during computation or it can be modeled in a relatively simpler way. Firstly, the turbulence models based on eddy viscosity hypothesis are discussed. Then the Reynolds Stress Model (RSM) which works with anisotropic turbulence is discussed. Boussinesq made an hypothesis where the Reynolds stresses was written similar to molecular stress. By this the Reynolds stress can be modeled as:

$$\overline{\rho u_i'' u_j''} \equiv -\mu_t \left(\frac{\partial \tilde{u}_i}{\partial x_j} + \frac{\partial \tilde{u}_j}{\partial x_i} - \frac{2}{3} \frac{\partial \tilde{u}_k}{\partial x_k} \delta_{ij} \right) + \frac{2}{3} \overline{\rho} k \delta_{ij} \tag{2.14}$$

where μ_t is the turbulent dynamic viscosity which needs to be closed and k is the turbulent kinetic energy. Thus now the problem becomes finding a model to close the turbulent viscosity which is appearing in the eqn. 2.14. From dimensional analysis, it can be determined that the turbulent kinematic viscosity, ν_t has the dimensions of m^2/s. So, ν_t can be expressed as the product of velocity scale and length scale.

$$\nu_t = C \overline{\rho} \, \nu_t \, l_t \tag{2.15}$$

We see that, ν_t can be obtained once the velocity and length scales and the constant are determined. To obtain these quantities, extra transport equations have to be solved. Depending on the number of transport equations required the turbulence models are classified into zero, one or two equation models. In this work only two equation models: $k - \epsilon$ and $k - \omega$ based Shear Stress Transport models will be discussed.

2.2.1. K-EPSILON MODEL

$k - \epsilon$ is one of the most widely used two equation turbulence model. It has become the primary workhorse in modeling turbulence due to its robustness and reasonable accuracy for wide range of engineering problems. $k - \epsilon$ is based on eddy viscosity hypothesis and to close eqn. 2.15 two transport equations for k and ϵ are solved to obtain required velocity and length scale of turbulence. Transport equations for (k) and (ϵ) are shown below:

$$\frac{\partial}{\partial t} \left(\overline{\rho} k \right) + \frac{\partial}{\partial x_j} \left(\overline{\rho} k \widetilde{u_j} \right) = \frac{\partial}{\partial x_j} \left[\left(\mu + \frac{\mu_t}{\sigma_k} \right) \frac{\partial k}{\partial x_j} \right] + 2\mu_t S_{ij} \cdot S_{ij} - \rho \epsilon + S_k^d \tag{2.16}$$

$$\frac{\partial}{\partial t} \left(\overline{\rho} k \right) + \frac{\partial}{\partial x_j} \left(\overline{\rho} \epsilon \widetilde{u_j} \right) = \frac{\partial}{\partial x_j} \left[\left(\mu + \frac{\mu_t}{\sigma_\epsilon} \right) \frac{\partial \epsilon}{\partial x_j} \right] + C_1 \frac{\epsilon}{k} 2\mu_t S_{ij} \cdot S_{ij} - C_{2\epsilon} \rho \frac{\epsilon^2}{k} + S_\epsilon^d \tag{2.17}$$

where S_{ij} is the mean strain rate and it represents the generation of turbulence due to the mean velocity gradients in the flow. σ_k and σ_ϵ represent the turbulent Prandtl numbers for k and . $C_{1\epsilon}, C_{2\epsilon}, \sigma_k$ and σ_ϵ are empirical constants and have following values:

$$C_{1\epsilon} = 1.44 \quad C_{2\epsilon} = 1.92 \quad \sigma_k = 1.00 \quad \sigma_\epsilon = 1.30 \tag{2.18}$$

Turbulent viscosity is calculated according to eqn. 2.15 and the constant in the equation is given by $C = C_\mu = 0.09$. Finally, the terms: S_k^d & S_ϵ^d in eqn. 2.16 & eqn. 2.17 represent the source terms of the spray droplets present in the flow, to consider the effect of turbulence two way coupling which is described in liquid phase section 2.6.5.

2.2.2. SHEAR STRESS TRANSPORT (SST) MODEL

The two equation Shear Stress Transport (SST) was introduced by Menter [20] in 1994 to address the problem of predicting the onset and the amount of separation under adverse pressure gradient flows. The SST model in essence is a careful combination of the $k - \epsilon$ model and the $k - \omega$ model with blending function which makes use of the best elements of the two models. The $k - \epsilon$ model although it is successful in predicting large variety of flows suffers from lack of sensitivity under adverse pressure gradient flows [20, 21] due to the over-prediction of turbulent length scale which yields in large turbulent viscosity in the near wall region. Damping functions are introduced to contain the over-production of turbulent viscosity but the functions are numerically stiff and non-linear. On the other hand, another two equation eddy viscosity model: $k - \omega$ model solves for the turbulent kinetic energy and the large scale turbulence frequency ω. The model performs better in in the near wall region and does not employ damping functions. Nevertheless the $k - \omega$ model suffers from the problem of sensitivity to the free stream value of ω. Thus, Menter proposed a new baseline turbulence model which uses the $k - \omega$ formulation in the near wall regions and switches to the $k - \epsilon$ formulation in the free stream through a blending function. The blending function F_1 is multiplied with the terms of the $k - \omega$ model and $1 - F_1$ with the $k - \epsilon$ model terms and takes value of one near the wall and is equal to zero in free stream. Further, the main difference between Reynolds stress transport and other two viscosity models is that the former takes into account the transport of the principal turbulent shear stress $(-\rho \overline{u'v'})$ whereas the latter does not. In order to take into account the transport of principal shear stress, Menter [20] used the earlier observed finding that in a boundary layer shear stress is proportional to the turbulent kinetic energy.

$$\tau = \rho a_1 k \tag{2.19}$$

where a_1 = constant. While the conventional two-equation models calculate the shear stress as:

$$\tau = \mu_t \frac{\partial u}{\partial y} \tag{2.20}$$

Eqn. 2.20 can also be rewritten for the two-equation models as:

$$\tau = \rho \sqrt{\frac{\text{production}}{\text{dissipation}}} a_1 k \tag{2.21}$$

For adverse pressure gradient flows, the ratio of production to dissipation can be greater than one [20], which leads to over-prediction of shear stress. Thus in the framework of eddy-viscosity model, the turbulent viscos-

ity is redefined to satisfy eqn. 2.19 as follows:

$$v_t = \frac{a_1 k}{max\left(a_1\omega, \frac{\partial u}{\partial y}F_2\right)} \tag{2.22}$$

where F_2 is a function equal to one in boundary layer flows where production is greater than its dissipation and hence $\frac{\partial u}{\partial y} > a_1\omega$ and thus eqn. 2.19 is satisfied whereas $v_t = k/\omega$ is used for rest of the flow.

2.2.3. REYNOLDS STRESS MODEL (RSM)

Previously discussed two equation models are based on the eddy-viscosity hypothesis and therefore isotropic assumption of normal stresses is implied. But in many practical applications such as swirling flows this assumption does not hold well. RSM accounts for this anisotropy by solving the transport equations for Reynolds stresses by taking the moment of the exact momentum equation [21]. The transport equation is thus given as ($R_{ij} = \widetilde{u_i'' u_j''}$)

$$\frac{\partial}{\partial t}\bar{\rho}R_{ij} + \frac{\partial}{\partial x_k}\bar{\rho}R_{ij}\tilde{u}_j = D_{T,ij} + D_{L,ij} + P_{ij} + \Pi_{ij} + \epsilon_{ij} + M_{ij} \tag{2.23}$$

where $D_{T,ij}$ is the turbulent diffusion term, $D_{L,ij}$ is the molecular diffusion term, P_{ij} is the the production term, $\prod_{ij}$ is the pressure strain term which relates the fluctuating pressure and fluctuating strain, ϵ_{ij} is the dissipation term and M_{ij} is the production by system rotation. By taking into account symmetry- $R_{ij} = R_{ji}$, 6 transport equations are solved which correspond to 6 components of the Reynolds stress tensor, along with additional equation for dissipation rate, ϵ. Thus in spatially 3D flows, 7 equations are solved. For detailed understanding of modeling of all the terms please refer to [21]

2.3. CLOSURE OF TURBULENT SCALAR FLUX

The other unclosed term in eqn. 2.12 is the turbulent species and enthalpy flux. This is closed by using the gradient diffusion hypothesis as shown:

$$\overline{\rho \widetilde{Y_k'' u_j''}} = -\frac{\mu_t}{Sc_t}\frac{\partial \widetilde{Y_k}}{\partial x_i} \tag{2.24a}$$

$$\overline{\rho \widetilde{h'' u_j''}} = -\frac{\mu_t}{Pr_t}\frac{\partial \widetilde{h}}{\partial x_i} \tag{2.24b}$$

where, Sc_t and Pr_t are the turbulent Schmidt number and turbulent Prandtl number and for simple flows both numbers are of order unity [21].

2.4. COMBUSTION MODELS

The last unclosed term in eqn. 2.12 is the mean chemical source term ($\bar{\bar{\omega}}_k$). Various approaches to close this term are generally known as combustion models or Turbulence-Chemistry Interaction models (TCI). For set of reactions (R) in a mechanism with number of species S, the rate of formation/consumption of species i is

obtained by the sum of rate equations of all the elementary reactions.

$$w_i = \frac{dC_i}{dt} = \sum_{r=1}^{R} k_r \left(v_{r,i}^p - v_{r,i}^{rt}\right) \prod_{s=1}^{S} C_s^{v_{r,s}^{rt}} \quad i = 1 \cdots S \tag{2.25}$$

The rate constant k_r depends strongly on the temperature and is found to have Arrhenius temperature dependence as:

$$k_r = AT^b exp\left(-\frac{E_a}{RT}\right) \tag{2.26}$$

The reaction source term then becomes:

$$\dot{\omega}_i = w_i W_i = W_i \sum_{r=1}^{R} k_r \left(v_{r,i}^p - v_{r,i}^{rt}\right) \prod_{s=1}^{S} \left(\frac{\rho Y_s}{W_s}\right)^{v_{r,s}^{rt}} \quad i = 1 \cdots S \tag{2.27}$$

In uniform medium with reaction only, the species equations take the form of set of Ordinary Differential Equation (ODE).

There are two class of combustion models, one which solves the species transport equations to obtain the reaction source terms during run time along with flow field calculation. Another class of combustion models decouple the calculation of species transport equations from the flow field calculation based on some assumptions about the reaction timescale and flame structure. These kind of models are known as tabulated chemistry models as the reaction rate values for reduced set of chemical variables required for all reactions are stored in the table before the running of the simulation (pre-processing step) and the values are just fetched from the table during the run-time thereby reducing the computational time significantly. Firstly, the models belonging to the first group are discussed and then the tabulated methods are discussed.

2.4.1. COMBINED EDDY DISSIPATION/FINITE RATE CHEMISTRY MODEL

This method is the combination of two combustion models: Eddy Dissipation Model (EDM) and Finite Rate Chemistry Model (FRC). EDM model is a simple model which considers the effect of turbulence on the chemical reaction rate. In this model, the reaction is mixing limited meaning the chemical time scales are shorter than the turbulence mixing time scale. As the turbulence mixes the reactants it is assumed to form products. For a single step reaction scheme

$$C_x H_y + \left(x + \frac{y}{4}\right) O_2 = xCO_2 + \frac{y}{2} H_2 O \tag{2.28}$$
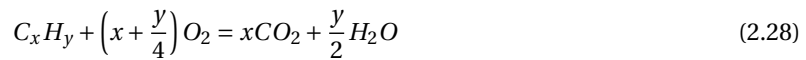
where for light heating oil used in this study, x = 14.32, y = 25.75. The Arrhenius parameters for the above reaction are given below:

Table 2.1: Arrhenius parameters for reaction 2.28. Units: J, mole, m, K

Reaction	E_a	A_F	n	m
2.28	1.256e+5	1.36e+15	0.25	1.5

The local reaction rate ($kg/m^3/s$) is obtained as the minimum of the rate computed by EDM and FRC:

$$R = min(R_{EDM}, R_{FRC}) \tag{2.29}$$

$$R_{EDM} = min\left(A_E \rho \frac{\epsilon}{k} Y_{fuel}, A\rho \frac{\epsilon}{k} \frac{Y_{ox}}{x + \frac{y}{4}}, A_E B_E \rho \frac{\epsilon}{k} \frac{Y_p}{x + \frac{y}{2}}\right) \tag{2.30a}$$

$$R_{FRC} = A_F \rho \cdot exp\left(\frac{E_a}{RT}\right)\left(Y_{C_xH_y}/W_{C_xH_y}\right)^n \left(Y_{O_2}/W_{Y_{O_2}}\right)^m \tag{2.30b}$$

where A_E and B_E are the adjustable model constants of the EDM model and are equal to 4 and 0.5 as in the original article of Magnussen et al. [22], A_F is the pre-exponential factor of Arrhenius law, Y_{fuel}, Y_{ox} Y_p are the mass fraction of fuel, oxidizer and products. There is no theoretical background for the default values of EDM model constants $A_E = 4$ and $B_E = 0.5$. The values are tuned to attain maximum flame temperature [23]. In this study, the value of A_E was changed to 2 in order to obtain maximum flame temperature which was in agreement with the equilibrium values obtained by Gaseq [24] for the light heating oil with the given global equivalence ratio of 1.45.

EDM can produce nonphysical results such as flashback (if the flow is turbulent before the flame stabilizer, EDM predicts combustion), creeping of flames along the walls (as close to the walls, the energy dissipation rate is high and according to eqn. 2.30a it predicts high reaction rate). In order to overcome this problem, EDM model is combined with Finite Rate Chemistry (FRC) method. The reaction rate for elementary reaction has Arrhenius temperature dependence and is low at low temperature. By this backward reactions can also be incorporated. But alone using FRC model neglects the influence of turbulence on combustion. By using the combination of EDM & FRC, the reaction rate is calculated as the minimum of the reaction rate calculated by the two methods. This way, the drawbacks of EDM model such as flashback, creeping of flames where EDM predicts non-physical results but according to chemistry, the reaction rates are low is avoided. But the combined EDM/FRC model cannot be used for multi step reaction mechanisms. This is because, suppose there are two reactions, reaction A with slower chemical time scale than turbulent mixing time scale and reaction B, with faster chemical time scale than the turbulent mixing time scale. In a fully turbulent flow where all the reactants are well mixed, at a certain point, according to the principle of combined EDM/FRC, reaction A will have reaction rate from turbulence while reaction B will have reaction rate from chemistry while in reality this does not happen. Thus, only single step chemistry is allowed with combined EDM/FRC model.

2.4.2. EDDY DISSIPATION CONCEPT

Eddy Dissipation Concept (EDC) is an extension of the Eddy Dissipation Model (EDM) to include detailed chemical mechanisms in turbulent combustion. The effect of the turbulent fluctuations on mean chemical reaction rate is taken into account using the phenomenological description of turbulence through the energy cascade. It is believed that the mixing of reactants and the dissipation of turbulent energy happens only in small volume fraction of the fluid and these regions are occupied by fine structures whose characteristic dimensions are of the same magnitude of the Kolmogorov scale [25]. It is in these structures that the turbulence energy is dissipated and is assumed that the reactants will be mixed at microscale and react. In EDC model, the computational cell is divided into two zones namely the reacting "fine structure" and "surrounding fluid" as shown in fig. 2.1. All the reactions occur inside the fine structures of size ξ for a time scale of τ where the conditions are assumed to be adiabatic, isobaric, perfect stirred reactor, transferring mass and energy to the surrounding fluid where only turbulent mixing takes place thus transferring mass and energy to and from the fine structure. The size of the fine structure and the mean residence time of the fluid in fine structure is determined from following expressions:

$$\xi = C_\xi \left(\frac{\nu\epsilon}{k^2}\right)^{1/4} \tag{2.31}$$

$$\tau = C_\tau \left(\frac{\nu}{\epsilon}\right)^{1/2} \tag{2.32}$$

where C_ξ is the volume fraction constant and the default value in FLUENT is set to 2.1377, C_τ is the time scale constant which is set to a default value of 0.4082 and ν is the kinematic viscosity. As mentioned earlier,
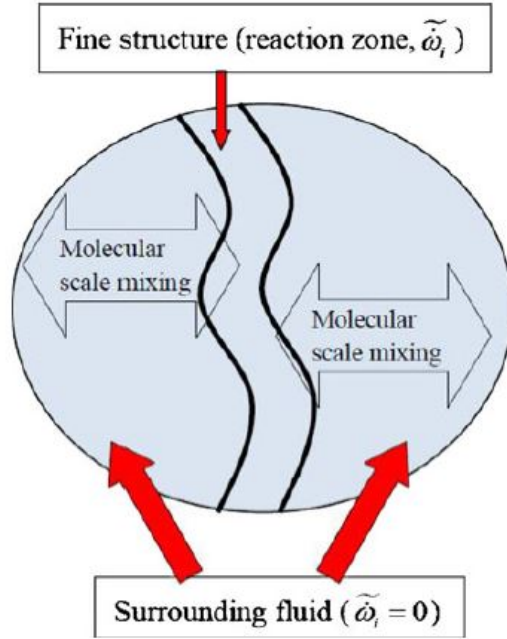
Figure 2.1: Fine scale and surrounding fluid in EDC model [3]

the computational cell is assumed to be a constant pressure reactor. The initial conditions are taken as the current species and temperature values in the cell and reactions proceed over a time scale τ governed by Arrhenius rates and are integrated numerically in time using ISAT algorithm [26] thereby the use of "Plug Flow Reactor" is made in FLUENT code as opposed to "Perfectly Stirred Reactor" which some researchers have used as discussed in [3]. The mean reaction source term with this approach is determined from the following equation.

$$\widetilde{\omega}_i = \frac{\overline{\rho}\xi^2}{\tau\left(1-\xi^3\right)}\left(Y_i^* - \widetilde{Y}_i\right) \tag{2.33}$$

where Y_i^* is the mass fraction of the species reached from the initial value of $\widetilde{Y}_i$ by action of applied chemical reaction mechanism over time τ.

2.5. FLAMELET APPRAOCH

The other class of TCI models which use tabulated chemistry approach are discussed here. With the detailed chemistry, calculation of reaction rates from EDC model is computationally expensive. In contrast, tabulated approaches are more computationally efficient. Flamelet models assume that the mean composition and source terms can be obtained by averaging over properties of laminar local states. The thermochemistry calculations (species, temperature) are stored in a table in a pre-processing step and are looked-up during run-time thereby reducing the run-time significantly. In the following subsections, two different methods of flamelet approach: Steady Flamelet method and Flamelet Generated Manifold (FGM) methods are elucidated.

2.5.1. STEADY FLAMELET MODEL

The flamelet concept was first proposed by Peters [27] where the flame reaction zone is assumed to be very thin and that the turbulent flame is an ensemble of laminar counter-flow diffusion flames as shown in Fig. 2.2. In turbulent flow, the flamelet concept is valid when the chemical reactions are faster than the smallest turbulent time scale i.e Kolmogorov time scale. This is expressed through Damköhler number which is defined as:

$$Da = \frac{t_{flow}}{t_{chemical}} \tag{2.34}$$

The solutions of flame calculations are functions of the physical space and thus in general are multi-dimensional.
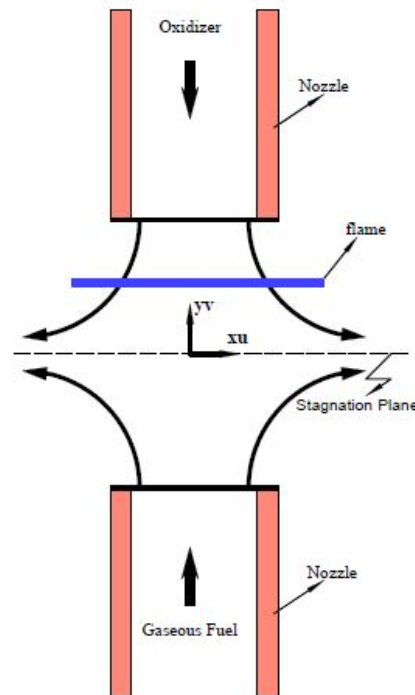
Figure 2.2: Laminar counter-diffusion flame

A different counter-diffusion flame is observed when the spacing of the fuel and oxidizer in Fig. 2.2 or their velocity are changed and this needs to be incorporated. Also, in the flamelet concept as the flame reaction zone is thin, only changes in the direction orthogonal to flame front are important and changes parallel to flame front are negligible. This reduces the multi-dimensional system to one dimension. For non-premixed combustion this one dimension is characterized by a new variable known as mixture fraction which has value of zero in air inlet and is equal to one in fuel inlet. By coordinate transformation the governing equations for species and temperature from physical space are converted to mixture fraction space. In FLUENT, some assumptions are made for the derivation of flamelet governing equations which are shown below:

- Lewis number is unity i.e mass diffusivity is equal to thermal diffusivity.

- Diffusion coefficients of all species is equal.

Based on these assumptions the following flamelet equations are derived for species and temperature.

$$\rho \frac{\partial Y_k}{\partial t} = \frac{1}{2} \rho \chi \frac{\partial^2 Y_k}{\partial Z^2} + S_k \tag{2.35a}$$

$$\rho\frac{\partial T}{\partial t} = \frac{1}{2}\rho\chi\frac{\partial^2 T}{\partial Z^2} - \frac{1}{C_p}\sum_k H_k S_k + \frac{1}{2C_p}\left[\frac{\partial C_p}{\partial Z} + \sum_k C_p\frac{\partial Y_k}{\partial Z}\right]\frac{\partial T}{\partial Z} \tag{2.35b}$$

where Y_k & T are the species mass fraction and temperature respectively. $\rho, C_p, C_{p,k}$ are the density, mixture averaged specific heat and specific heat of kth species respectively. In eqn. 2.35a & eqn. 2.35b there is a new factor χ, which is known as scalar dissipation rate. The scalar dissipation effects the change in relative velocities of the counter-flowing jets and is a measure of the departure from the equilibrium condition. Higher scalar dissipation shows deeper non-equilibrium phenomena in the flame. Furthermore, turbulence stretches and strains the flame. In order to consider the effect of strain rate in the mixture fraction space, the scalar dissipation is defined as:

$$\chi = 2D|Z|^2 \tag{2.36}$$

where D is the diffusion coefficient of species. Now, in order to solve eqn. 2.35a & eqn. 2.35b the knowledge of χ is needed. Thus, species mass fraction and temperature can be obtained as a function of mixture fraction and scalar dissipation rate. Further, in the steady flamelet method the temporal terms in eqn. 2.35a and eqn. 2.35b are ignored and only the RHS terms are solved for solution of species mass fraction and temperature. The scalar dissipation rate is varied from a very small value (close to equilibrium) in small steps until the flamelet is extinguished. Typical generation of a flamelet can be seen in Fig. 2.3 where blue lines correspond to the steady flamelet model. The results from the flamelet generation are stored in the table and the independent parameters of this table are mixture fraction and scalar dissipation rate.

Non-adiabatic effects due to droplet evaporation can be taken into account through the calculation of enthalpy. However, modeling of steady flamelets over a range of enthalpies is quite difficult. Hence, in ANSYS FLUENT, assumption is made that the effect of heat loss/gain is considered not to affect the species mass fractions. So the adiabatic species mass fractions are still used and the temperature is adjusted according to the mean enthalpy gain or loss.

Although the chemical time scales in SFM are assumed to be smaller than the smallest turbulence time scale, turbulence can still wrinkle, stretch and strain the flame. These effects have to be included during the flame calculations. Thus turbulence-chemistry interactions are taken into account through the joint Probability Density Function (PDF) of the controlling parameters Z, χ_{st}.

$$\widetilde{\phi} = \int_0^1 \int_0^\infty \phi(Z, \chi_{st})\widetilde{P}(Z, \chi_{st})\, dZ d\chi_{st} \tag{2.37}$$

where ϕ is species mass fraction or temperature and $\widetilde{P}$ is the joint PDF. χ_{st} is the value of scalar dissipation rate at stoichiometric mixture fraction and is characteristic of each flamelet. If the variables are assumed to be statistically independent, then the joint PDF in the above equation can be expressed as:

$$\widetilde{\phi} = \int_0^1 \int_0^\infty \phi(Z, \chi_{st})\widetilde{P_Z}(Z)\widetilde{P_\chi}(\chi_{st})\, dZ d\chi_{st} \tag{2.38}$$

The advantage of using separate PDF for each variable is that the shape of the PDF can be assumed for each of the variables. In FLUENT, the mixture fraction is presumed to be of shape of β function. By doing this, the fluctuations in the mixture fraction are taken into consideration. But for χ_{st} no presumed PDF is considered. Alternatively, Dirac delta function is used to define the fluctuations in χ_{st}. The β function is defined as shown in eqn. 2.39a. In order to determine the β function, the mean ($\widetilde{Z}$) and its variance ($\widetilde{Z''^2}$) have to be known. Once these quantities are determined the β function can be computed.

$$p(Z) = \frac{Z^{\alpha-1}(1-Z)^{\beta-1}}{\int_0^1 Z^{\alpha-1}(1-Z)^{\beta-1}\, dZ} \tag{2.39a}$$

$$\alpha = \left[\frac{\widetilde{Z}\left(1-\widetilde{Z}\right)}{\widetilde{Z''^2}} - 1 \right] \widetilde{Z} \tag{2.39b}$$

$$\beta = \left[\frac{\widetilde{Z}\left(1-\widetilde{Z}\right)}{\widetilde{Z''^2}} - 1 \right] \left(1-\widetilde{Z}\right) \tag{2.39c}$$

As mentioned earlier the fluctuations in stoichiometric scalar dissipation rate is assumed to be of Dirac delta function. The Dirac delta function is shown in eqn. 2.40a.

$$p_\chi\left(\chi_{st}\right) = \delta\left(\chi_{st} - \widetilde{\chi_{st}}\right) \tag{2.40a}$$

$$\widetilde{\chi_{st}} = C_\chi \frac{\epsilon}{k} \widetilde{Z''^2} \tag{2.40b}$$

where C_χ is a constant and is equal to 2. Also the turbulence quantities ϵ, k are obtained from the employed turbulence model.

With the values of independent parameters Z & χ obtained from the flamelet table, the turbulence-chemistry interaction can be included through the above mentioned process. By doing so, the earlier two dimension calculation (Z & χ) will be changed to three dimension namely mean mixture fraction ($\widetilde{Z}$), mixture fraction variance ($\widetilde{Z''^2}$) and mean stoichiometric scalar dissipation rate ($\widetilde{\chi_{st}}$). In order to reduce the computational time, the integration of eqn. 2.38 of is not performed during run-time and instead it is performed in the pre-processing step by solving the equation for various values of ($\widetilde{Z}, \widetilde{Z''^2}, \widetilde{\chi}_{st}$). The result of this is the species mass fraction and temperature are stored in three-dimensional look-up table for referencing during run-time. Also inclusion of non-adiabtic case is possible and in this case one additional dimension of mean enthalpy is needed to describe the heat/loss gain. Finally, the process of executing the presumed PDF Steady Flamelet Method is described in the process flow diagram in Fig. 2.3
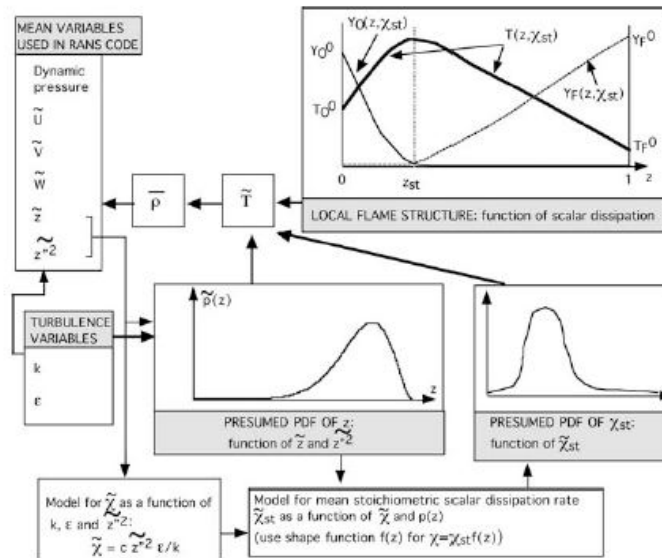
Figure 2.3: Execution of PDF steady flamelet method [4]

2.5.2. FLAMELET GENERATED MANIFOLD (FGM)

As mentioned earlier with Steady Flamelet Method, deeper non-equilibrium effects such as ignition, mixing cannot be captured and thus a more general approach such as Flamelet Generated Manifold is needed. Overall the basic procedure is similar to SFM method but there are some differences in the FGM methodology. When the flamelets are generated, the non-equilibrium unsteady effects are considered which are not done in SFM method. In SFM method, the flamelets are generated from $\chi = 0$ until the flamelet is extinguished, $\chi_{extinguish}$ which are seen as the lowest blue line in the Fig. 2.4. With FGM the transient extinguishing flamelet is added (red lines in Fig. 2.4 covering the range from the start of extinction to pure mixing). Similar to SFM, in FGM the reaction is assumed to happen in lower dimension manifolds which are charac-
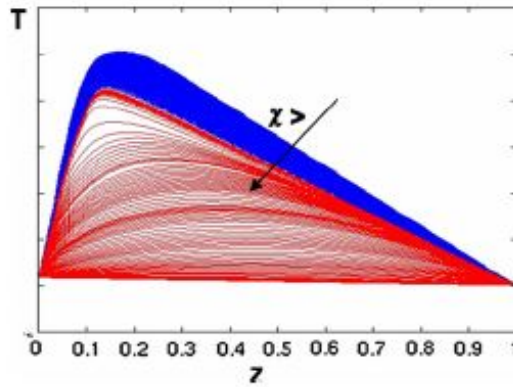
Figure 2.4: Temperature vs. Mixture fraction with increasing scalar dissipation rate

terized by few independent variables which can change in the composition space. In FGM the controlling parameters are mixture fraction which shows the extent of mixing and a new variable is used which shows the progress of the reaction completion, c, with $c = 0$ from pure mixing in unburned condition to $c = 1$ fully burnt condition. In FLUENT mass fractions of CO_2, CO are used as the marker of the reaction progress. The progress variable is defined as shown in eqn: 2.41.

$$c = \frac{Y_k^{eq} - Y_k}{Y_k^{eq} - Y_k^{mixing}} \tag{2.41}$$

where Y_k^{eq} denotes the species mass fraction at equilibrium condition and Y_k^{mixing} shows the mass fraction at mixing condition. Similar to SFM method, the turbulence-chemistry interaction is modeled through joint PDF and β function shape is presumed for fluctuation of progress variable c along with the β shape for mixture fraction, Z. In order to define the β function, mean progress variable ($\tilde{c}$) and progress variable variance ($\widetilde{c''^2}$) have to be known. Therefore in FGM, 4 transport equations are solved namely: mixture fraction (eqn. 2.42a) and its variance and un-normalized progress variable (eqn. 2.42b) and its variance [28].

$$\frac{\partial \rho \tilde{z}}{\partial t} + \nabla \left(\rho \mathbf{v} \tilde{z} \right) = \nabla \left(\frac{\mu_t}{\sigma_t} \nabla \tilde{z} \right) \tag{2.42a}$$

$$\frac{\partial \rho \tilde{c}}{\partial t} + \frac{\partial \left(\rho \tilde{u}_i \tilde{c} \right)}{\partial x_i} = \frac{\partial}{\partial x_i} \left(\rho D_{eff} \frac{\partial \tilde{c}}{\partial x_i} \right) + \tilde{S}_c \tag{2.42b}$$

where μ_t and σ_t are turbulent viscosity and turbulent Schmidt number and $\tilde{S}_c$ is the reaction progress source term which is obtained from the flamelet library. When these quantities are known, the species mass fraction

and temperature are computed from the following integral equation.

$$\widetilde{\phi} = \int_0^1 \int_0^1 \phi(Z,c)\, \widetilde{P_Z}(Z)\, \widetilde{P_c}(c)\, dZ dc \tag{2.43}$$

Again, the effect of heat loss/gain can be taken in to account by adding another dimension of mean enthalpy. Finally, the integration of eqn. 2.43 is carried out for different values of ($\widetilde{Z}$, $\widetilde{Z''^2}$, $\widetilde{c}$, $\widetilde{c''^2}$) and are stored in look-up table for referencing during run-time. It should be mentioned here that the gaseous flamelets are used to represent the local structure of the turbulent spray flames. But the droplet evaporation process in spray combustion provides local fuel source and could modify the reaction zone in the mixture fraction space. For detailed information on spray flamelet modeling refer to [29] and references therein.

2.6. DISPERSED PHASE MODELING

2.6.1. GOVERNING EQUATIONS FOR DISPERSED PHASE

The injection of liquid fuel into the gas phase sets off a wide variety of interaction among the two phases. The main processes of turbulent spray combustion involves disintegration of bulk liquid into ligaments and then droplets known as primary atomization. Secondary atomization may be present depending upon the drop sizes produced after primary atomization. The droplets are injected into the gas phase and experience aerodynamic forces and thereby exchange momentum with the continuous phase. The turbulence present in the gas phase facilitates the mixing of droplets with gas phase thereby distributing these sources of chemical energy in the flow, which is modeled as turbulent particle dispersion. Further, the concentration gradient at the droplet gas interface leads to evaporation of liquid fuel. Turbulence enhances the evaporation by homogenizing the gas phase in the vicinity of the droplet. This evaporated fuel then acts as a source for combustion process and the combustion process releases heat leading to faster evaporation of fuel. All these processes are highly coupled with the gas phase and a change in one of the processes leads to different combustion performance and hence all these processes needs to be correctly modeled. All these changes are accounted into the gas phase through various source terms which appear in the gas phase governing equations as seen in section 2.1.

There are two different methods to treat the dispersed phase in conjunction with gas phase and these are Eulerian framework and Lagrangian framework. In the Eulerian framework the dispersed phase is also treated as continuum and interacts with the gas phase continuum resulting in set of differential equations representing conservation laws of mass, momentum and energy. The Eulerian approach is easy to apply and computationally inexpensive but the constitutive relationships to solve the governing equations are rather empirical. Also, prediction of droplet size distributions is difficult. In the Lagrangian framework, the discrete particles are tracked through the computational domain by solving their equation of motion. Lagrangian approach is widely used for particle tracking in many engineering problems [30–33]. In this thesis, the spray is dilute as the volume fraction of the dispersed phase in the gas phase is very low. Therefore Lagrangian framework is used to model the discrete phase in both SPRAYSIM and FLUENT.

As in Lagrangian method each droplet is tracked throughout the computational domain, the number of droplets produced by a spray process is of the order of millions and thus the computational cost of doing such a modeling would be very high. Therefore the parcel approach is used wherein group of droplets (parcels) of identical properties such as diameter, velocity, temperature are continuously injected into the computational domain with the given initial conditions. Then the evolution of the parcels through the properties of position, velocity, diameter, velocity and temperature is sought in Lagrangian frame by solving the equation of motion

for every parcel.

In this work, droplets are tracked using the steady injection method. In this method, after the iterations of gas field, the spray parcels are injected into the flow from the desired position with the given initial conditions. These parcels are then tracked in the domain and the status of each parcel is registered either as evaporated, escaped or incomplete. Where escape means that the parcel has left the computational domain without evaporating and incomplete means the number of tracking steps specified was not sufficient enough to track the parcel. After one discrete phase injection, specified number of gas phase iterations are solved with the sources from the discrete phase calculated from previous calculation. Then again the discrete phase parcels are injected into the modified gas field for re-tracking of the injected parcels and this loop is continued until the convergence is obtained.

As there is exchange of mass, momentum and energy between liquid and gas phase. In order to evaluate these a set of ordinary differential equations are solved in the Lagrangian framework of the dispersed phase.

The mass conservation for a droplet can be written as follows, which shows the conversion of liquid mass in time equal to the vapor mass flow.

$$\frac{dm_p}{dt} = -\dot{m}_v \tag{2.44}$$

where m_p is the parcel mass and $\dot{m}_v$ is the vapor mass flow. The droplet motion is given by eqn. 2.45 which is a function of time and depends on all the forces acting on it.

$$\frac{d\left(m_p \cdot \vec{u}_p\right)}{dt} = -m_v \cdot \vec{u}_p + \sum \vec{F}_i \tag{2.45}$$

where $\vec{u}_p$ is the droplet parcel velocity and $\sum \vec{F}_i$ is the sum of forces acting on the droplet. Differentiating eqn. 2.45 gives the following equation.

$$m_p \frac{d\vec{u}_p}{dt} = \sum \vec{F}_i \tag{2.46}$$

The sum of forces includes: the drag force experienced by the droplet due to the relative velocity between discrete and continuous phase. Volume force due to gravity. Basset force which is due to the transient nature of the development of the particle's boundary layer. Virtual mass force which originates due to the difference in the acceleration of fluid and particle. Magnus force which arises due to rotation of particle in a non-rotating environment. And finally, Saffman force which accounts for lift force experienced by particle when it moves through a viscous liquid due to the velocity gradients caused by the translational velocity of the particle.

However, the equation of motion can be greatly simplified when the flow is considered to be dilute, turbulence intensities are less and particle to fluid density ratio is greater than 200 and the droplets are of spherical shape. In this situation, apart from drag and volume forces by gravity all other forces mentioned above such as Basset, Magnus, virtual mass and Saffman are negligible. Hence the particle motion equation with drag force and volume force is given in terms of particle relaxation time.

$$\frac{d\vec{u}_p}{dt} = \frac{1}{\tau_{relax}} \cdot \vec{u}_{rel} + \left(1 - \frac{\rho_g}{\rho_p}\right) \cdot \vec{g} \tag{2.47}$$

where $\vec{g}$ is the specific volume force, $\vec{u}_{rel}$ is the slip velocity and ρ_p, ρ_g are the density of the parcel and gas phase respectively. τ_{relax} is the particle relaxation time defined in eqn. 2.48 as:

$$\tau_{relax} = \frac{4}{3}\frac{\rho_g}{\rho_p}\frac{d_p}{C_D |u_{rel}|} \tag{2.48}$$

where C_D is the drag coefficient. For dilute spray the drag coefficient in SPRAYSIM is taken from Clift et al.

[34] for solid spheres without correction for evaporation. In FLUENT the drag coefficient when no secondary breakup is activated is obtained as:

$$C_D = a_1 + \frac{a_2}{Re_p} + \frac{a_3}{Re_p^2}$$

(2.49)

where the droplet Reynolds number Re_p is:

$$Re_p = \frac{\rho_g \left| \vec{u}_p - \vec{u}_g \right| d_p}{\mu_g}$$

(2.50)

Knowing the velocity of the particle, the droplet location can be obtained by the integration of the following equation.

$$\frac{d\vec{x}_p}{dt} = \vec{u}_p$$

(2.51)

With the mass and momentum conservation determined the droplet energy equation is obtained as:

$$\frac{dT_p}{dt} = \frac{\dot{m}_v \Delta h_v - \dot{Q}}{C_{p,liq} \rho_{liq} V_d}$$

(2.52)

where T_p is the parcel temperature, h_v is the enthalpy of vaporization, $\dot{Q}$ is the heat flow onto the surface of the droplet, $C_{p,liq}$ is the specific heat of liquid at constant pressure, ρ_{liq} is the density of the liquid and V_d is the volume of the droplet. The mass flow rate due to vaporization and the heat flow into the liquid is obtained from an evaporation model such as Abramzon-Sirignano evaporation model described below [35].

2.6.2. EVAPORATION MODELING

In brief, the Abramzon-Sirignano model is based on the classical gas-film theory. It assumes that the gas obeys ideal gas law and the droplet interior is well mixed i.e. there is no temperature gradient inside the droplet (also known as infinite conductivity model) and the process of heat and mass transfer is quasi-steady. Quasi-steady means: if an evaporating droplet is kept at constant radius by continuous replenishment of liquid at the droplet center, then the concentration gradient away from the droplet is steady. The classical gas-film theory assumes that the resistance to heat and mass transfer from the non-vaporizing particle and gas flow may be modeled by introducing diffusional and thermal boundary layer of constant thickness. But this does not include the Stefan flow (blowing effect) which thickens the laminar boundary layer and thereby modifies the heat and mass transfer process. With infinite conductivity model the temperature evolution is given as follows:

$$\frac{dT_p}{dt} = \frac{\pi d_p \lambda_{film} Nu}{m_p C_{p,liq}} \left(T_{film} - T_p \right) + \frac{1}{C_{p,liq}} \frac{\Delta h_v}{m_p} \dot{m}_p$$

(2.53)

where T_p is the droplet temperature, d_p is the droplet diameter, λ_{film} is the gas phase thermal conductivity evaluated at film condition, $C_{p,liq}$ is isobaric heat capacity of liquid, Δh_v is the latent heat of vaporization and m_p is the droplet mass. The mass transfer is given by:

$$\frac{dm_p}{dt} = \pi d_p Sh D_{vap} \rho_g ln(1 + B_M)$$

(2.54)

where Sh is the Sherwood number D_{vap} is the diffusion coefficient, B_M is the Spalding mass transfer number which is obtained from Raoult's law and Clausius-Clapeyron equation. The Sherwood number and Nusselt number for convective flow is obtained from the popular Ranz-Marshall correlation given as:

$$Nu = 2 + 0.552 Re_p^{1/2} Pr_{film}^{1/3}$$

(2.55a)

$$Sh = 2 + 0.552 Re_p^{1/2} Sc_{film}^{1/3} \tag{2.55b}$$

In order to account for the Stefan flow, corrections have been given by Abramzon and Sirignano [35] for Sherwood and Nusselt numbers which are given in eqn. 2.56b and eqn. 2.56a.

$$Nu^* = 2 + \frac{Nu - 2}{F_T} \tag{2.56a}$$

$$Sh^* = 2 + \frac{Sh - 2}{F_M} \tag{2.56b}$$

$$F_T = (1 + B_T)^{0.7} \frac{ln(1 + B_T)}{B_T} \tag{2.57a}$$

$$F_M = (1 + B_M)^{0.7} \frac{ln(1 + B_M)}{B_M} \tag{2.57b}$$

$$B_T = (1 + B_M)^{\phi} - 1 \ \ \text{with} \phi = \frac{C_{p,vap}}{C_{p,film}} \frac{Sh^*}{Nu^*} \frac{Pr_{film}}{Sc_{film}} \tag{2.58}$$

where F_M and F_T represent the relative change in film thickness due to Stefan flow effect. When Abramzon-Sirignano model is used, Nu and Sh in the eqn. 2.53 and eqn. 2.54 are replaced with Nu^* and Sh^*. Finally the film condition is chosen as:

$$T_{film} = T_s + \frac{1}{3}(T_\infty - T_s) \tag{2.59a}$$

$$Y_{film} = Y_s + \frac{1}{3}(Y_\infty - Y_s) \tag{2.59b}$$

where 1/3 value is recommended for most of spray combustion calculations and also popularly known as "$1/3^{rd}$" rule. Other values of 1 and 1/2 have also been used as mentioned in [29].

The evaporation model in FLUENT employs the classical model of evaporation with correction for the convective transport of fuel vapor and gas mixture away from droplet surface (Stefan flow) [36]. This results in following equation for Nusselt number:

$$Nu = \frac{ln(1 + B_T)}{B_T} Nu_0 \tag{2.60}$$

where Nu_0 is obtained from eqn. 2.55a with coefficient of 0.552 changed to 0.6. For mass transfer away from the droplet FLUENT uses eqn. 2.55b with coefficient of 0.552 changed to 0.6.

2.6.3. SECONDARY ATOMIZATION

When a drop experiences a surrounding flow field moving with some velocity relative to it, the aerodynamic forces cause the droplet to deform and break into smaller droplets. This process is referred to as secondary atomization [37]. Whereas in primary atomization the sheet or jet of liquid breaks up for the first time to form drops and it occurs close to the nozzle exit. To model the secondary atomization: "Cascade atomization and drop breakup" model (CAB) of Tanner [38] was used in SPRAYSIM in the CFX-SPRAYSIM coupled runs as the drop size prediction with the given initial drop size condition did not match the experimental values at the first measurement position, which is explained further in 3.1.

The CAB model is used to accommodate the catastrophic breakup apart from bag and stripping breakup modes observed in many sprays. In CAB model the drop breakup is considered by taking into account the aerodynamic forces acting on the droplet which leads to its distortion and subsequent breakup into collection of product droplets. The drop distortion and breakup criteria is based on the droplet deformation dynamics

of Taylor Analogy Breakup model where the droplet deformation is thought of as spring-mass-damper system. The aerodynamic droplet-gas interaction is the forcing term while the liquid viscosity plays the role of damper and surface tension acts as the restoring force. Drop breakup occurs when the gas Weber number (eqn. 2.61) exceeds the critical value. The properties of the product droplets are governed by eqn. 2.62 based on the theory of population dynamics. In short, it is assumed that the number of product droplets formed is proportional to number of parent droplets and the proportionality constant depends on the drop breakup regime.

$$We = \frac{\rho_{gas} v_{rel}^2 d}{\sigma} \tag{2.61}$$

$$\frac{d}{dt}\overline{m}(t) = -3K_{bu}\overline{m}(t) \tag{2.62}$$

$$K_{bu} = \begin{cases} k_1 \omega & We_{crit} < We \leq We_{b,s} \\ k_2 \omega & We_{b,s} < We \leq We_{s,c} \\ k_3 \omega We^{3/4} & We_{s,c} < We \end{cases} \tag{2.63}$$

where subscripts b ,s, c correspond to bag, stripping and catastrophic breakup, constant k_1 is determined from the Rayleigh-Taylor instability analysis and is equal to 0.05, $\overline{m}$ denotes the mean mass of the product drop distribution. Values of k_2 & k_3 are chosen such that K_{bu} is continuous across all Weber numbers.

2.6.4. TURBULENT PARTICLE DISPERSION

In dilute spray applications such as the combustion system, the dispersion of fuel droplets due to turbulent fluctuations is important and has to be properly accounted for. The droplets carry the chemical energy with them and hence their position in the combustor affects the reaction zone and flame characteristics. The particle dispersion model varies depending on which framework (Eulerian or Lagrangian) is used to describe particle motion. In most combustion studies, Lagrangian framework is employed.

Modeling particle dispersion depends mainly on two aspects [39] :

- Carrier phase turbulence models.

- The ability of the carrier phase models to provide the exact details of instantaneous gas velocity at each particle location needed to model particle dispersion.

Thus, the key to modeling particle dispersion is to obtain the required data through turbulence models with valid assumptions. When Lagrangian particle tracking is applied, there are two ways to model the particle dispersion: the particle trajectories are generated directly using stochastic model (random walk model) for Lagrangian velocities. This method is simpler as it does not require the information from Eulerian fluid velocity field but it is confined to passive particles such as dispersion of pollutants in atmosphere. In the second approach, the particle trajectories are obtained by solving the particle momentum equation for representative samples through the Eulerian fluid velocity field. But there is a problem with this approach, the carrier phase is solved in Eulerian framework and the practical turbulence models give time-averaged fluid velocity, whereas the particle momentum equation requires instantaneous carrier phase velocity at each particle location. So these models need to estimate fluctuating fluid velocity at each particle location as it moves through the computational domain.

In turbulence, the fluctuating velocity is correlated to itself for a certain time interval before it significantly changes. This time interval is roughly of the order of the Lagrangian fluid time scale. According to Gosman et al. [40] the Lagrangian fluid time scale is conceptually similar to particle Lagrangian time scale and it can

be viewed as the large eddy lifetime based on the dissipation length scale (Kolmogorov scale). According to Taylor's theory of particle dispersion, in order to calculate the variance in the particle trajectory, this fluctuating fluid velocity at two different times is needed. This temporal correlation is an important factor to consider if the particle trajectories are constructed by marching downstream the flow with time steps less than or equal to Lagrangian fluid time scale. Thus the models which estimate the fluctuating fluid velocity from the time-averaged Navier-Stokes equation need to circumvent a way to account for fluid temporal correlation. To obtain time-dependent data, the same fluctuating fluid velocity is assumed to act on the particle for a time interval known as particle-eddy interaction time, which is the minimum of the eddy lifetime and the transit time needed for a particle to cross an eddy of certain size. In the following models, the concept of particle interaction time is used to model turbulent particle dispersion.

In FLUENT, the Discrete Random Walk model of Gosman and Ioannides [40] is used. According to this theory, the instantaneous gas velocity in the particle momentum equation is obtained from the time-averaged Navier-Stokes equation and the carrier phase turbulence fields. The turbulence is assumed to be isotropic and the droplets are assumed to interact with a sequence of randomly sampled turbulent eddies. The fluctuating velocity is assumed to be the shape of Gaussian PDF (eqn. 2.64) with zero mean mean and standard deviation obtained from the local turbulence kinetic energy which are sampled at appropriate points in the domain to obtain the prevailing fluctuating velocity field.

$$u' = \zeta \sqrt{\overline{u'^2}} \tag{2.64}$$

where ζ is normally distributed random number. In eqn. 2.64 the RHS is the RMS fluctuating velocity which is related to the kinetic energy obtained from the transport equation for kinetic energy.

$$\sqrt{\overline{u'^2}} = \sqrt{\overline{v'^2}} = \sqrt{\overline{w'^2}} = \sqrt{2k/3} \tag{2.65}$$

When Reynolds Stress Model is used, the fluctuating velocity in each direction is obtained separately by using the computed normal stresses. For particle trajectory computation, the time for integration is obtained using particle-eddy interaction time which is mentioned before. To compute particle-eddy interaction time, the eddy lifetime τ_e is assumed to be either constant as shown in eqn. 2.66b or as random variation about Lagrangian fluid time scale, shown in eqn. 2.66c computed in FLUENT as:

$$T_L \approx 0.15 \frac{k}{\epsilon} \tag{2.66a}$$

$$\tau_e = 2T_L \tag{2.66b}$$

$$\tau_e = -T_L \, ln(r) \qquad 0 < r < 1 \tag{2.66c}$$

Particle eddy transit/crossing time is computed as:

$$t_{cross} = -\tau \, ln \left[1 - \left(\frac{L_e}{\tau \left| u - u_p \right|} \right) \right] \tag{2.67}$$

where τ is the particle relaxation time, L_e is the characteristic eddy size (based on dissipation length scale) and $\left| u - u_p \right|$ is the slip velocity. The particle interacts with the eddy for a time which is minimum of eddy lifetime and eddy crossing time. When this time is reached the particle is assigned a new fluctuating velocity by applying new value of ζ in eqn. 2.64.

When steady tracking of particles is used in FLUENT, each time when the particles are injected, certain

number of times (referred to as number of tries) each particle in the injection is tracked through the flow with the calculated random carrier phase fluctuating field. When this number is small the ensemble average of the trajectories is different each time the trajectories are computed. In order to have statistical convergence a sufficient number of tries should be used. But high value of this leads to longer computational time. Thus a trade-off has to be made. Recommended values for number of tries is between 3-5.

In SPRAYSIM, the spectral dispersion model of Blümcke [41] is used. As in DRW model, this model is also based on stochastic approach to determine the particle trajectories. In DRW model, the parcel experiences a constant gas fluctuation velocity as long as it is thought to be moving inside an eddy. These gas fluctuation velocities experienced successively by a parcel along its trajectory are not correlated. In Blümcke's more advanced spectral dispersion model, a realistic decay of the two-point autocorrelation of the gas fluctuation velocity components 'seen' by the parcel both in time and in space is employed. For detailed description, the readers can refer to [41].

2.6.5. GAS-DISCRETE PHASE COUPLING

The interaction of discrete phase with continuous phase is taken into account through various source terms in gas phase balance equations. The coupled calculation in both SPRAYSIM and FLUENT is carried out as follows:

1. Solve the gas field prior to the introduction of discrete phase.

2. Introduce the discrete phase by calculating the particle trajectories and compute the sources for gas phase.

3. Recalculate the gas field with the exchanged mass, momentum and heat transfer source terms calculated during discrete phase.

4. Recalculate the discrete phase with the modified gas field.

5. Repeat the previous two steps until a converged solution is achieved in which both the continuous phase flow field and the ensemble of discrete phase particle trajectories are unchanged with successive iterations.

The source terms calculated during discrete phase calculations when introduced into the gas field may cause solution to become unstable or lead to divergence. Therefore under-relaxation factors are introduced in the mass, momentum and heat transfer terms to let the impact of the discrete phase change only gradually. The set of equations shown in eqn. 2.68 show the update process with the under-relaxation factor α where m,f,e are the exchanged mass, momentum and heat transfer terms.

$$m_{new} = m_{old} + \alpha \left(m_{calculated} - m_{old} \right) \tag{2.68a}$$

$$f_{new} = f_{old} + \alpha \left(f_{calculated} - f_{old} \right) \tag{2.68b}$$

$$e_{new} = e_{old} + \alpha \left(e_{calculated} - e_{old} \right) \tag{2.68c}$$

When the source terms of mass, momentum and heat transfer are introduced into the gas field as shown above it is known as two-way coupling. However, with regards to turbulence, only the influence of gas phase turbulence on discrete phase is considered. Whereas the gas phase turbulence can also be modified by the discrete phase. The effect of this is known as "turbulence two-way coupling". When the particles are introduced into the carrier phase, either augmentation or attenuation of turbulence can occur depending on the

size of the particles [26, 42]. Generally it is believed that small particles (smaller than energetic eddy in the flow) attenuate the turbulence intensity of the carrier phase as the small particles in an eddy are imparted kinetic energy at the expense of the eddy's turbulent energy. On the other hand large particles tend to augment the turbulence intensity through vortex shedding in the wake region of the particles. This modulation of the turbulence manifests as source terms in turbulence transport equations (eqn. 2.16, eqn. 2.17). In SPRAYSIM, this turbulence two-way coupling is available but has not been used. In FLUENT, the turbulence two-way coupling is only possible when $k - \epsilon$ turbulence models are used. However, when Reynolds Stress model is employed, FLUENT does not allow the turbulence two-way coupling. Study of turbulence two-way coupling is used to assess the sensitivity of this in the current case and is discussed in the results section.

2.7. RADIATION MODEL

Radiation plays an important role in a of combustion chamber and an accurate treatment of radiation is essential to develop a mathematical model of the combustion system. The level of detail to be included depends on the problem of interest such as, in order to model pollutant formation accurate prediction of temperature distribution is of paramount importance as species rate equations are highly dependent on temperature. Hence radiation has to be treated carefully. Also, prediction of soot formation and oxidation is highly dependent on temperature and inaccurate prediction of temperature leads to erroneous soot yield and therefore radiative heat losses. Radiation effects are important when the domain size is big and the fraction of heat transfer due to radiation grows with the combustor size [43]. Radiative heat transfer can be computed if the radiative properties of the participating medium and the temperature field is known. But as the temperature field is unknown and is solved for in CFD simulations, the radiative transfer equation is coupled to the energy equation through a heat source term in eqn. 2.3, Q. This heat source term can be expressed as divergence of heat flux vector, $\vec{q}_R$,

$$\vec{q}_R = \int_0^\infty \kappa_\eta \left(4\pi I_{b\eta} - \int_{4\pi} I_\eta d\Omega \right) d\eta \tag{2.69}$$

where η is the wavenumber, Ω solid angle, κ_η the spectral absorption coefficient, I_η the spectral radiative intensity and subscript b denotes blackbody property. As the radiative energy travels in the form of electromagnetic waves or rays of photons, it is best to quantify the radiative heat transfer in form of radiative intensity. The radiative intensity is defined as the radiative energy flow per unit time, per unit area normal to the ray of radiation, per unit solid angle and per unit wavenumber and is the solution of the Radiative Transfer Equation [44]. The radiative energy traveling in a participating medium undergoes absorption, emission and scattering from the medium which changes the intensity of the radiation. A simple energy balance for a ray of radiation leads to Radiative Transfer Equation (RTE). RTE gives the intensity field inside a domain containing participating medium as function of spatial coordinates, direction and wavelength (frequency) and is expressed in general form as:

$$\frac{dI_\eta}{ds} = \kappa_\eta I_{b\eta} - \beta_\eta I_\eta + \frac{\sigma_{s\eta}}{4\pi} \int_{4\pi} I_\eta(\hat{s}_i) \Phi_\eta(\hat{s}_i, \hat{s}) d\Omega_i \tag{2.70}$$

where $\vec{s}$ is the unit direction vector, β_η is the spectral extinction coefficient which is sum of spectral absorption coefficient κ_η and spectral scattering coefficient $\sigma_{s\eta}$. The quantity $\Phi_\eta(\hat{s}_i, \hat{s})$ is the scattering phase function which describes the probability that a ray from a certain direction $\hat{s}_i$ is scattered into other direction $\hat{s}$. The first term on RHS of RTE is the augmentation of radiative intensity due to emission. Second term is attenuation of radiation due to scattering and absorption and third term describes the augmentation of radiation due to scattering of radiative intensity from other directions. The above integro-differential equation can be

simplified depending on the nature of the participating medium. Such as in lightly sooting flames scattering is negligible and eqn. 2.70 reduces to just a differential equation:

$$\frac{dI_\eta}{ds} = \kappa_\eta I_{b\eta} - \beta_\eta I_\eta \tag{2.71}$$

With proper boundary condition the above equation can be solved to obtain I_η and subsequently the heat flux vector in eqn. 2.69.

The accuracy of radiation calculation depends on the solution method used to solve the RTE and the accuracy of the radiative properties of the participating media. Hereafter just a brief description of the solution method of *P1* and the weighted-sum-of-gray-gases for evaluating spectral radiative properties is described.

P1 Radiation Model: P1 is a spherical harmonic method and is one of the models in the class of P-N method. It is based on the idea that the solution of RTE can be simplified by expressing the radiative intensity as orthogonal series of spherical harmonics which satisfy Laplace equation in spherical coordinates. The number of terms retained in the series expansion gives the method its order and name. So, P1 model means only first order term of the series expansion is retained. By this way the RTE is transformed into a set of simultaneous PDE's that are solved in a reacting flow. For detailed information on P1 and other radiation model please refer to [44].

The next part which affects the RTE is the radiative properties of the gas phase species involved in the combustion system. Generally, water vapor, carbon dioxide and carbon monoxide are important contributors to nonluminous radiation and the effect of NO_x and SO_x is not great as they are present in only small quantities [45]. Radiation from a flame is absorbed and emitted by participating media only at certain frequencies governed by the quantum mechanics. The radiative properties such as absorption coefficient tend to oscillate across the spectrum. Therefore approximate methods have been developed which predict the radiative properties and one of them is the Weighted-Sum-of-Gray-Gases (WSGG). In brief, WSGG replaces the nongray (functions of spectral properties) gases with number of gray gases. Radiative heat transfer rates are calculated independently by solving the RTE with weighted emissive powers for each gray gas [43, 45]. In FLUENT the P1 model with WSGG approach for radiative properties is used in calculating the radiative heat transfer from the flame.

2.8. COMPUTATIONAL MODEL FOR DROP SIZE DISTRIBUTION

This section discusses the different types of size distribution functions used to model drop size distribution. It highlights the empirical size distribution techniques namely: Root normal distribution, Log normal distribution, Rosin-Rammler distribution, Log Rosin-Rammler distribution, Nukiyama-Tanasawa distribution. Also a brief discussion about Maximum Entropy Formalism is presented. Further implementation of the Nukiyama-Tanasawa distribution in the DLR code- SPRAYSIM is discussed.

2.8.1. MATHEMATICAL AND EMPIRICAL REPRESENTATION OF SIZE DISTRIBUTION

Sprays produced by different atomizers contain a wide spectrum of drop diameters and the knowledge of this size distribution is vital for understanding the operation of the system. Different applications require different type of distribution ranging from narrow distribution (narrow drop diameter range)for respiratory sprays to wide distribution (wider drop diameter range) for gas turbines. Therefore, drop size distribution is equally important in spray literature apart from prediction of single diameter. Sprays produced by the atomization

process is highly diverse and distinct for each atomizer. There are various mechanisms involved such as jet and sheet disintegration processes which result in the formation of different diameters and the resulting main and satellite drops vary in size accordingly. This makes prediction of drop size distribution from first principles a difficult task and till date no theory has been able to completely describe this phenomena [46]. Because of this, there are many functional relations which are based on probability theory or purely empirical consideration to mathematically describe the drop size distribution. Some of the widely used mathematical correlations are: *Normal, Lognormal, Rosin-Rammler, Log Rosin-Rammler and Nukiyama-Tanasawa.* According to [46] mathematical functions should have the following characteristics to be of practical importance.

1. Provide satisfactory fit to the experimental data.

2. Be able to extrapolate to drop sizes outside the experimental range.

3. Permit easy calculation of mean drop size and other characteristic diameters.

4. In ideal situation, also be able to reflect the basic mechanisms involved in the atomization.

The fact that different type of functions are used is because they are formulated by fitting to wide variety of experimental data through empirical arguments. It is therefore necessary to test several of these distributions to find a right fit for the given experimental data. In the coming section, some of the mathematical and empirical functions will be discussed, but before that a brief account of different representations of size distribution will be discussed.

In principle there are multiple ways of representing the drop size data. Graphical representation of the drop size distribution is the more efficient way of expressing the data. Intuitively, range of drops produced by a given spray can be divided into set of classes, where each class consists of drop whose diameters are in the range of a given diameter, D i.e each class consists of drops whose diameters are in the range of $D - \Delta D$ and $D + \Delta D$. By counting the number of drops occurring in each class, a histogram of frequency of occurrence of a given class can be constructed. The continuous version of the histogram plot is called as the probability distribution function (PDF) of the drop size or also known as drop size distribution function. This type of PDF results in number based distribution (dN/dD).

If the volume of the drops rather than its number can be considered, yielding the volume based distribution (dQ/dD). Alternatively, the drop size distribution can also be represented as cumulative volume distribution ($Q(D)$). This is the integral representation of the volume based distribution and it informs the percentage of the total volume of the drops in a spray present below the given diameter D (for example, Q(D)=0.5% means 50% of the volume of the droplets is below a given diameter and this diameter is known as the mass median diameter).

It should also be mentioned here that the number based distribution is related to volume based distribution by eqn. 2.92 provided that the shape of the droplets are assumed to be spherical and have same density [47].

$$\frac{dQ}{dD} = \frac{D^3 \frac{dN}{dD}}{\int_0^\infty D^3 \frac{dN}{dD} d\tilde{D}} \tag{2.72}$$

As the cumulative volume distribution is the integral representation of volume based distribution, the cumulative volume distribution and volume based distribution are related to each other by the following equation.

$$Q(D) = \int_0^D \frac{dQ}{dD} d\tilde{D} \tag{2.73}$$

Following figure shows the number based, volume based and cumulative representation of the same size distribution (root normal) which has a Sauter mean diameter, SMD (defined as the diameter of the drop

whose ratio of volume to surface area is same as that of the entire spray)
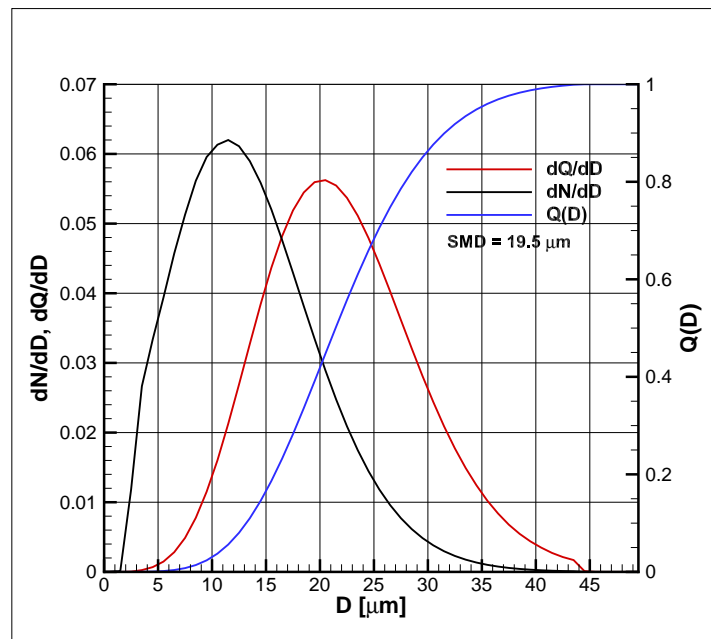

Figure 2.5: Different representations of drop size distribution

Figure 2.5 shows a typical size distribution generated from the SPRAYSIM software. In the volume based distribution, it can be seen that the the size distribution is cut-off at certain value to remove out the droplets which are very few in number and this cut-off is based on the minimum of two conditions: either the removed droplets' volume is not more than 0.05% of the total volume and the droplet diameter is not more than the specified value.

Some of the mathematical functions which are frequently used to represent drop size distribution are described below.

- **Root-Normal Distribution:** It is a relatively simple and robust relation to express drop size distribution. In root-normal distribution the size distribution which follows the Gaussian shape is scaled with square root of the drop diameter instead of linear scale for drop diameter [48]. For the sake of simplicity all the following distributions will be expressed in terms of cumulative volume distribution (Q).

$$Q(D) = \frac{1}{2}\left[1 + erf\left(\frac{1}{\sqrt{2}\sigma} \times \left(\sqrt{\frac{D}{D_{v,50}}} - 1\right)\right)\right] \quad (D > 0) \tag{2.74}$$

  where σ is the standard deviation and $D_{v,50}$ is the mass median diameter and *erf()* is the error function defined as:

$$erf(x) = \frac{2}{\sqrt{\pi}} \int_0^x e^{-t^2} dt \tag{2.75}$$

- **Log-normal Distribution:** Many particle size distribution follow a Gaussian distribution law and can be represented as Gaussian distribution if the log of the particle diameter is taken as a variable [46]. By doing so the cumulative volume distribution for Log-normal distribution looks like:

$$Q(D) = \frac{1}{2}\left[1 + erf\left(\frac{1}{\sqrt{2}\sigma} \times \left(ln\left(\frac{D}{D_{v,50}}\right) - 1\right)\right)\right] \quad (D > 0) \tag{2.76}$$

  where σ is the standard deviation and $D_{v,50}$ is the mass median diameter.

- **Rosin-Rammler Distribution:** It is one of the widely used empirical size distribution for sprays. Originally developed for size distribution of coal particles, it is also being used to describe the liquid spray size distribution successfully [49]. Rosin-Rammler is a mathematical function depending on only two parameters namely a characteristic diameter and a width parameter. This mathematical simplicity to describe the complex size distribution just by two parameters makes it widely popular in the spray literature. The Rosin-Rammler distribution is represented as:

$$Q(D) = 1 - exp\left(-\left(\frac{D}{\overline{D}}\right)^q\right) \tag{2.77}$$

  where q is the width parameter representing width of the sizes in the size distribution. If value of q is higher, then the droplet size is more uniform and in the limit of q tending to infinity the drop size distribution becomes mono-disperse. And $\overline{D}$ is a characteristic diameter of the size distribution and originally $D_{v,63.2}$ is used. However, in the SPRAYSIM code $D_{v,50}$ is used which leads to a different pre-factor in the exponential term (other than -1) as shown:

$$Q(D) = 1 - exp\left(ln(0.5)\left(\frac{D}{D_{v,50}}\right)^q\right) \tag{2.78}$$

  The result with $D_{v,50}$ was obtained in the previous works at DLR, Institute of Combustion Technology.

- **Log Rosin-Rammler Distribution:** As it was found earlier with the log normal distribution that using

log of the diameter as variable could represent the experimental data adequately it was also found with the Rosin-Rammler distribution. It was found that the fit obtained from the original Rosin-Rammler distribution from pressure swirl nozzle deviated for larger drops and it could be remedied by using the log of the diameter as shown below:

$$Q(D) = 1 - exp\left(-\frac{ln(D)}{ln(\overline{D})}\right)^{q}$$
(2.79)

where again the parameters q and $\overline{D}$ have the same meaning as in original Rosin-Rammler distribution and where $D_{v,50}$ is used for the characteristic diameter.

- **Log-hyperbolic function:** Log-hyperbolic is another empirical relation for describing the drop size distribution of sprays. It was developed by Bhatia et al. [50] to describe the size distribution characteristics obtained from the spray of a oil burner nozzle. It contains of 4 parameters (α, δ, μ, β,) and is shown in the following equation:

$$\frac{dN}{dD} = a(\alpha\beta\delta) \, exp\left\{-\alpha\sqrt{\delta^2 + (D-\mu)^2} + \beta(D-\mu)\right\}$$
(2.80)

where a is the normalizing constant given by

$$a = \frac{\sqrt{\alpha^2 - \beta^2}}{2\alpha\delta K_1\left(\delta\sqrt{\alpha^2 - \beta^2}\right)}$$
(2.81)

δ is the scale parameter, μ is the location parameter and other two parameters α & β, define the shape of the PDF. As it can be seen, this method requires information of 4 parameters to successfully fit the experimental data and this makes it difficult to work with. Also, according to [51], the computation of parameters leads to instability and makes the usage even more cumbersome.

- **Nukiyama-Tanasawa Distribution:** Nukiyama-Tanasawa distribution was originally conceived by Nukiyama and Tanasawa to describe the number based drop size distribution of spray produced by a pneumatic atomizer in 1939 [52]. It is an empirical relation consisting of 3 independent parameters namely *b, p and q* which adequately describe the drop size distribution and is shown in the following equation:

$$\frac{dN}{dD} = a \, D^p \, exp[-bD^q]$$
(2.82)

where b, p and q control the width of the distribution and the location of the mean and a is the normalizing constant given as:

$$a = \frac{qb^{\frac{p+1}{q}}}{\Gamma\left(\frac{p+1}{q}\right)}$$
(2.83)

As seen from above, there are different mathematical relations to describe a drop size distribution produced by a spray, the question which generally arises is, which of the above is a better choice?. Paloposki in his work used χ^2 test to analyze the drop size distribution from 22 data sets among which some of them were considered as benchmark data sets [53]. Paloposki concluded that the Nukiyama-Tanasawa and log hyperbolic relations provided the best fit to the experimental data sets which he used as compared to others. Another result which was of importance was that: as the number of the parameters describing the size distribution increased, the fit provided by the method to the experimental data was

better. This is evident, as more independent parameters give the freedom to better fit the experimental data. With this recommendation it was considered to include the Nukiyama-Tanasawa method in the SPRAYSIM software. While the log hyperbolic method is also mentioned, numerical fitting of the four parameters of the complicated log-hyperbolic function is difficult [51]. Thus the implementation of it in SPRAYSIM was dropped.

From the literature survey, it was observed that the original Nukiyama-Tanasawa distribution is used in different ways which are either a modification or simplification of the original equation (eqn. 2.82). One of the widely used variant is due to Mugele & Evans [52] where in the value of the independent parameter p is taken to be fixed at 2 which essentially reduces this variant to a 2 parameter distribution. The equation for size distribution is shown below:

$$\frac{dN}{dD} = a\, D^2\, exp[-(bD)^q] \tag{2.84}$$

Another variant of the method is given by Paloposki [54] where in the parameter 'p' is assumed to be equal to $1/q$. By doing so, the size distribution can be defined only by 2 independent parameters. The size distribution can be expressed by the following equation:

$$\frac{dN}{dD} = a\, D^{1/q}\, exp[-(bD)^q] \tag{2.85}$$

The third variant of Nukiyama-Tanasawa method is given by Gonzalez [47]. In this work, effort was made to make the method fit the experimental data by using the Sauter Mean Diameter (SMD) from the measured data for a spray. Along with SMD, p and q are the other two parameters which completely define a size distribution. The number based distribution is shown below:

$$\frac{dN}{dD} = \frac{q}{SMD\,\Gamma\left(\frac{p+1}{q}\right)} \left(\frac{\Gamma\left(\frac{p+4}{q}\right)}{\Gamma\left(\frac{p+3}{q}\right)}\right)^{p+1} \times \left(\frac{D}{SMD}\right)^p exp\left[-\left(\frac{\Gamma\left(\frac{p+4}{q}\right)}{\Gamma\left(\frac{p+3}{q}\right)}\right)^q \left(\frac{D}{SMD}\right)^q\right] \tag{2.86}$$

where $\Gamma()$ is the complete gamma function defined as shown in eqn. 2.87. In the following section, the implementation of the aforementioned variants of Nukiyama-Tanasawa empirical method in SPRAYSIM is explained.

$$\Gamma(z) = \int_0^\infty t^{z-1}\, e^{-t}\, dt \tag{2.87}$$

Eqn. 2.86 is mathematically equivalent formulation of eqn. 2.82 and not a simplification. SMD is related to other parameters as:

$$SMD = \frac{1}{b^{1/q}} \left(\frac{\Gamma\left(\frac{p+4}{q}\right)}{\Gamma\left(\frac{p+3}{q}\right)}\right) \tag{2.88}$$

2.8.2. IMPLEMENTATION OF NUKIYAMA-TANASAWA DISTRIBUTION IN SPRAYSIM

This section describes the implementation of Nukiyama-Tanasawa variants in the spray software SPRAYSIM. From section 2.8.1 it can be seen that the Nukiyama-Tanasawa variants are given in number based distribution and other representations are also required to completely evaluate the spray. Thus the first step was to convert this number based distribution to volume based and cumulative distribution. As mentioned previously all the variants of Nukiyama-Tanasawa distribution are based on the basic version of the distribution (eqn. 2.82) and in order to be more informative, the parameter b in (eqn. 2.82) is replaced by D_{ref} which

scales with the variable D and this is shown in the following equation.

$$\frac{dN}{dD} = a_N \, D^p \, exp\left[-\left(\frac{D}{D_{ref}}\right)^q\right]$$

(2.89)

The above equation is mathematically equivalent to eqn. 2.82 where parameter b is related to D_{ref} by:

$$b = \frac{1}{D_{ref}^q}$$

(2.90)

The normalizing constant a is related to other independent parameters. The derivation for this is shown in the appendix. The final form is given below:

$$a_N = \frac{q}{D_{ref}^{p+1} \, \Gamma\left(\frac{p+1}{q}\right)}$$

(2.91)

where $\Gamma()$ is a complete gamma function which is defined in eqn. 2.87. With the number based distribution derived, now the volume based distribution is derived. Assuming all the particles to have same spherical shape and density, the volume based distribution is related to the number based distribution in the following way:

$$\frac{dQ}{dD} = \frac{D^3 \frac{dN}{dD}}{\int_0^\infty D^3 \frac{dN}{dD} d\tilde{D}}$$

(2.92)

By using the above relation the volume based distribution function is derived. The complete derivation can be found in the appendix and the final form is given below:

$$\frac{dQ}{dD} = \frac{q}{D_{ref}^{p+4} \, \Gamma\left(\frac{p+4}{q}\right)} \, D^{p+3} \, exp\left[-\left(\frac{D}{D_{ref}}\right)^q\right]$$

(2.93)

where again $\Gamma()$ is the complete gamma function. Finally, the cumulative distribution is derived. Cumulative distribution is defined as the integral of the volume based distribution over all the diameters of the distribution. Cumulative distribution can be obtained from the volume based distribution in the following way

$$Q(D) = \int_0^D \frac{dQ}{dD} d\tilde{D}$$

(2.94)

With the above relation the integration is carried out and the derivation is shown in the appendix. The final result is shown below:

$$Q(D) = P\left(\frac{p+4}{q}, \left(\frac{D}{D_{ref}}\right)^q\right) \quad (q > 0)$$

(2.95)

where P() is the incomplete gamma function which is defined as:

$$P(a, D) = \frac{1}{\Gamma(a)} \int_0^D t^{z-1} \, e^{-t} dt \qquad (a > 0)$$

(2.96)

Eqn. 2.95 is the generalized function to obtain the cumulative distribution. It differs for each variant of the Nukiyama-Tanasawa distribution as the independent parameters are different for each of these variants. Table 2.2 shows the implementation of four variants (including the original version of the distribution) in SPRAYSIM. Other representations (dN/dD, dQ/dD) are also implemented in the SPRAYSIM code. The derivation for these representations are shown in appendix and for each variant they can be obtained by substituting respective parameter values. As we can see that to compute the cumulative distribution, values of complete

Table 2.2: Nukiyama variants implemented in SPRAYSIM

Type	Size Distribution Function	Cumulative Distribution, Q(D)	Independent Parameters
Nuki Original	Eqn.2.82	$Q(D) = P\left(\frac{p+4}{q}, \left(\frac{D}{D_{ref}}\right)^q\right)$	D_{ref}, p, q
Nuki A	Eqn.2.84	$Q(D) = P\left(\frac{2+4}{q}, \left(\frac{D}{D_{ref}}\right)^q\right)$	D_{ref}, q
Nuki B	Eqn.2.85	$Q(D) = P\left(\frac{1/q+4}{q}, \left(\frac{D}{D_{ref}}\right)^q\right)$	D_{ref}, q
Nuki C	Eqn.2.86	$Q(D) = P\left(\frac{p+4}{q}, \left(\frac{D}{D_{ref}}\right)^q\right)$	SMD, p, q

and incomplete gamma function is needed. Complete gamma function and the incomplete gamma functions were coded in FORTRAN 95 with some minor modifications to avoid underflow and overflow of the values computed during the computation of these functions. These codes were based on the code given in [55]. According to the definition of the complete gamma function, the function is defined only when $a > 0$ and this imposes the following parameter space shown in table 2.3 for the independent parameters to obtain physical values of the size distribution.

Table 2.3: Possible parameter values for Nukiyama-Tanasawa variants

Type	Parameter Space
Nuki A	p = 2, q > 0
Nuki B	$p = 1/q, q > \frac{-1}{4}, q \neq 0$
Nuki C	$p > -1, q > 0; p < -4, q < 0, q \neq 0$

After the implementation of these codes, an optimization routine is implemented. This is done because, suppose the characteristic diameters of a size distribution for example only SMD and MMD (mass median diameter) are known (either from experimental or from empirical relationships) and a Nukiyama-Tanasawa distribution needs to be fit to these user-prescribed characteristic diameters. Nukiyama-Tanasawa distribution with different parameter values can be tried to fit to the user-prescribed diameters. Thus in order to find the optimum values of the parameters an optimizing routine is used. By using this routine an optimum size distribution is generated such that the standard deviation ($dgoal$) (weighted) of the difference of the optimized size distribution and the user-prescribed characteristic diameters ($d10 \cdots d32, d_{v1} \cdots d_{vn}$) is minimum as shown in eqn. 2.97.

$$dgoal = \left(\frac{((d10 - d10_{NT})w10)^2 + \cdots + ((d32 - d32_{NT})w32)^2 + \left((d_{v1} - d_{v1,NT})w_{v1}\right)^2 \cdots + \left((d_{vn} - d_{vn,NT})w_{vn}\right)^2}{w10^2 + w20^2 + w30^2 + w32^2 + w_{v1}^2 + \cdots + w_{vn}^2}\right)^{1/2}$$

(2.97)

where $d10_{NT} \cdots d32_{NT}, d_{v1,NT} \cdots d_{vn,NT}$ are the characteristic diameters from the optimized size distribution and $w_{10}, w_{20} \cdots$ are the weighting factors which are non-negative numbers (≥ 0) and the value of zero means that its characteristic diameter will not influence the eqn. 2.97.

As we see from the previous section, the independent parameters in the three variants are different. Thus the optimizing routine which finds the optimum parameters is slightly different namely: for eqn. 2.84 and eqn. 2.85 the parameters D_{ref} and q are optimized and for eqn. 2.86 since the SMD is used as a parameter which is taken from the experiments, the independent parameters of p and q are optimized. For the original representation of Nukiyama-Tanasawa distribution (eqn. 2.82) parameters p and q are optimized by holding the mass median diameter $D_{v,50}$ constant which is related to D_{ref}. Along with Nukiyama-Tanasawa distribution optimization has already been implemented for other size distribution functions mentioned in section 2.8.1 by DLR, Institute of Combustion Technology. All the size distribution functions are tested in the current study to obtain a size distribution which best describes the experimental data.

2.8.3. MAXIMUM ENTROPY FORMALISM

This section discusses the Maximum Entropy Formulation (MEF) to describe the drop size distribution in sprays. Although this approach has not been used in this thesis work, this is a novel research area and hence a brief account of this method is described hereafter.

Maximum Entropy Formalism is a statistical tool to predict the least biased drop size probability distribution function that satisfies the set of constraints expressing the available information related to the distribution sought. In order to obtain the PDF, the information regarding the PDF sought is to be known and this information is written as constraints (in terms of the mean diameter of the PDF). The PDF which satisfies the constraints is the one which has maximum uncertainty. According to Shannon's entropy principle, for a set of m states, each of them having probability, p_i, the uncertainty of the probability distribution is given by:

$$S = -k \sum_{i=1}^{m} p_i \, ln\left(p_i\right) \tag{2.98}$$

Eqn. 2.98 is similar to the entropy from statistical thermodynamics and hence S is called the Shannon's entropy. For a continuous variable, the probability distribution becomes probability density function f whose entropy is written as:

$$S = -k \int_0^\infty f\left(D\right) ln\left[f\left(D\right)\right] dD \tag{2.99}$$

Earlier methods of MEF principle were based on the information obtained from experimental work and hence they were not purely theoretical approach in predicting the drop size PDF. This was overcome by Cousin et al.[56] where the MEF was derived with constraints based on one mean drop diameter obtained from the classical linear stability analysis. But with this approach the number based distribution prediction was unphysical towards lower diameter ranges as the number distribution did not approach zero as the drop diameter went to zero. Dumouchel et al. [57] developed the work of Cousin et al.[56] and is discussed here briefly because of its insight on relationship of MEF with Nukiyama-Tanasawa distribution. In this work an interesting observation was made by Dumouchel. With the newly derived number based drop size distribution they were able to relate it to Nukiyama-Tanasawa distribution function thereby making Nukiyama-Tanasawa distribution no longer empirical in nature. Dumouchel derived the number based PDF using the statistical mechanics and by subjecting to following simple constraints irrespective of which atomization mechanism is at play.

A large ensemble of N drops is considered. The droplet diameter space is divided into droplet classes with the median diameter D_i and the width ΔD_i. With MEF, the aim is to determine the number of drops contained in each diameter class, N_i.

1. The numbers of droplets is fixed.

$$\sum_{i=1}^{\infty} N_i = N \tag{2.100}$$

2. Existence of finite drop diameter: Aerodynamic forces are always present and tend to break the large diameters to small diameters. In statistical sense, all the moments of the distribution must be finite and as these moments define the mean diameters of the distribution the following sum must be a positive constant for each value of q.

$$\sum_{i=1}^{\infty} \frac{N_i}{N} D_i^q = D_{q0}^q \tag{2.101}$$

3. Existence of minimum drop diameter: Surface tension forces exist in all liquids and when the droplet gets very small the surface tension forces becomes far greater than the aerodynamic forces and hence

minimum drop size exists. This also means that producing zero diameter particles would mean infinite energy input and on other hand producing infinite size particle would mean no energy input. In any case, this means the probability of any diameter class is not equally likely. Thus this limitation of drop size is modeled as diameter-class probability distribution increasing with diameter.

$$g_i = A D_i^{a-1} \tag{2.102}$$

where A is assumed to be a constant and $a \geq 1$

With the constraints defined, W is computed, defined as the number of ways in which N particles can be distributed, if N_i of all the particles are in class i, and if number of ways a particle can reach class i is proportional to g_i. In short, W is the number of possible arrangements of N droplets in infinite number of classes whose occurrence is given by g_i:

$$W = N \prod_{i=1}^{\infty} \left(\frac{g_i^{N_i}}{N_i} \right) \tag{2.103}$$

The distribution N_i which is sought here, is the one which maximizes W and therefore has maximum entropy given in eqn. 2.104.

$$S = k \, log \, (W) \tag{2.104}$$

The maximization of S by subjecting to eqn. 2.100 and eqn. 2.101 the following number based distribution is obtained.

$$\frac{dN}{dD} = \frac{q}{\Gamma\left(\frac{a}{q}\right)} \left(\frac{a}{q}\right)^{\frac{a}{q}} \frac{D^{a-1}}{D_{q0}^a} \, exp\left(-\frac{a}{q}\left(\frac{D}{D_{q0}}\right)^q\right) \tag{2.105}$$

As mentioned earlier, in this work, the drop size distribution obtained from the MEF principle was equivalent to the Nukiyama-Tanasawa distribution. The Nukiyama-Tanasawa distribution (eqn. 2.82) is equivalent to number based distribution of MEF (eqn. 2.105) if:

$$\begin{cases} q = q \\ p = a - 1 \\ b = \frac{a}{q \, D_{q0}^q} \end{cases} \tag{2.106}$$

By making use of eqn. 2.106 and eqn. 2.91, it can be shown that the normalizing constant of Nukiyama-Tanasawa distribution is analogous to the normalizing constant of the eqn.. 2.105. Thus the Nukiyama-Tanasawa distribution is not just an empirical relation but a theoretical relation which follows from the MEF approach given above.

3

NUMERICAL SIMULATION OF DLR MGT BURNER WITH ANSYS CFX AND SPRAYSIM

The numerical simulation of the two-phase flow was performed by coupling the DLR liquid phase simulation code SPRAYSIM with the commercial CFD-code ANSYS CFX-16.1. The gasfield simulation was calculated using the finite volume code of CFX, whereas the Lagrangian particle tracking of the droplets was performed by SPRAYSIM. The two-way coupling of both codes with the exchange of the gasfields and the spray feedback source terms was done via interface routines using the User Fortran feature of CFX.

The Fortran95-code SPRAYSIM is the development platform of the DLR Institute of Combustion Technology for unsteady or steady Lagrangian particle simulation [15, 16, 32, 58–61]. It is designed basically as a standalone code running both under LINUX and WINDOWS, that can be coupled via files or online coupling via function-calls to CFD gas field codes. The code is MPI parallelized in the number of computational particles ('parcels'). The particle tracking happens on domains with unstructured grids employing a predictor-corrector solver for the ordinary differential equations. Models for turbulent particle dispersion, atomization and multicomponent evaporation are implemented in the code. SPRAYSIM employs registration planes, where computational parcels that pass these planes are registered during the tracing. The individual parcel data are accumulated and finally processed to obtain distributions and profiles of characteristic spray diameters, size distributions, liquid fluxes, spray velocities, temperatures, etc.

This chapter is structured as follows: section 3.1 discusses the numerical simulation of the spray combustion of the DLR MGT burner (nozzle 6). Then the determination of boundary conditions for gas phase and spray droplets are explained. Further, initial trials of simulating the entire combustion chamber (injection nozzle to outlet) and the outcome of the simulations are discussed. Section 3.2 discusses the numerical investigation of only the combustion chamber and the reason for doing this is elucidated. For the CFD simulation of turbulent spray combustion, the turbulence is modeled by Shear Stress Transport (SST) and the combustion model of combined Eddy Dissipation and Finite Rate Chemistry is used. The turbulent particle dispersion is simulated by the spectral dispersion model of Blümcke [41]. Liquid fuel evaporation is modeled through the Abramzon-Sirignano model implemented in SPRAYSIM. The fuel used is light heating oil (referred to in this work as DF2). The property tables and the NASA polynomial for DF2/light heating oil

have been kindly provided by M. Rachner (DLR, Institute of Combustion Technology). They were generated based on formulas and data values compiled from the literature. The results obtained from the simulation is discussed and conclusions for this are drawn. [1]

3.1. FULL DOMAIN SIMULATIONS

For numerical simulation, the computational domain is derived from the combustor which is experimentally investigated in this study. Combustion chamber length from the exit of mixing tube is 218.5 mm and the radius of the combustion chamber is 34 mm. To reduce the computational cost, the computational domain is limited to a sector of 22.5°. The axial extent can be seen in Fig. 3.1. The boundary conditions for the
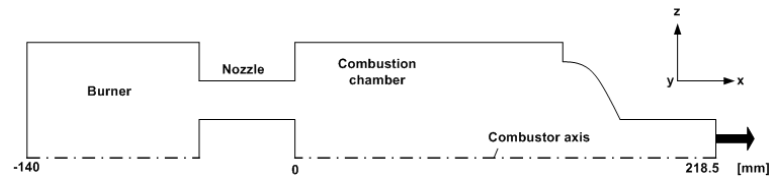

Figure 3.1: Computational domain for CFD simulations

simulation are given in Table 3.1. The coordinate system chosen for simulation is such that the origin is at the exit of the mixing tube and the injection nozzle is located at x = -139 mm. An unstructured mesh with

Table 3.1: Boundary Conditions for nozzle 6

Parameter	Value
Pressure (bar)	3.5
$T_{air}(K)$	573
λ_G	1.45
$V_{bulk}(m/s)$	120
$P_{th}(kW)$	186
$T_{fuel}(K)$	310
Fuel mass flow rate over 8 nozzles (g/s)	4.3
Air mass flow rate over 8 nozzles (g/s)	91.4

hexahedral cells was used for the grid generation in the entire domain. Mass flow inlet boundary condition was applied for the air inlet and pressure outlet was applied for the outlet. Liquid fuel droplets were injected through the injection file obtained from SPRAYSIM.

With regards to spray boundary conditions, the initial conditions for droplet size and velocity are mentioned below. The nozzle used for the experiment was a pressure atomizer without swirl manufactured by Steinen. Computational parcels were started 0.5 mm downstream of the injection nozzle from 10 particle location classes equidistantly spaced in a circle and the injection direction for each particle location is obtained from the axial and radial position of the location class as shown in Fig. 3.2 such that the final location class will have the spray half angle of 22.5°. All the parcels starting from different location classes were given the following initial conditions.

---

[1] Content of this chapter has been published in the following Conference:
Gounder et al. Experimental and numerical investigation of spray characteristics in a new FLOX® based combustor for liquid fuels for Micro Gas Turbine Range Extender (MGT-REX), 52nd AIAA/SAE/ASEE Joint Propulsion Conference, Salt Lake City, Ohio, USA
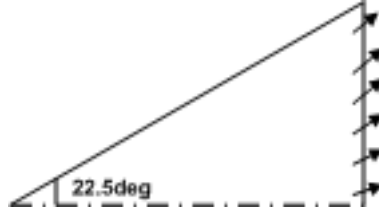
Figure 3.2: Injection direction for particle starting locations

3.1.1. INITIAL DROPLET SIZE

Several empirical relations exist in the literature to predict the SMD of the size distribution for different type of atomizers based on certain geometric and flow parameters [62, 63]. The empirical relation for pressure nozzles from chapter 6.16 of [62] was used to obtain the SMD of the size distribution and is given in eqn. 3.1.

$$SMD = 2.25 \, \sigma^{0.25} \, \mu_L^{0.25} \, \dot{m}^{0.25} \, \Delta P_L^{-0.5} \, \rho_A^{-0.25} \tag{3.1}$$

In the eqn. 3.1, the pressure drop over nozzle was obtained for the given fuel mass flow from the technical data provided by the nozzle manufacturer, Steinen. The values of parameters used in eqn. 3.1 are listed in Table 3.2.

Table 3.2: Parameters for eqn. 3.1 at 573 K

$\rho_{air}(kg/m^3)$	0.667
$\mu_{fuel}(kg/m \cdot s)$	0.0023
$\sigma_{fuel}(N/m)$	0.0233
$\dot{m}_{fuel}(kg/s)$	0.5375e-3
$\Delta P_L(Pa)$	3886050

SMD of 91.54 μm was obtained from eqn. 3.1. Width of the size distribution which is defined by the ratio MMD/SMD was chosen to be 1.13 which is the most frequently occurring width for gas turbine combustors [49]. With two characteristic diameters (MMD & SMD) a root normal distribution was prescribed for all the radial particle starting location classes.

3.1.2. INITIAL DROPLET VELOCITY

The nominal droplet axial velocity was obtained from the nozzle fuel mass flow rate according to eqn. 3.2

$$\dot{m} = \rho \, A \, u \tag{3.2}$$

The density of the fuel was computed at 310K (from the property tables provided by the DLR, Institute of Combustion Technology) and the area was calculated from the diameter of the nozzle. Radial velocity for the droplets starting in different location classes were obtained from the axial velocity and the spray angles for every particle location class (Fig. 3.2).

From the above gas and spray boundary conditions, a cold (without combustion) steady-state simulation with SST turbulence model and Lagrangian particle tracking by SPRAYSIM was carried out and the spray characteristics at the first measurement position namely at x = 4 mm were analyzed. This was possible as the measurements suggested that the approximate flame lift-off height was in between 15-20 mm and therefore at x = 4 mm (143 mm from the droplet injection) no flame was seen and could be considered to be relatively cold. The simulation showed that the droplet SMD at x = 4 mm was nearly unchanged (Fig. 3.3a) while the

measurements showed that the droplet SMD was around $19 \mu m$ there. Moreover, the aerodynamic Weber number obtained from eqn. 3.3 was greater than the We_{crit}. We_{crit} is the gas Weber number above which the breakup occurs as suggested in [38] and references therein. This indicated that the secondary breakup should occur in the mixing chamber.

$$We = \frac{\rho_{gas} v_{rel}^2 d}{\sigma} \tag{3.3}$$

Based on the above observation a Cascade Atomization Breakup (CAB) [38] which is already employed in the

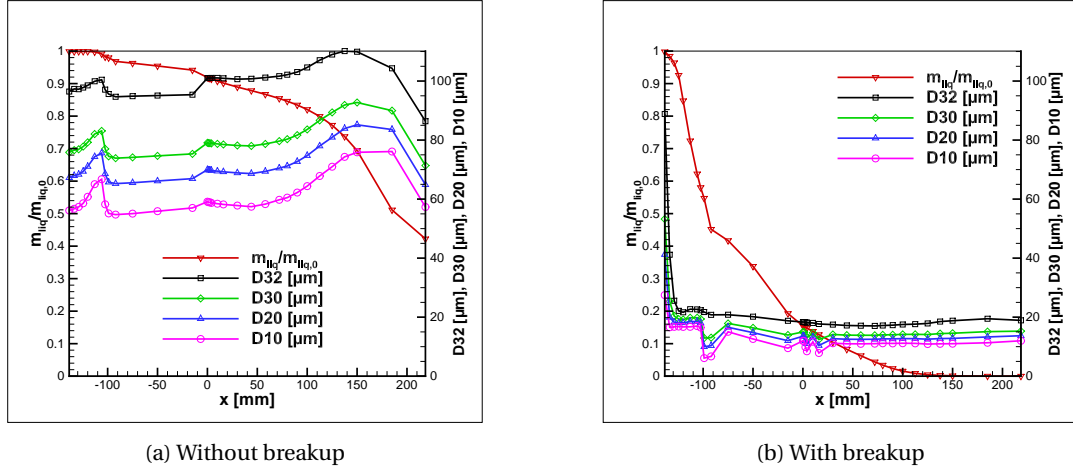(a) Without breakup   (b) With breakup

Figure 3.3: Comparison of normalized liquid mass flow with and without sec. breakup

SPRAYSIM was used to model the secondary breakup of the droplets. With CAB model it was found that the breakup completed inside the mixing chamber and the normalized liquid mass flow rate at the exit of the mixing pipe was as low as ≈0.2 while the SMD was around 17 μm as seen in Fig. 3.3b. The CAB model was found to be very sensitive to the breakup constant used in the model and the normalized liquid mass flow and characteristic diameters changed with the change in the CAB model constant. Therefore it required a more rigorous analysis of the secondary atomization behavior and was thus not used.

Further, with the cold simulation, another important aspect about the flow was studied: cooling air flow into the combustion chamber. The total inlet air mass flow entering the geometry was split into primary airflow, which flows through the mixing chamber, mixing pipe and then into the combustion chamber and the remaining part into the cooling air mass flow, which enters the combustion chamber through a circumferential slot. The mass flow of this cooling air was not measured during the experiments and in the simulation it was determined through the comparison of the computed maximum axial velocity of the small droplets (d< $5\mu m$) from cold simulation at x = 4 mm with the experimental values of small droplets there. The fraction of the air which was used for cooling flow was determined as 0.164. This comparison was possible because a) the experiments showed that the flame lift-off height was in the range of 15-20 mm and therefore at x = 4 mm the flow was still cold b) the cold simulation showed that the maximum axial velocity of the small droplets and the gas phase had nearly the same value at x = 0 mm and at x = 4 mm.

As the secondary breakup model was not able to predict appropriate droplet sizes, the droplet size boundary condition was changed with the value of SMD of 19.5 μm which was the SMD of the droplets observed at x = 4 mm from measurements. A rootnormal type of size distribution with a width of 1.10 was employed as this type of size distribution predicted satisfactory results at x = 4 mm when compared to measurements there. Subsequently, with the split applied for the mass flow rate and the droplet size boundary condition

a hot simulation (with combustion) was carried out for the complete domain with SST two-equation model for turbulence and 1-step global reaction kinetic (eqn. 2.28) with EDM/FRC turbulence-chemistry interaction model. The EDM/FRC model predicted too early onset of heat release as eary as in the mixing chamber whereas the measurements showed that flame was only visible in the combustion chamber far downstream of the mixing chamber. Therefore, in further investigation, the hot simulation (with combustion) was only performed in the combustion chamber. The initial conditions for gas field and spray profiles for the hot simulation was obtained from the computed cold simulations at the exit of the mixing pipe (nozzle)at x = 0 mm.

3.2. Combustion Chamber Simulation

As discussed in section 3.1 to eliminate the early onset of heat release predicted by the EDM/FRC model, the numerical simulation was performed with computational domain consisting of only the combustion chamber downstream of the mixing pipe. The initial conditions for the gas field and the radial profiles of spray (mean and rms of axial and radial velocities, mean and rms temperature) was obtained from CFX from cold simulation at x = 0 mm. A steady RANS computation was performed and important aspects of both the gas phase and dispersed phase were observed. Following sections present the detailed discussion of the results.

3.2.1. Liquid mass flow evolution

One of the measure of the vaporization rate is the streamwise development of the liquid mass flow. Fig. 3.4 shows the evaporation progress of liquid mass flow normalized by the initial liquid mass flow for the simulations with and without combustion from the injector (x=-139 mm) to the outlet of the combustion chamber. Evaporation rate is significant in the mixing chamber as the oxidizing air is preheated to 573 K. Subsequently, the evaporation rate is relatively reduced in the mixing pipe because of reduced residence times of the particles due to higher gas phase velocity. From the cold simulation, at x = 0 mm it can be observed that the normalized liquid mass flow rate has a value of 0.336 corresponding to almost $2/3^{rd}$ of the flow evaporation before entering the combustion chamber. Also, the cold simulation curve shows enhanced evaporation in the combustion chamber due to longer residence times of the particles due to lower gas velocity as compared to the mixing pipe. In the hot simulation, value of 0.336 was used as liquid mass flow value to generate the droplet injection file in SPRAYSIM. Subsequently, the hot simulation curve shows significant evaporation due to the combustion. At x = 100 and 120 mm the normalized liquid mass flow rate has a value of 0.0196 and 0.0073 showing that hardly any droplets are seen past x = 120 mm. This was in good agreement with the experimental data where it was also observed that no droplets were seen past x = 120 mm in Mie scattering. Moreover, it can also be observed that no droplet reaches the outlet through the droplet trajectory plot in Fig. 3.13.
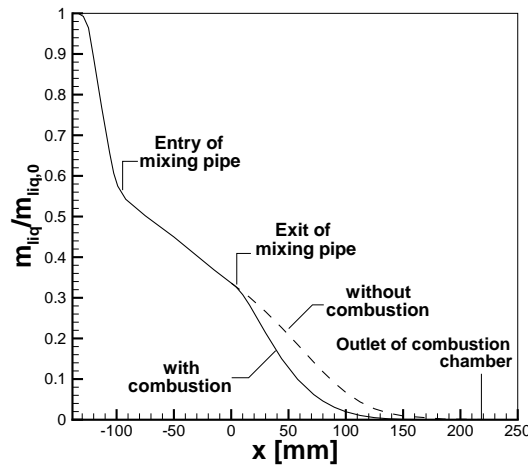
Figure 3.4: Axial development of normalized liquid mass flow rate

3.2.2. AXIAL AND MEAN AND RMS VELOCITY PROFILES

As no gas phase velocity measurements (mentioned in section 1.1) were done and only conditioned droplet velocity were measured at different axial locations until x = 72 mm. Fig. 3.5 shows the comparison of calculated (both gas and droplet velocities) and measured radial profiles of mean and rms axial velocity. The calculated mean and rms profiles predict a similar trend (shape) as compared to the measurements but the magnitude of the velocity is predicted inaccurately. At x = 4 mm, the mean axial velocity at the centerline has a velocity of 125.0 m/s which is slightly higher than the measured value. This is due to the early heat release predicted by the combustion model and the slow radial expansion of the jet predicted by the turbulence model. The slip velocity is defined as the difference between mean velocity of the droplets and the gas phase, $u_s = u_d - u_g$. At x = 4 mm, droplets in the size class $15 < d \leq 25$ μm are lagging behind the gas phase due to their inertia indicating negative slip velocity in the jet core as shown in Fig. 3.5. These large droplets attain positive slip velocity beyond r = ± 3.5 mm when compared to r = ± 2 mm as observed by measurements and this could be partly due to the turbulent dispersion which the droplets experience and partly due to the heat release predicted by the combustion model where the gradient of temperature might be slightly different compared to the experimental case. At increasing downstream distance (at x = 72 mm) the simulated mean axial velocities have higher values close to the centerline than measured values there. The decay of the centerline velocity in the simulations conforms to the measured mean velocity profile at higher downstream distance around ~120 mm which is not shown here indicating slower spreading rate of the jet predicted by the calculations.

Calculated RMS axial velocity profiles at all measured locations show a similar trend with respect to measurements: low magnitude of fluctuations in the jet core and fluctuations increase in the shear layer (r > 2 mm). However, the magnitude of the calculated fluctuation velocity is under-predicted at all locations compared to measurements. Moreover, experimental u' at x = 72 mm is nearly constant across the jet, but in the numerical simulation this characteristic is observed only at x = 120 mm (not shown here). Both mean and RMS calculated axial velocity profiles shows that the turbulent kinetic energy prediction by the turbulence model is inaccurate and thus turbulent intensity prediction. Also, in the two-equation SST turbulence model used in this simulation, the two way turbulent coupling was not included where the modulation of turbulence from the droplets is considered and this can also be a factor in describing the proper spreading of the

jet. Another reason which could also lead to inaccurate spreading of the jet is the heat release prediction by the combustion model. Inaccurate prediction of the temperature field leads to inaccurate prediction of velocity, as the temperature field affects the local density of the gas mixture (ideal gas law) and thereby affects the velocity field. All these reasons are investigated in the further section where simulations with different turbulence and TCI models are carried out.
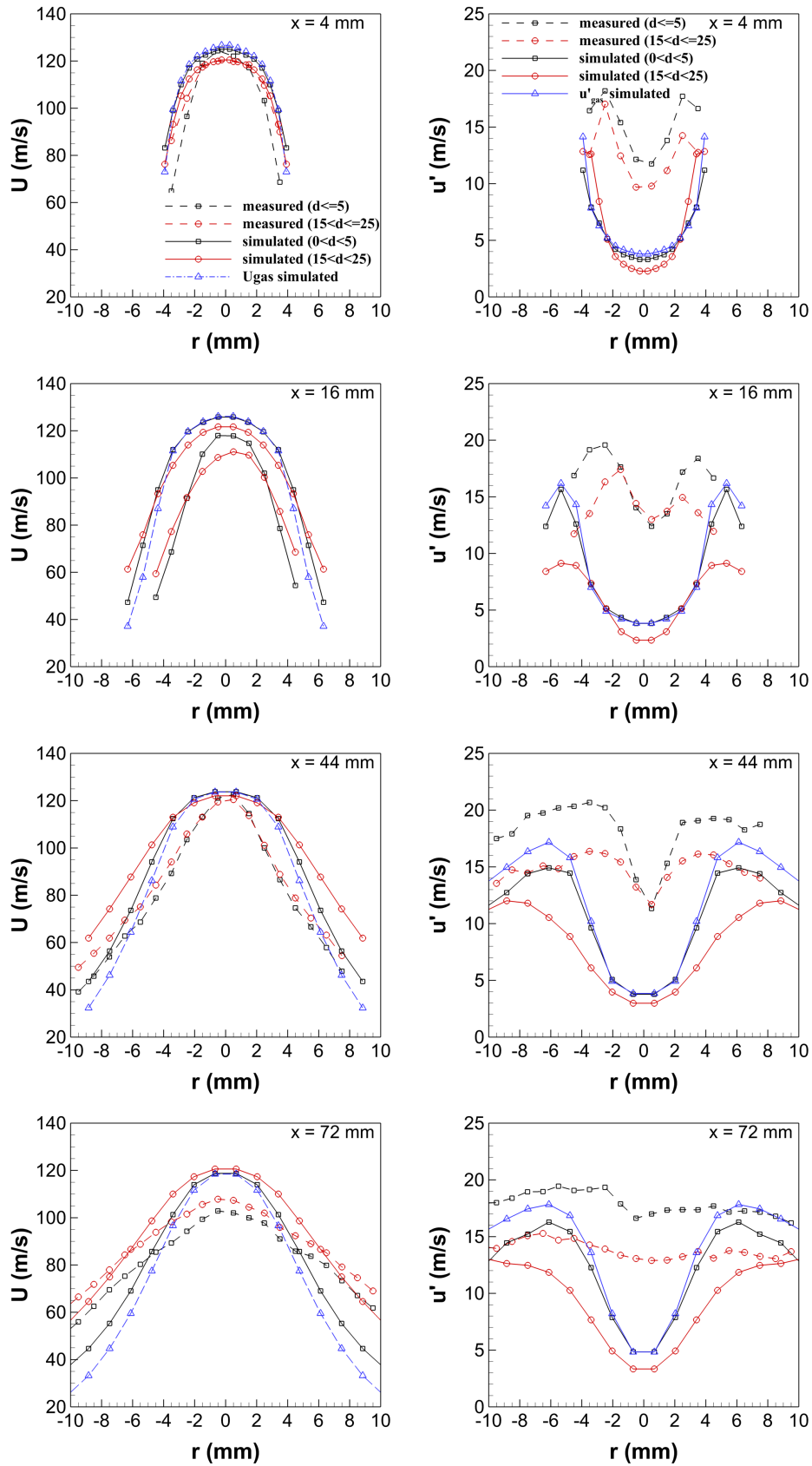
Figure 3.5: Comparison of calculated and measured radial profiles of mean and rms axial velocity at different axial locations

3.2.3. RADIAL MEAN AND RMS VELOCITY PROFILES

Fig. 3.6 shows the comparison of the calculated and the measured radial profiles of the radial mean and RMS values at different downstream distances. The calculated mean radial velocity profiles for all axial locations show that the spray is symmetric as observed by experiments. This can also be seen from the particle trajectory plot Fig. 3.13. For all axial locations the magnitude of the calculated mean radial particle velocity increases gradually when moving radially outwards and a good agreement is obtained between the calculated and the experimental findings. Also, the calculated particle mean radial velocity supersedes the mean radial velocity of the gas phase for r> 2 mm due to the higher inertia of the particles. Furthermore, the calculated radial gas phase velocity is in agreement with the small particle measured radial velocity which approximately represent the gas phase velocity until x = 16 mm. But as one moves downstream the calculated radial gas phase velocity starts to deviate (outside of the jet core) and is under predicted. This shows that the transport of momentum in the cross stream direction is being under predicted by the turbulence model which also manifests in the slow spreading of the jet witnessed the mean and RMS axial velocity profiles in Fig. 3.5. With regards to radial fluctuation velocity, the calculated gas phase v' is higher than the v' of large diameter particles and v' decreases with increasing particle diameter as confirmed by the experiments. Although the trend in the calculated RMS velocity profiles of gas and droplets are in good agreement with their measured counterparts the prediction of the magnitude of the fluctuations is again under predicted. As said above this may be due to inaccurate prediction of turbulent kinetic energy, combustion model and may be also due to the absence of turbulent two way coupling.
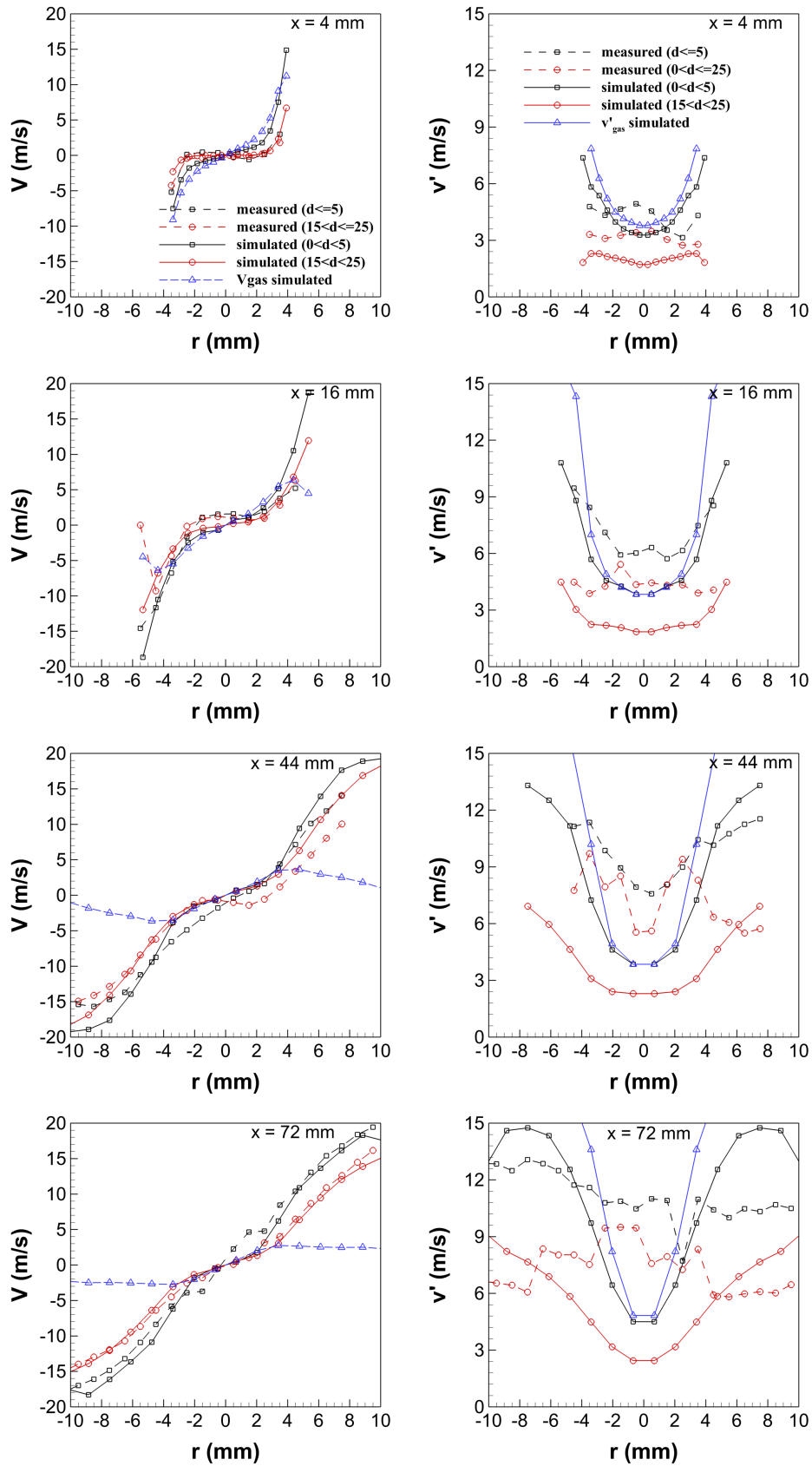
Figure 3.6: Comparison of calculated and measured radial profiles of mean and RMS radial velocities at different axial locations

3.2.4. Profiles of characteristic diameters

The calculated and measured radial profiles of the characteristic spray diameters at different axial locations are presented in Fig. 3.7 As mentioned earlier, a SMD of 19.5 μm was employed at the injection nozzle (x = -139 mm) during cold simulation (without combustion). For the hot simulation (with combustion) a single size distribution for the particles starting from all radial locations in plane x = 0 was obtained from the cold simulation there, as the radial profiles of the characteristic diameters obtained from the measurements at x = 4 mm were nearly constant. That is why at x = 4 mm the calculated characteristic diameters in Fig. 3.7 are still nearly constant across the jet. The plots in Fig. 3.7 show that the radial profiles of the characteristic diameters capture well the shape of the measured profiles. Also the width (defined as the ratio of $SMD/D10$) of the measured size distribution is in agreement with the calculated width. The calculated characteristic diameters rise with increasing axial distance, whereas the measured characteristic diameters remain almost constant with axial distance. Although the evaporation of an individual droplet in a spray always decreases its diameter, the evaporation of a spray can lead to a temporary increase, decrease or maintain nearly constant characteristic diameters of the spray. This behavior of the characteristic diameters in the course of the evaporation is not an indicator for a slow or fast evaporation. Evaporation on one hand leads to a removal of small droplets from the spray (this tends to raise the characteristic diameters, e.g. the SMD) but on the other hand to a reduction of larger droplets to medium size droplets (this tends to decrease the characteristic diameters). So there is a dynamic filling and depleting of the bins of the size distribution of an evaporating spray. The actual change of the characteristic diameters due to evaporation depends on the initial shape of the size distribution and the gasfield experienced by the individual particles of the spray. Only in a very late state of the evaporation of a spray the characteristic diameters converge, then collapse into 1 line and end up at a value of zero. This can be clearly seen in Fig. 3.8. It shows the evolution of different characteristic diameters including some volume undersize diameters ($D_v0.1, D_v0.5, D_v0.9$) along the axial distance for the hot simulation. In each axial registration plane, the characteristic diameters were calculated from all particles that passed the plane. It can be observed from Fig. 3.8, that the characteristic diameters increase until around x = 120 mm (this rise was already mentioned in the radial profiles of Fig. 3.7) even though strong evaporation is present (Fig. 3.4) and this increase is due to the above mentioned reasoning. Beyond x = 120 mm, where only a tiny fraction of the initial liquid spray volume is still present, all characteristic diameters fall continuously and converge. All characteristic diameters meet at a single value, namely the diameter of the very last particle at the moment, where the penultimate particle (in this case of 2 million of started computational particles) is just evaporated. This happened just before the outlet. Hence the course shown in Fig. 3.12 demonstrates complete evaporation in accordance with Fig. 3.4. The fact, that the measured characteristic diameters in Fig. 3.7 remained roughly constant in measured planes x = 4 to 72 mm, whereas the computed values rose there, is simply the result of a somewhat different initial size distribution at x = 0 interacting with a different gasfields, especially the gas temperature field. Once again, the combustion model is of strong influence. (It should be mentioned here, that in the simulation without combustion the axial development of the SMD was nearly constant from the injection nozzle to the exit of mixing pipe even though strong evaporation was already present there, see Fig. 3.4).

3.2.5. Volume flux profile

Figure 3.9 shows radial profiles of the calculated liquid volume flux distribution at different axial locations in the combustion chamber. At the beginning of the mixing pipe (x = 92 mm, not shown in the figure) the radial profile of the liquid volume flux of the droplets has a maximum at the pipe center and an additional bump at r = 1.4 mm. In the course of the further downstream development of that profile in the pipe, both
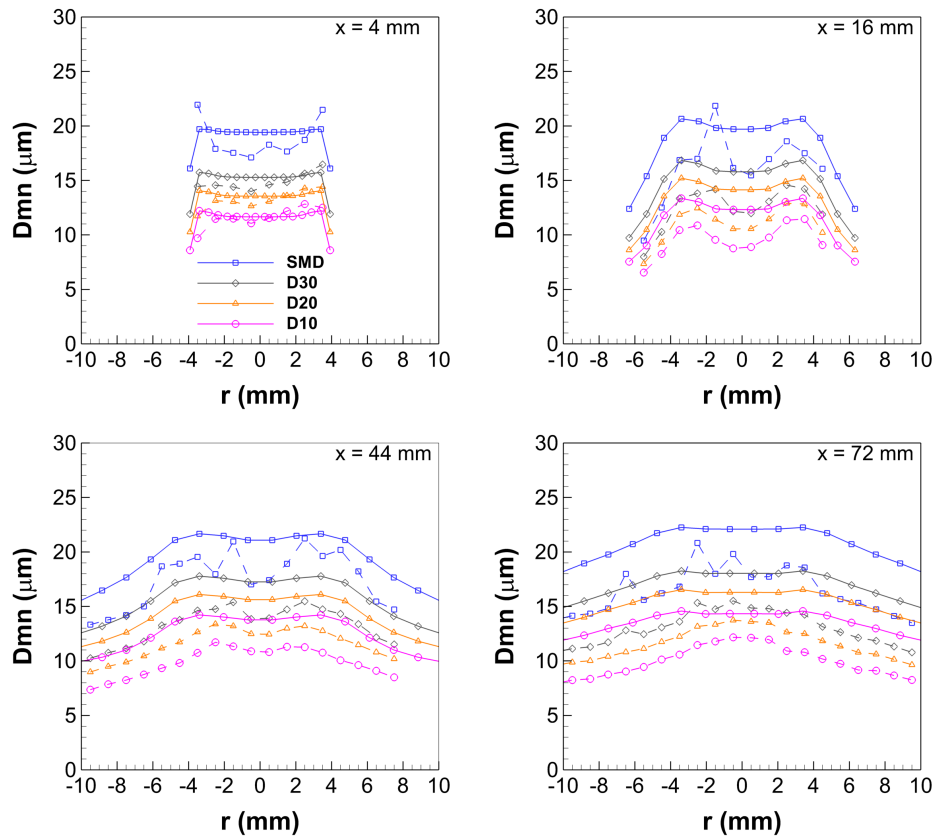
Figure 3.7: Comparison of calculated (solid lines) and measured (dashed lines) radial profiles of droplet diameters at different axial locations
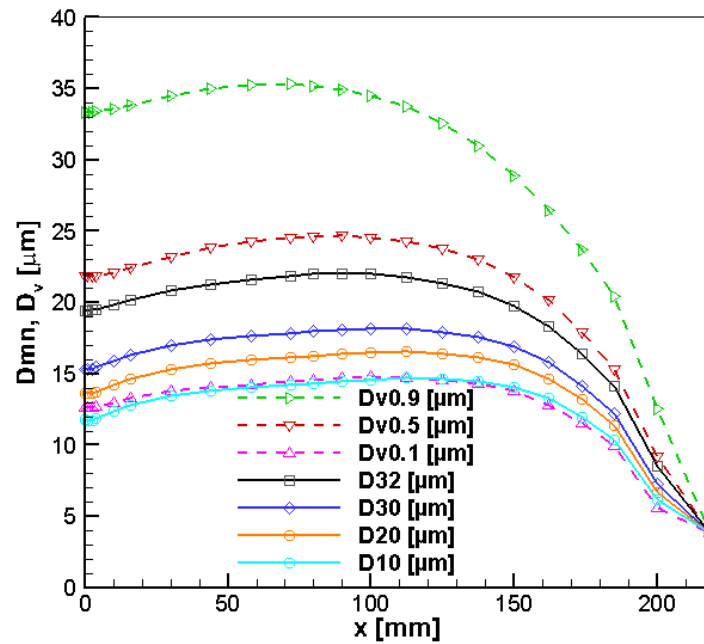

Figure 3.8: Axial development of characteristic diameters

maxima become lower and the bump moves toward the pipe wall. Fig. 3.9 shows, that finally at the exit of the mixing pipe (x = 0) most of the spray has concentrated near the pipe wall (r = 3.5 mm). The underlying radial movement of particles in the pipe from the region of high axial velocity to low axial velocity is an effect of the turbulent particle dispersion in the shear flow of the pipe. As that radial particle drift is limited by the pipe wall, the particles accumulate there. Downstream ($x > 0$) of the pipe exit the bounding pipe walls are no longer present, and the droplets spread radially into the chamber. So the accumulated maximum of the liquid volume flux profile near the radius of the pipe wall reduces (x = 10 mm) and finally disappears at x = 72 mm. This spreading of the particles is larger than the spreading of the gas jet (cf. the axial velocity of the large particles compared to the gas in Fig. 3.5 at x = 72 mm) according to the particle inertia (particle's Stokes number). It should be noted here, that volume flux profiles from the PDI measurements in the combustion chamber exist. However they are not calibrated and cannot be used for any quantitative comparisons. Nevertheless they confirm the presence of accumulated liquid volume near the wall of the pipe.
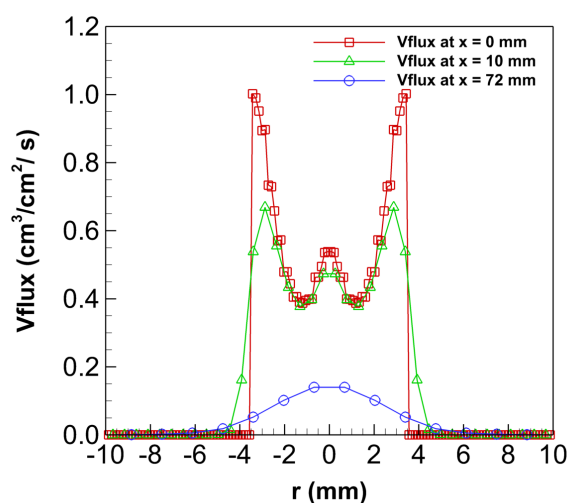

Figure 3.9: Calculated radial profile of liquid volume flux at three different axial locations

3.2.6. Temperature and species mass fraction evolution

Fig. 3.10 shows the temperature and species mass fraction evolution in the combustion chamber. It should be mentioned here that no temperature and species mass fraction were measured during experiments. Therefore in order to validate the simulations, comparison was made with the values obtained from a chemical equilibrium software Gaseq at similar operating conditions. The temperature rise happens quite early and can already be seen at x = 4 mm. This rise in temperature is also a factor in increasing the maximum axial jet velocity as the radial expansion of the jet is slower when compared to the measurements. It is also evident in the mean axial velocity profile in Fig. 3.5 where the maximum centerline velocity of the jet is slightly higher than the measured value. The temperature and species mass fraction profiles are obtained along the centerline where it is believed to have maximum temperature. The calculated values are in close agreement with the values obtained from the chemical equilibrium solver Gaseq. As the nozzle axis is not the axis of the combustion chamber itself, the flow starts to bend towards the outlet far downstream and this is the reason why a decreasing tendency is observed for both temperature and species mass fraction in the figure at downstream distances.
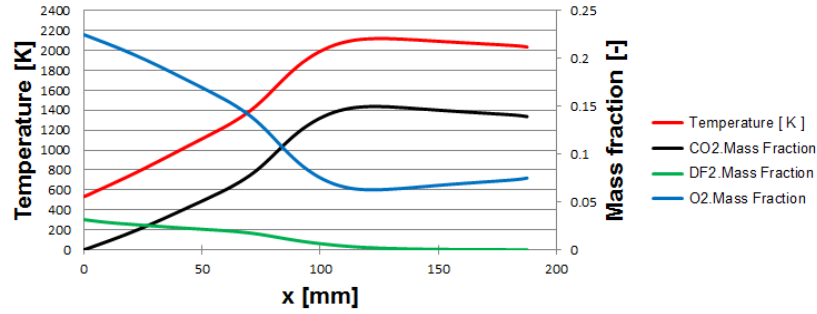
Figure 3.10: Evolution of calculated gas temperature and species mass fractions along the centerline of nozzle. Light heating oil is referred to as DF2 ($C_{14.32}H_{25.75}$)

3.2.7. TEMPERATURE FIELD, STREAMLINES AND SPRAY TRAJECTORIES

Figure 3.11 shows the calculated temperature field in selected planes in the combustion chamber. The xz-plane shows the gas jet. In the near field of the nozzle, the reaction zone is around the gas jet, whereas the jet core still remains relatively cold. As a consequence, the shown radial temperature profile does not uniquely define the flame lift-off height. The yz- plane close to the nozzle shows a distinct blue zone which is caused by the feeding of impingement cooling air through the axial slot into the combustion chamber. In the outlet cross section it is observed that the temperature is not fully uniform throughout the area: the maximum temperature at the outlet plane (x = 218.5 mm) is found to be 2084 K close to the geometric axis of the combustion chamber and minimmum temperature of 2025 K away from the geometric axis of combustion chamber. The CO_2 distribution in the outlet when normalized by its max. and min. values (0.1461 and 0.1390, resp.) exhibits nearly the same pattern as the normalized temperature distribution, so the CO_2 mass fraction in the outlet is higher, where the temperature is higher. These maximum and minimum CO_2 mass fractions are in close agreement with the equilibrium value of 0.1439 predicted by Gaseq for the combustion of the light heating oil with λ_G of 1.45. Further, the ratio of the computed mass flow of CO_2 through the outlet to the theoretical mass flow of CO_2 produced for complete combustion of the fuel is 0.99938. This indicates that the 1-step reaction is fully completed inside the combustion chamber.
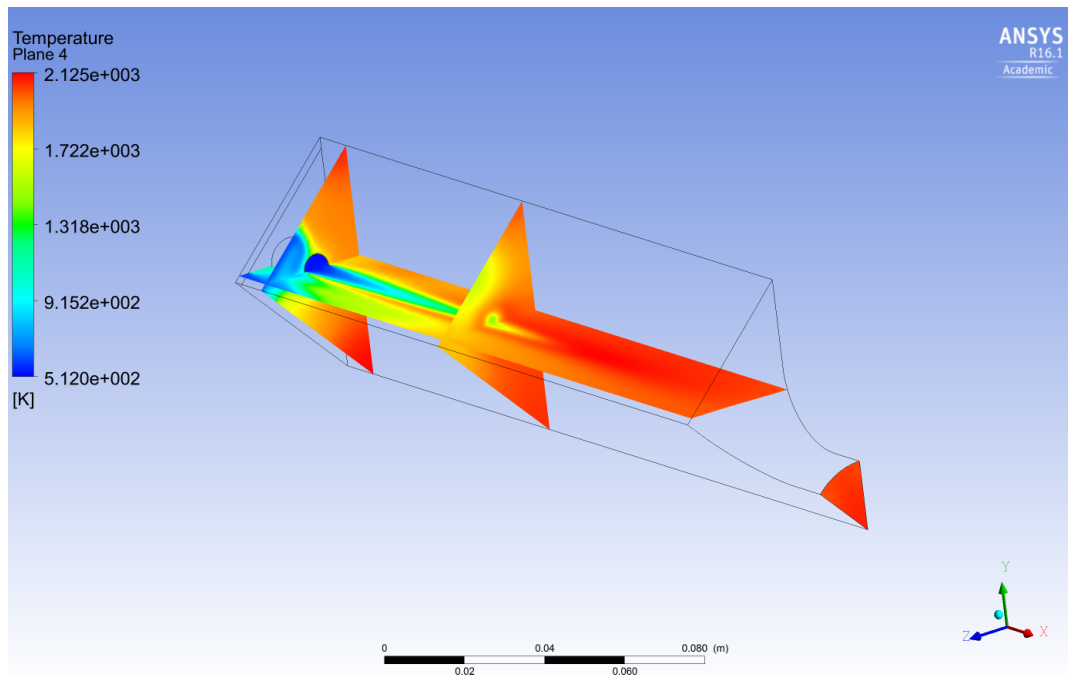
Figure 3.11: Calculated Temperature contour on selected planes in the combustion chamber

Figure 3.12 shows some streamlines in the combustion chamber. Existence of three distinct recirculation zones is visible. The two recirculation zones are present above and below the nozzle axis and help in stabilization of the flame. The third recirculation zone is located at the exhaust wall of the combustion chamber. It is rather weak and due to the flow bending from the nozzle axis to the outlet. Also visible are streamlines which emanate from the axial slot tangentially into the combustion chamber which are later entrained into the recirculating flow. Figure 3.13 shows particle trajectories computed by SPRAYSIM. 500 trajectories are

Figure 3.12: Calculated streamlines in the combustion chamber

shown in the figure. They reveal that the spray jet is actually symmetric in the measured axial range ($x < 72$ mm). The effect of the turbulent dispersion model is clearly visible. Finally, none of the spray particles reach the outlet indicating that complete evaporation of the spray occurs.

Figure 3.13: Calculated particle trajectories by SPRAYSIM in the combustion chamber

3.3. General Conclusion

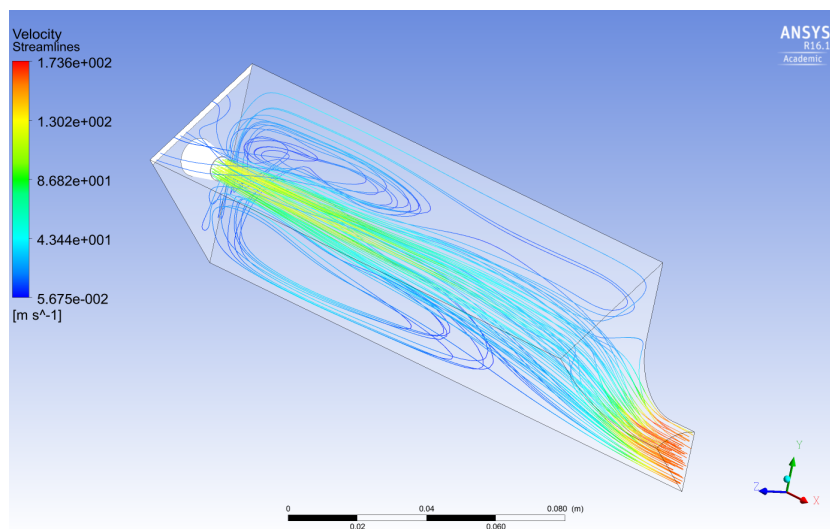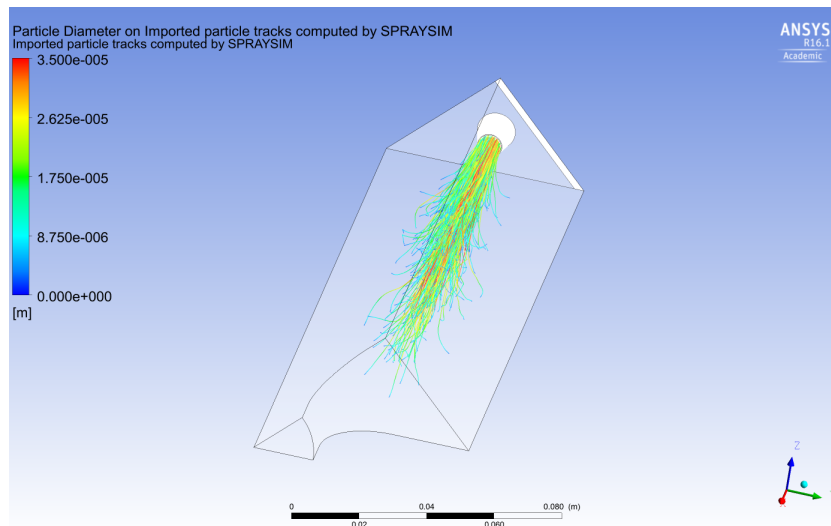The calculated and measured spray behavior in the combustion chamber showed fairly good agreement. The results from the simulations showed that a large portion of the evaporation happened already in the nozzle, although future investigation will be required to quantify the influence of the secondary breakup on the evaporation in the nozzle. Even though intense evaporation is predicted in the combustion chamber where the spray was fully evaporated, spray particles still penetrate deep into the combustion chamber (x > 150 mm).

Some differences were observed in the droplet axial and radial velocity profiles between simulation and measurements due to the low turbulence intensity prediction and slow spreading of the gas jet in the combustion chamber computed by the SST two-equation turbulence model. Also, the simulation showed that the spray characteristics was mainly affected due to the simple global 1-step chemical kinetics with simple turbulence-chemistry interaction (TCI) model EDM/FRC, which predicted a too early onset of the heat release.

The use of a detailed finite rate chemistry model and turbulence-chemistry interaction model is a must for a quantitatively good prediction (not post-diction) of the two-phase flow in the combustion chamber. The aforementioned shortcomings of the present case will be addressed in the next chapter where a better turbulence model and a better TCI model (Eddy Dissipation Concept) with reduced chemical mechanism will be used.

4

NUMERICAL SIMULATIONS OF THE DLR MGT BURNER WITH ANSYS FLUENT

In this section, the CFD simulations of the MGT burner in FLUENT is discussed. As the simulation result in the previous section showed some inaccuracies in predicting the velocity profiles due to the turbulence and combustion models used, it was decided to use the FLUENT code which provides access to different turbulence and turbulence-chemistry interaction models with provision to include detailed reaction mechanism which is essential to model finite rate chemistry effects. Furthermore, the results obtained from these simulations are discussed and also appropriate comparisons are made with the previous simulation to highlight the causes for the inaccuracies.

During all the simulations carried out in FLUENT, Eulerian-Lagrangian approach is used to simulate the turbulent spray combustion. In this case, the Lagrangian particle tracking from SPRAYSIM was not employed as the coupling of SPRAYSIM with FLUENT code (although done in the past [64]) is currently not possible. Therefore, Lagrangian tracking was done in FLUENT itself along with the gas field computation. Nevertheless, the spray boundary conditions which are required for simulations are still provided by SPRAYSIM which can generate an initial condition file in the format which is acceptable for FLUENT runs. Further, in order to facilitate meaningful comparison with the previous results obtained from CFX, the liquid properties of the diesel fuel which was used in CFX was also used in FLUENT through the User-Defined Functions (UDF) for the liquid properties such as: liquid density, liquid isobaric specific heat capacity, latent heat of vaporization and vapor pressure. Meanwhile, for the gas phase the detailed reaction mechanism of Chang et al. [65] was used for n-decane. The reaction mechanism consists of 40 species and 141 reactions and has been validated against the experimental data available on n-decane oxidation and also been applied to predict the combustion and emissions from premixed charge compression ignition (PCCI) engine by CFD simulations. This work also serves as another validation of the reaction mechanism.

In order to predict the turbulent spray combustion phenomena correctly, firstly Reynolds Stress Model is used along with SST model to compare the simulation result against the CFX simulation employing the SST turbulence model. Also, $k - \epsilon$ model is used, to take into account- turbulence two-way coupling and to analyze the sensitivity of this in the current case. Secondly, the turbulence-chemistry interaction (TCI) is modeled through the Eddy Dissipation Concept with detailed reaction mechanism mentioned above. Also, in this present investigation the applicability of nonpremixed Steady Flamelet Model (SFM) and Flamelet

Generated Manifold (FGM) of FLUENT with gaseous flamelet model implemented therein is investigated. The results obtained from different modeling approaches are compared with the experimental data.

The computational grid used for simulations in FLUENT is a similar grid with similar number of nodes as used in chapter 3 but a change was made in the number of volume domains. Instead of having one volume domain for the entire combustion chamber two volume domains are used: one from the inlet of air until the exit of mixing pipe (x = -139 mm to 0 mm) and other from start of combustion chamber till outlet (x = 0 mm to x = 218.5 mm). The EDC combustion model requires high temperature to start the combustion process. If the entire combustion chamber consists of only 1 volume domain, then the high temperature patch which is applied for the volume domain will be applied for the whole combustion chamber. When this happens combustion is predicted where there is fuel source available (in this case upstream of combustion chamber). This is not seen in the measurements. So, when there are two volume domains available, high temperature patch can only be applied to the domain where combustion is seen in the measurements (in this case from exit of mixing of pipe to the outlet of the combustion chamber). By doing so even when there is fuel source available (due to evaporation) upstream of combustion chamber, there is no high temperature patch applied and the flow will remain cold. When the fuel-air mixture enters the combustion chamber, combustion process starts. In short, EDC model was applied to both subdomains and only the second subdomain (combustion chamber) was initialized with high temperature patch. It should also be mentioned here that, even with employing two volume domains for the combined ED/FR with 1-step global reaction scheme (eqn.2.28) flashback was observed due to simple reaction kinetic and highly turbulent field present upstream of the mixing pipe.

The boundary conditions for the gas field is the same as given in Table 3.1 and as far as droplets boundary condition is concerned, the droplet size of 19.5 μm was used with rootnormal size distribution and the droplet nominal axial velocity was obtained from the mass flow rate through the nozzle as also mentioned in section 3.1. The results are presented mainly in following sections: study of above mentioned turbulence models in conjunction with Eddy Dissipation Concept model (EDC), then the applicability of flamelet methods and lastly the effect of radiation on combustion characteristics and then effect of higher air preheat air temperature on the combustion characteristics in this type of burner.

4.1. RESULTS FROM EDC MODEL

4.1.1. AXIAL VELOCITY PROFILES

Firstly the axial and radial velocity profiles of the droplets are studied as these profiles were inaccurately predicted in the previous simulation described in chapter 3. Fig.4.1 shows the comparison of the radial profiles of the measured and the calculated mean axial velocity at different axial locations with Reynolds Stress Model and SST model. The figure also shows the result obtained from the CFX simulation employing SST turbulence model with ED/FR model with 1 step chemistry to facilitate the comparison of the current simulation with the previous simulation. To maintain better readability of the figure, the profiles of mean axial velocity are presented separately for two different droplet classes ($0 < d \leq 5$, $15 < d \leq 25 \mu m$). Fig. 4.1 clearly shows that both the turbulence models predict almost similar velocity profiles for both the droplet classes at all the axial locations and are in good agreement with the measured mean axial velocity profiles there.

At x = 72 mm, it is interesting to observe that the mean axial velocity profile predicted by the SST turbulence with EDC model is different than the SST turbulence with ED/FR model with 1 step chemistry meaning that rather than the turbulence model, it is the spatial heat release model which affects the velocity prediction in this case. In these kind of FLOX combustors [12], the heat release is delayed by the reason of nonequilibrium effects in chemistry due to the mixing at high flow velocities in the vicinity of the nozzle exit. Whereas the ED/FR model (used in the previous chapter with CFX-SPRAYSIM simulation of only the

combustion chamber) with only 1 step chemistry predicts relatively faster heat release compared to the EDC model with multi-step chemistry which can be seen in the temperature evolution along the nozzle centerline plotted in Fig. 4.3. This faster heat release along the centerline accelerates the particles to have higher velocity along the centerline and respond slowly to the spreading of jet. It should also be mentioned here that the flow at $x \approx 190mm$ bends from the nozzle axis towards the combustor axis and that is why the temperature profile along the centerline starts to decrease from $x \approx 120mm$. However, the combustion reaches the adiabatic flame temperature and was verified against the values obtained from the equilibrium calculation program Gaseq [24] at the given global equivalence ratio.

The heat release in the combined ED/FR model is faster because the reaction rate is computed by taking the minimum of the two rates computed by ED and FR models. The fuel-air mixture is well mixed before entering the combustion chamber. When the fuel-air mixture enters the combustion chamber the reaction rate computed from FR (Arrhenius Law) with 1 step chemistry is high compared to the ED model. So when the reaction rate is computed from the ED model alone, it ignores the chemical non-equilibrium effects and predicts the rate according to $rate \propto \epsilon/k$ resulting in higher temperature gradients. While, with EDC model and multi-step chemistry, the temperature gradient is somewhat smooth when compared to the combined ED/FR model as all the intermediate reactions are taken into account and is more closer to the reality.

Figure 4.2 shows the comparison of the calculated and measured radial profiles of the axial rms velocity for two droplet classes at different axial locations. At x = 4 mm, the fluctuations are minimum close to the centerline and rises as one moves away from the centerline of the jet towards the walls. This maxima is because, the maximum turbulence production happens in the shear layers of the gas jet (pipe inner radius is 3.5 mm) when it enters the combustion chamber and there is less turbulence production near the centerline as the mean velocity gradient is less. While the numerical model (both RSM and SST models) are able to capture this trend, an under-prediction of the fluctuations is seen near the centerline. This may be due to two reasons: firstly, it might be due to the under-prediction of the turbulent fluctuations in the upstream mixing pipe as the y^+, which is the non-dimensional distance of the first cell node to the wall is close to 50 in the pipe region (for both turbulence models). This means the buffer layer and the viscous sub-layer are not resolved. As most of the turbulence is generated in this region, failing to resolve this leads to smaller turbulence level (turbulence kinetic energy) production and advection of it downstream. Having said that, for ϵ based equations such as $k-\epsilon$ and Reynolds Stress Model a value of $y^+ = 50$ is normal with the standard wall function to account for the law of the wall. Secondly, in a jet, vigorous eddy mixing transports the turbulent fluid from nearby region of high turbulence production towards and across the centerline [66]. As such the values of $\overline{u'^2}$, $\overline{v'^2}$ and $\overline{w'^2}$ do not decrease very much. This effect may not be correctly predicted by the turbulence models. Also, at x = 72 mm the measurements show a flat fluctuation profile whereas the calculations still show a small dip near the centerline of the nozzle, which means that the jet core is still present at x = 72 mm and this flattens only later (x = 90 mm, not shown here).

(a) For droplet class $0 < d \leq 5\mu m$ (b) For droplet class $15 < d \leq 25\mu m$

Figure 4.1: Comparison of calculated (solid lines) and Measured (dashed lines) radial profiles of mean axial velocity of droplets of size class: $a. \, 0 < d \leq 15\mu m$, $b. \, 15 < d \leq 25\mu m$ at different axial locations

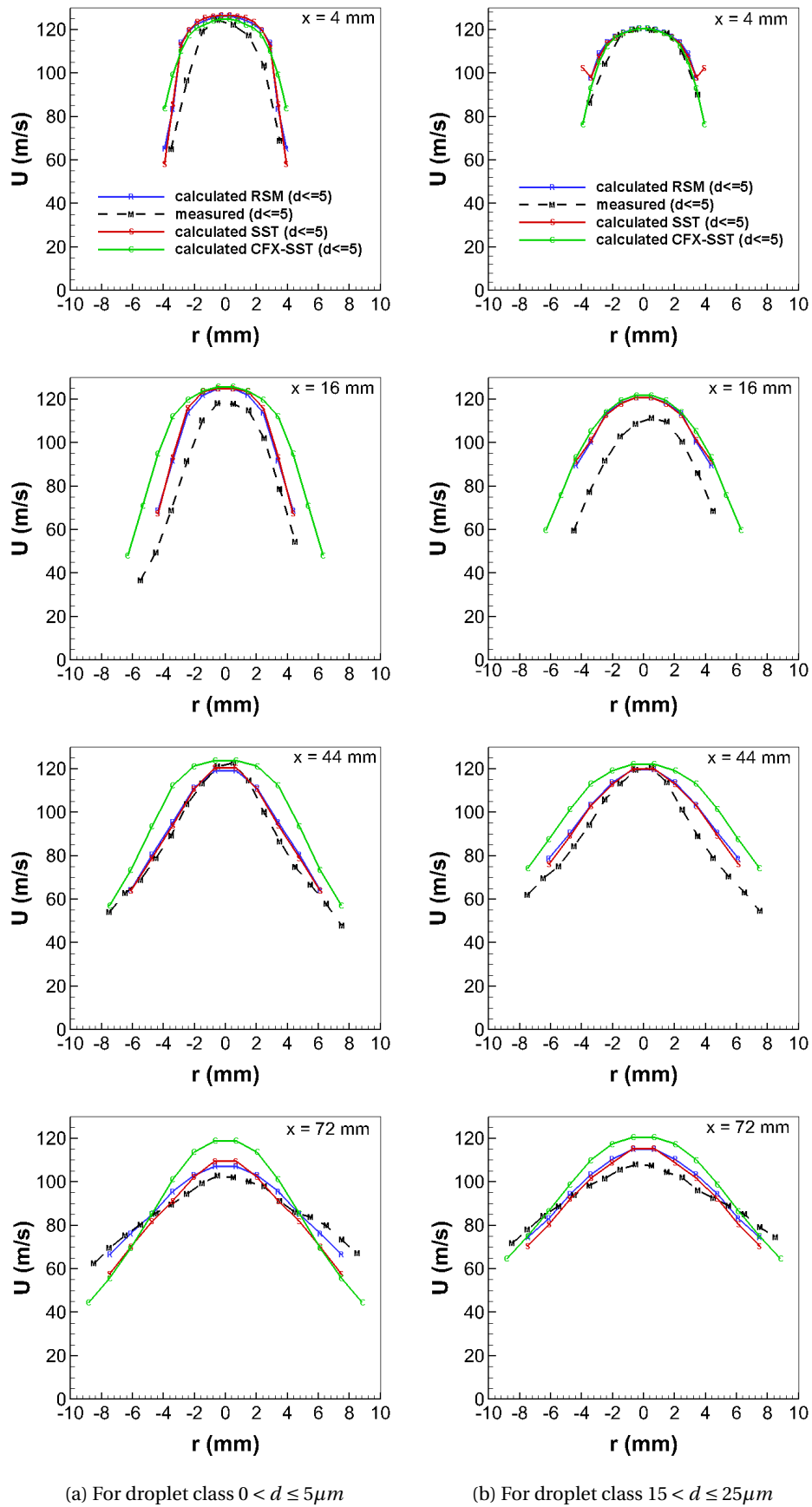(a) For droplet class $0 < d \leq 5\mu m$ (b) For droplet class $15 < d \leq 25\mu m$
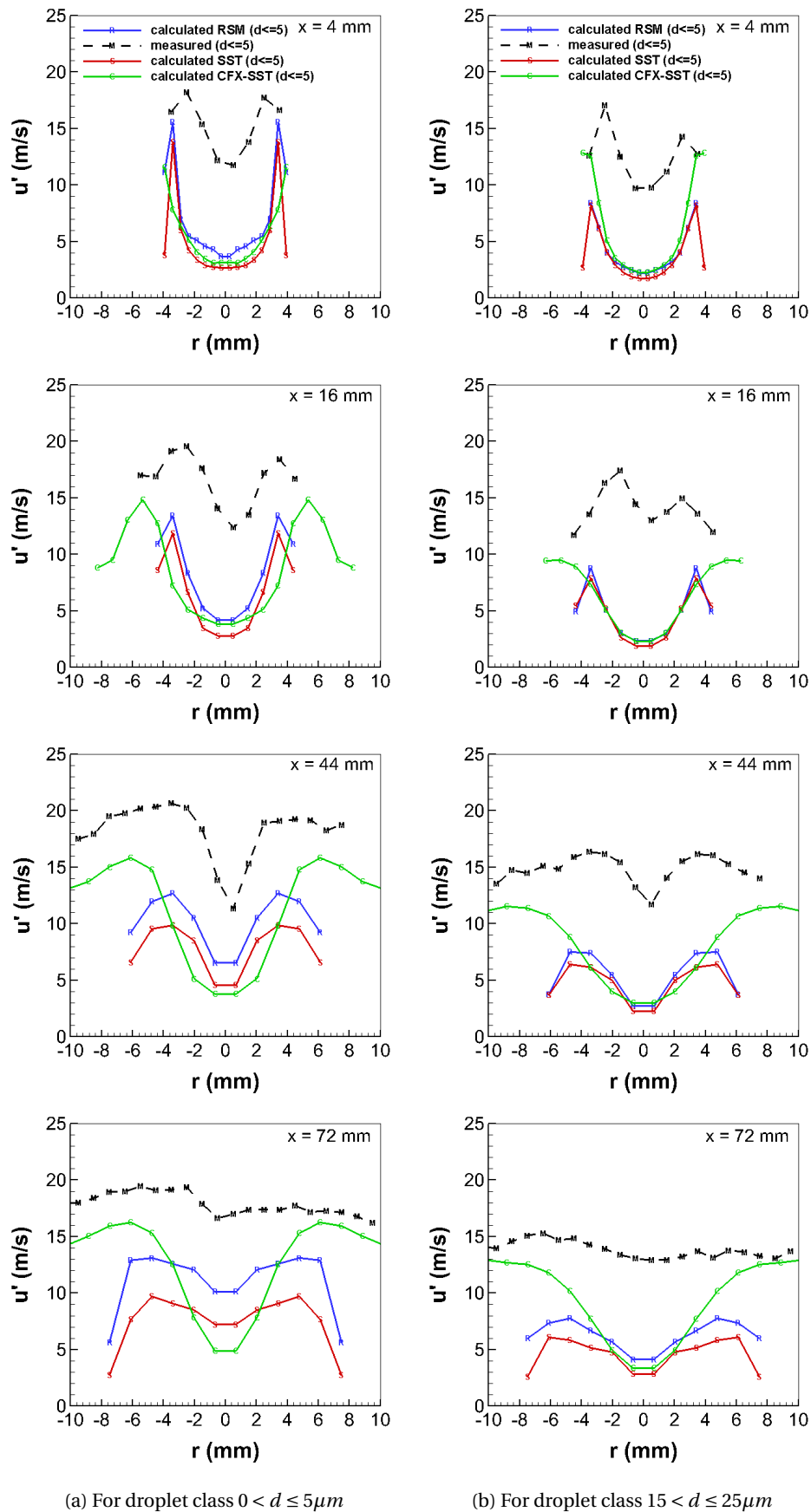
Figure 4.2: Comparison of calculated (solid lines) and measured (dashed lines) radial profiles of the rms axial velocity of droplets of size class: a. $0 < d \leq 15\mu m$, b. $15 < d \leq 25\mu m$ at different axial locations
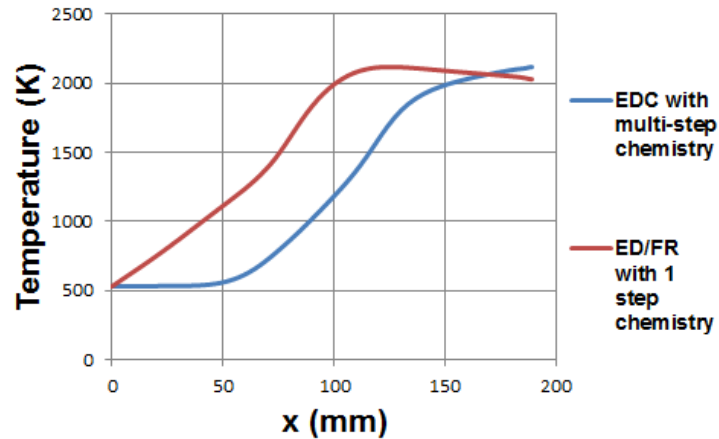
Figure 4.3: Calculated temperature evolution along centerline of nozzle #6 for EDC model used in ANSYS FLUENT and with the ED/FR model used in CFX 3

4.1.2. RADIAL VELOCITY PROFILES

Fig.4.4 shows the comparison of the calculated and measured mean radial profiles of the radial velocity for two droplet classes at different axial locations. The calculated mean radial velocity profiles shows that the spray jet is quite symmetric around the nozzle axis. At the edge of the jet where the maximum liquid volume flux exists higher radial velocities are observed indicating the spread of the spray. At x = 4 mm, the calculated mean radial velocity for both droplet class is close to zero as predicted by both RSM and SST turbulence models for r > 4 mm. Whereas already non-zero velocity is seen there in the measurements which means that the spreading of the jet is slightly slower aided by slower heat release from the EDC model and the size of recirculation regions present above and below the centerline. However at x = 4 mm the combined ED/FR model of CFX which predicts early heat release leads to higher radial velocities compared to the measurements outside of the jet core (r > 3 mm). For x > 16 mm, the calculated mean radial velocity of the bigger droplets ($15 < d \le 25 \mu m$) from both models is slightly less outside r > 3 mm compared to the measurements due to the combined effect of particle inertia, heat release which slowly evaporates these droplets. Further at x = 72 mm the radial velocities increase because of the reducing dimension of the recirculation region.

Fig. 4.5 shows the comparison of the radial profiles of measured and calculated rms radial velocity at different axial locations with different turbulence models. As was with the axial fluctuations, the same reasoning holds for the anamoly of the calculated profiles from the measured profiles. The magnitude of the fluctuations computed from the SST model for r > 3 mm for both droplet classes with the combined ED/FR model in CFX suggests that turbulence production in shear layers is correctly predicted.
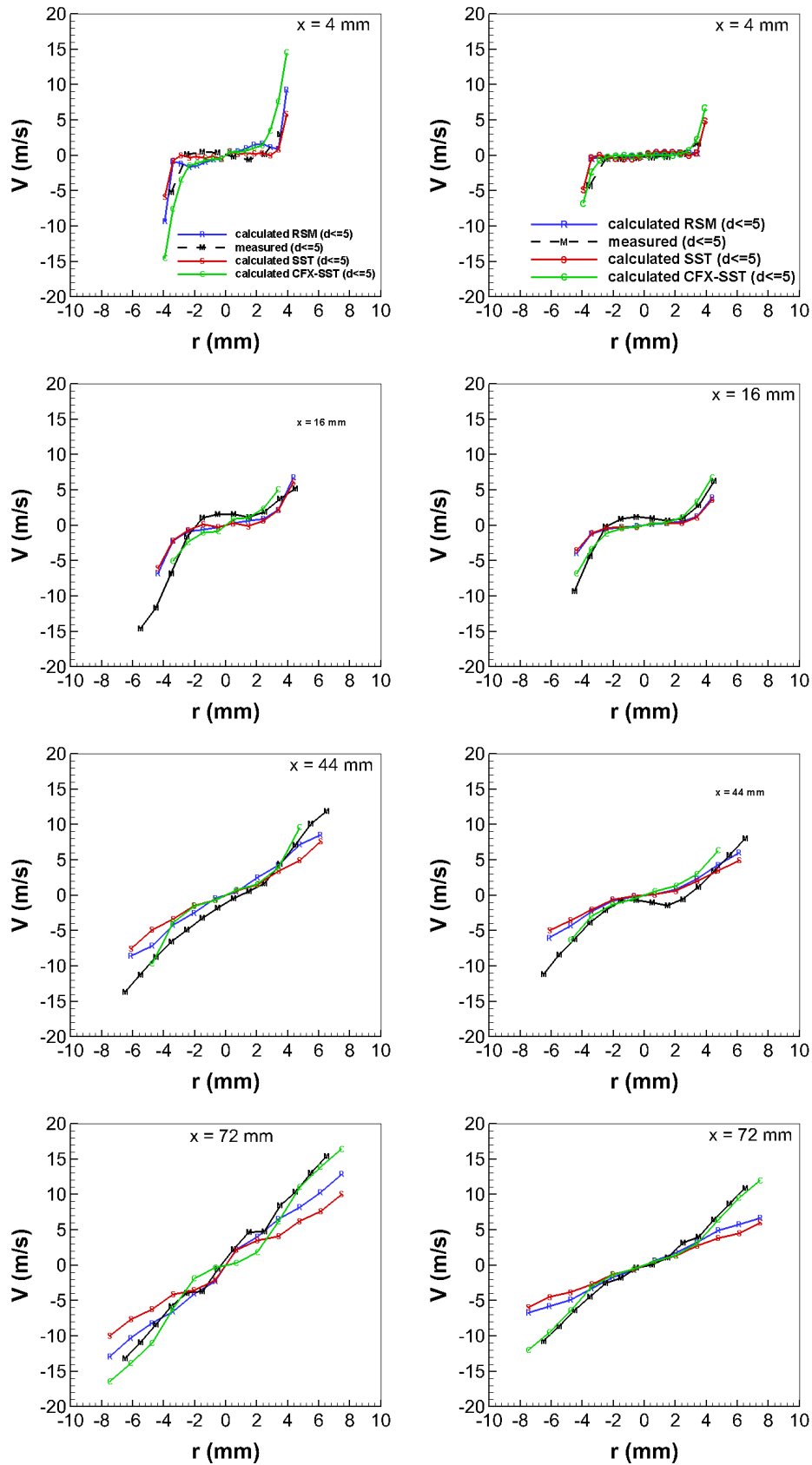
(a) For droplet class $0 < d \leq 5\mu m$ (b) For droplet class $15 < d \leq 25\mu m$

Figure 4.4: Comparison of calculated (solid lines) and measured (dashed lines) radial profiles of mean radial velocity of droplets of size class: a. $0 < d \leq 15\mu m$, b. $15 < d \leq 25\mu m$ at different axial locations

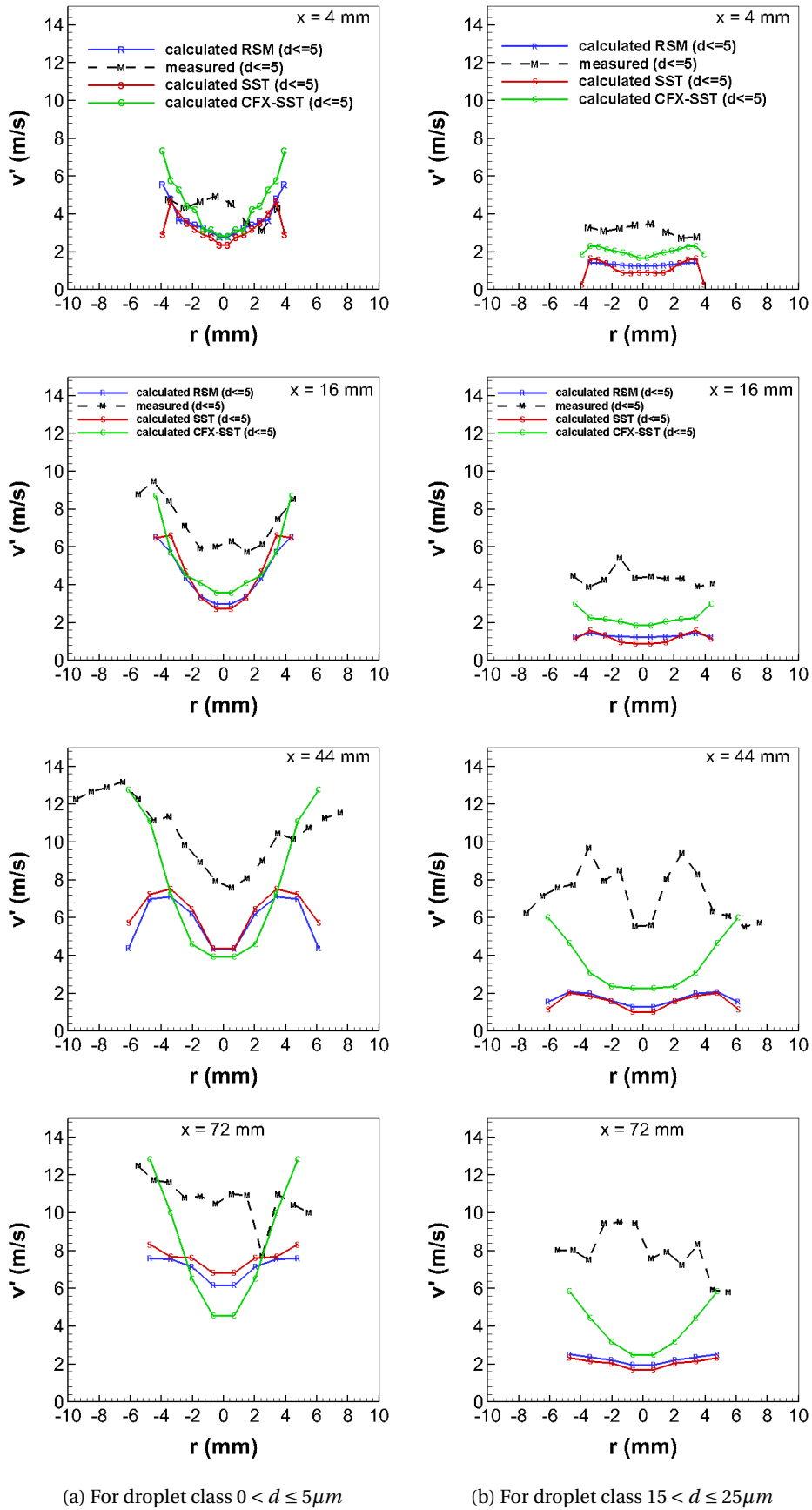(a) For droplet class $0 < d \leq 5\mu m$ (b) For droplet class $15 < d \leq 25\mu m$

Figure 4.5: Comparison of calculated (solid lines) and measured (dashed lines) radial profiles of rms radial velocity of droplets of size class: $a.\ 0 < d \leq 15\mu m$, $b.\ 15 < d \leq 25\mu m$ at different axial locations

4.1.3. LIQUID MASS FLOW PROFILE

As mentioned in the previous chapter, development of the liquid mass flow normalized by the initial liquid mass flow is one of the measure of evaporation progress and this is studied using the EDC model with different turbulence models. Fig. 4.6a shows the streamwise development of liquid mass flow normalized by injected mass flow for the simulation with EDC model with Reynolds Stress transport turbulence. Fig. 4.6b shows the comparison of the evaporation progress from the simulation with EDC combustion model and SST turbulence model with the combined ED/FR model and SST turbulence model with 1 step chemistry. Fig. 4.6a shows the similar characteristics which was observed in the previous simulation (Fig. 3.4) such as: fast evaporation in the mixing chamber until the mixing pipe due to the higher inlet air temperature of 573 K then followed by reduced evaporation in the mixing tube starting from $x \approx -96$ mm until x = 0 mm due to high gas velocity. At the exit of the mixing tube already $\approx 60\%$ is evaporated which was similarly predicted in the previous case. Nevertheless, the slope of the evaporation progress line in case of ED/FR model is slightly steeper when compared to the EDC model and this is due to the high heat release predicted by the ED/FR model which results in the faster evaporation of the droplets (see Fig. 4.3) against the slightly delayed evaporation in case of the EDC model which predicts delayed spatial heat release. Finally, both the models predict similar spray penetration length of ≈ 150mm with value of 0.0003 at x = 150 mm.

Further in the Fig. 4.6b a slightly higher evaporation rate is predicted in the mixing chamber (until the entry of mixing pipe) in case of simulation with EDC model in FLUENT when compared to the combined ED/FR model simulation in CFX. This may be due to the different gas film properties experienced around the liquid droplet in EDC model. In the EDC model a detailed reaction mechanism of n-decane ($C_{10}H_{22}$) is used whose thermodynamic properties are slightly different from the Light Heating Oil ($C_{14.32}H_{25.75}$) used in the combined ED/FR model in CFX. As the vaporization models are extremely sensitive to the physical properties of the variables involved [35] a direct comparison in this case does not exactly hold good. Nevertheless, the evaporation model employed in FLUENT is a classical model according to eqn.106 and eqn.109 of Sazhin [36] which take into effect the convective flow of vapor and gas mixture away from the droplet surface. While, in SPRAYSIM the Abramzon-Sirignano evaporation model is implemented and is used in the CFX-SPRAYSIM simulations in chapter 3. Sazhin [36] reports that when Abramzon-Sirignano model is used, the heat transfer number and Nusselt number are less compared to the classical theory which is employed in FLUENT. This reduction is due to the thickening of the film around the droplet which slightly reduces the heat and mass transfer rates away from the droplet. Thus this reduced Nusselt number in Abramzon-Sirignano model leads to slightly reduced evaporation rate in Fig. 4.6b.

4.1.4. VOLUME FLUX PROFILE

Fig.4.7 shows the calculated volume flux development at different axial locations with Reynolds Stress Model and Shear Stress Transport model for turbulence and Discrete Random Walk (DRW) model for turbulent particle dispersion. The volume flux profile obtained from the SST turbulence model and DRW turbulent dispersion model in FLUENT is similar to the profile obtained from the SST turbulence model and spectral dispersion model in CFX. From the figure it can be seen that, at the beginning of mixing pipe (x = -92 mm) as the flow exits the nozzle, the liquid volume flux has maximum at pipe center with a bump at r = 1.4 mm. Due to turbulent particle dispersion, the particles move from high velocity region at the center to low velocity region towards the pipe wall. This liquid volume accumulation moves the maximum of liquid volume flux from pipe center towards the wall and it remains until the liquid exits the pipe. Further downstream as the pipe walls are no longer present the accumulated maximum liquid volume flux near the walls of the pipe drops and disappears at x = 72 mm. However, as was mentioned in the previous section that there were no

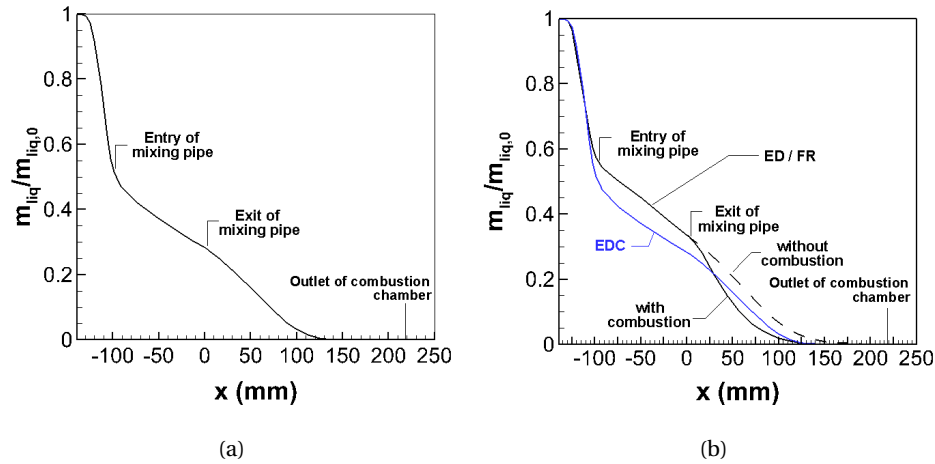(a)   (b)

Figure 4.6: a. Evaporation progress in EDC (RSM turbulence) with evaporation model in FLUENT, b. Comparison of combined ED/FR model (SST turbulence) with Abramzon-Sirignano model in SPRAYSIM and EDC model (SST turbulence) with evaporation model of FLUENT

calibrated volume flux measurements for quantitative comparison. Nevertheless the qualitative profiles are similar to the ones obtained in the calculation.

Furthermore, the volume flux profiles obtained from the Reynolds Stress model is different than the one computed by the SST model. More liquid accumulation is seen near the centerline when compared to the SST model. This is due to the particle dispersion model. The particle dispersion model in FLUENT computes the fluctuations based on the normal stresses in different directions in case of anisotropic turbulence. As seen earlier the particles accumulate at the center of the pipe at x = -92 mm where the turbulence intensity is relatively less. In case of RSM, v'^2 is smaller than u'^2 and thus the particles do not have enough vertical fluctuations to travel from high velocity to low velocity region. This liquid accumulation at the centerline then develops along the pipe until the liquid exits the pipe into the combustion chamber. However in case of SST turbulence model the particles accumulate towards the wall and this is due to the particle dispersion model where in the instantaneous gas fluctuation velocity in all directions is same and is equal to $\sqrt{2k/3}$ thus redistributing the droplets from centerline towards the pipe walls.
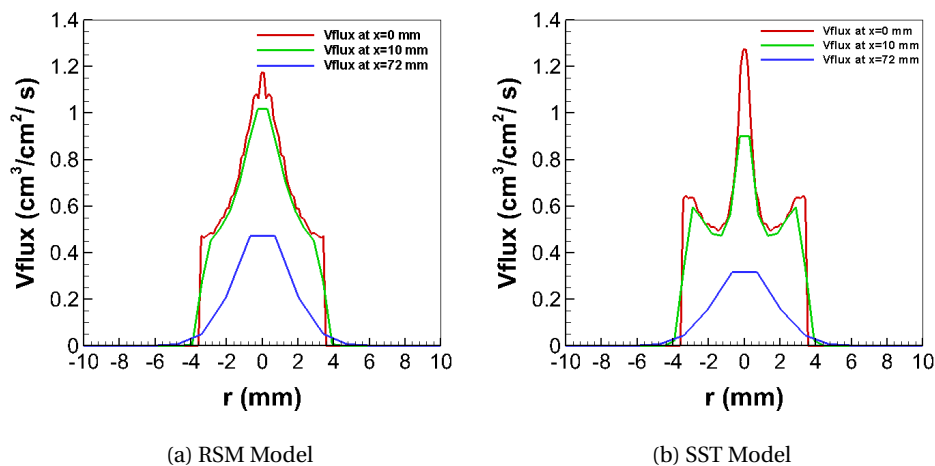

(a) RSM Model   (b) SST Model

Figure 4.7: Liquid volume flux profile at different axial locations using RSM and SST turbulence models

4.1.5. PROFILES OF CHARACTERISTIC DIAMETERS

Fig. 4.8 shows the comparison of the measured and calculated radial profiles of the characteristic diameters at different axial locations in the combustion chamber. The radial profiles are shown here only for the RSM turbulence model as the profile obtained from different turbulence model resulted in negligible difference. The radial profiles of the characteristic diameters follow the similar trend as was seen in the previous simulation in CFX in Fig. 3.7. Again, the radial profiles of the characteristic diameters capture the proper shape of the measured radial profiles and also the width of the size distribution (defined as: SMD/D10) fairly agrees with the measured width of the size distribution. The width of the size distribution is important as it is one of the factors in determining the heat release from combustion.
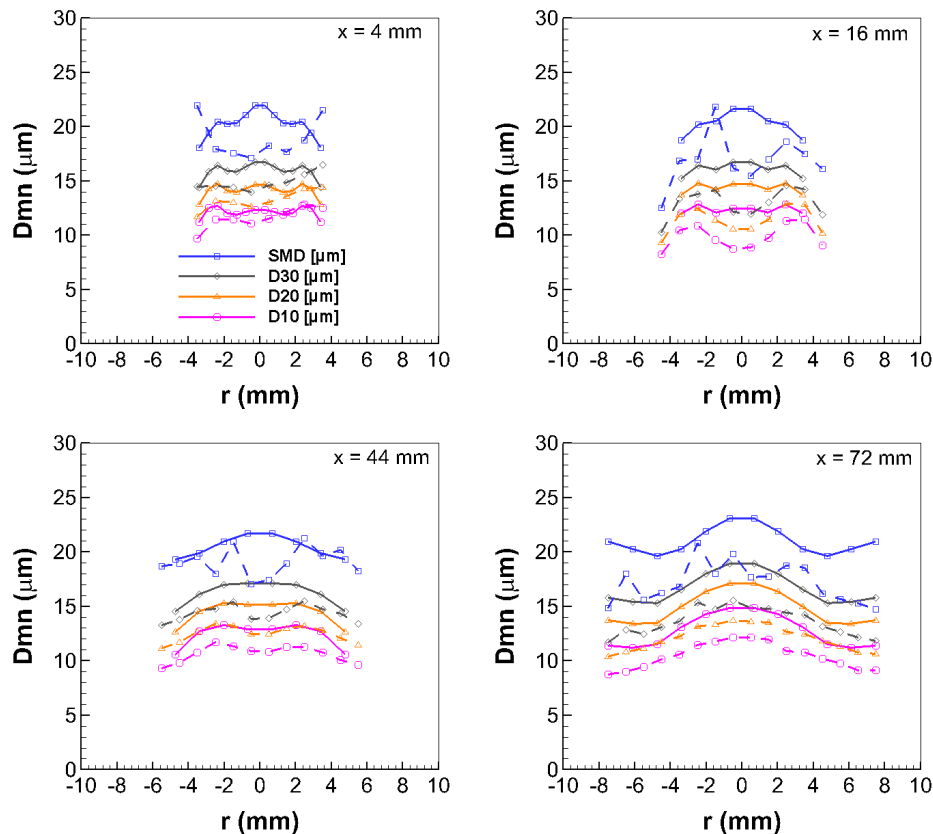

Figure 4.8: Comparison of calculated (solid lines) and measured (dashed lines) radial profiles of characteristic diameters at different axial locations

Furthermore, the value of the SMD from the injection (x = -139 mm) till x = 4 mm is nearly the same despite strong evaporation and this could be due to the depletion of small droplets and reduction of large droplets to small droplets are occurring at same rate. Further, the calculated characteristic diameters are increasing with increase in axial distance as seen in Fig. 4.8 and Fig. 4.9. The reason for this behavior is already explained in the section 3.2.4. In addition, in Fig. 4.9 initially there is increase in characteristic diameters after the injection and this is due to the evaporation of smaller droplets which increases the characteristic diameters. But at x = -106 mm there is a sudden decrease of diameters and this is because at x = -105 mm there is an axial slot through which the preheated inlet air (573 K) enters and this may aid the evaporation of small droplets and thus reduces the characteristic diameters. As there is only little liquid mass present beyond x = 120 mm all characteristic diameters fall continuously and converge to a value of the last droplet remaining before its evaporation.
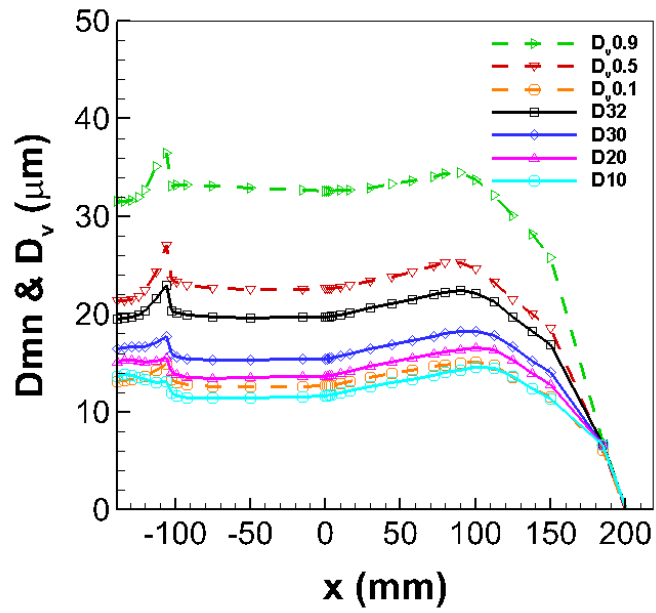
Figure 4.9: Axial evolution of calculated characteristic diameters

Finally, the calculated characteristic diameters are found to increase whereas the measured characteristic diameters are found to remain constant with increase in axial distance and this is due to the droplet size distribution experiencing somewhat different gas field compared to measurements as the calculated gas field is different due to the different turbulence field and particle dispersion resulting from the different turbulence field.

4.1.6. TEMPERATURE FIELD

Fig. 4.10 shows the calculated temperature field in selected planes in the combustion chamber. The gas jet and the impingement cooling air effect are observed in th yz and xz planes which were also observed in Fig. 3.11. Again, in the outlet the calculated temperature distribution is not fully uniform throughout the area and exhibits the similar distribution with higher temperature of 2112 K close to the geometric axis of the combustion chamber. While the local minimum temperature of 2075 K occurs away from the geometric axis of the combustion chamber. The computed CO_2 mass fraction distribution is also not fully uniform and the values range from minimum of 0.137 to 0.140. These values are very close to the value of 0.135 predicted by the equilibrium calculations by Gaseq [24] with n-decane fuel and global equivalence ratio of $\lambda_G = 1.45$. Also, the calculated NO mass fractions at the outlet are less than the equilibrium values validating the FLOX principle in producing low NO_X emissions.
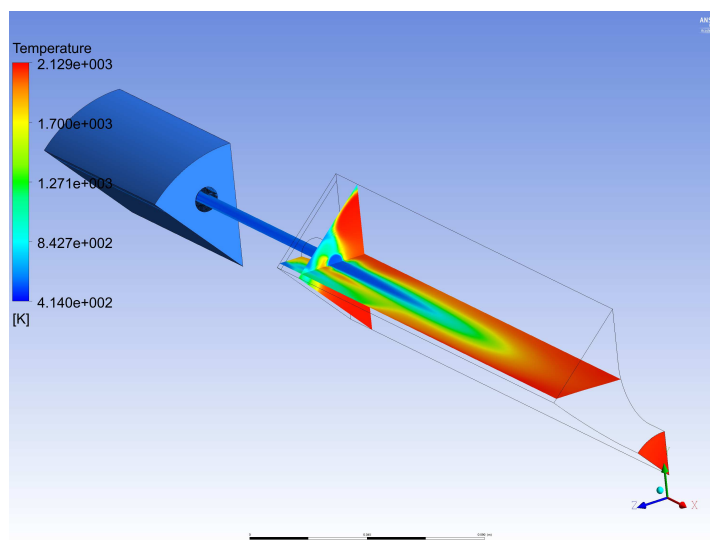

Figure 4.10: Calculated temperature field in selected planes in the combustion chamber

4.2. APPLICABILITY OF FLAMELET MODELS

4.2.1. STEADY FLAMELET MODEL

As the computation time with Eddy Dissipation Concept turbulence model is high as all the species transport equations are solved during the run time, flamelet approach seems a viable option where the species mass fractions and temperature are just functions of mixture fraction, scalar dissipation/progress variable. The theory behind using these approaches is elucidated in section 2.5.1. In this section the applicability of Steady Flamelet model is presented, followed by the application of Flamelet Generated Manifold.

The Steady Flamelet Model (SFM) in FLUENT can be accessed as a non-premixed combustion model option. For SFM the table containing the data for temperature and species mass fractions should be generated. In order to this two inputs are required. Firstly the chemical mechanism is required and for this purpose the same reaction mechanism of Chang et al. [65] for n-decane mentioned in previous chapter is used. The other input is the oxidizer stream and fuel stream boundary conditions which are given in table 4.1. After the boundary conditions, the flamelet is generated by varying the scalar dissipation rate from very small value ($\chi = 0.01$) until the flamelet is extinguished. After the generation of the flamelet the PDF table is generated with presumed PDF's for mixture fraction and scalar dissipation for the integration to obtain the species mass

Table 4.1: Boundary conditions for flamelet table generation

	Temperature (K)	Mass fraction (-)
Oxidizer	573	Y_{N_2}=0.768, Y_{O_2}=0.232
Fuel	310	$Y_{C_{10}H_{22}}$=1.0

fractions and temperature. After the generation of the table the gas phase and discrete phase coupled calculations are carried out. One thing to be noted is that unlike in the EDC model no temperature patch is needed as the combustion is determined from the scalar dissipation which is solved for.

The simulation resulted in combustion much upstream of the combustion chamber in the mixing chamber whereas measurements show that flame is only visible in the combustion chamber downstream of the mixing chamber. This is because in the mixing chamber there is intense mixing of incoming preheated air and the injected fuel. This well mixedness creates a small gradient in the mixture fraction Z. According to the definition of scalar dissipation (eqn. 4.1) which is also a measure of the departure from equilibrium, a small gradient in mixture fraction leads to small value of scalar dissipation rate.

$$\chi = 2D|Z|^2 \tag{4.1}$$

Smaller values of scalar dissipation means the process is closer to equilibrium and hence combustion is predicted. The SFM model with presumed PDF approach was used by Vaz et al. [67] and they also observed this kind of behavior. Also, in the SFM method, the deeper non-equilibrium effects of ignition and mixing effects are not included and upstream of combustion chamber there is only mixing without ignition and hence this non-equlibrium effect needs to be considered (Fig. 2.4, red lines). These effects can be captured by building Flamelet Generated Manifold (FGM) where flamelets are generated from mixing until equilibrium and is discussed below.

4.2.2. FLAMELET GENERATED MANIFOLD

In contrast to Steady Flamelet method, the FGM model is parameterized by reaction progress which is equal to zero in the unburnt mixture and one in burnt state. The progress variable in FLUENT for hydrocarbon flames is defined in terms of evolution of CO and CO_2. The FGM table is generated with the boundary conditions given in table 4.1. The flamelets are solved in the reaction progress space at different mixture fractions and are tabulated as function of progress variable and mixture fraction. FGM involves solving a transport equation for the mixture fraction and its variance and for un-normalized progress variable and its variance as given in eqn. 2.42a and eqn. 2.42b. After the generation of the table, the coupled simulation of gas phase and discrete phase are solved. It should be noted here that to initiate combustion a source term is required for the progress variable equation and thus a patch for the progress variable is used in FLUENT to initiate combustion. The calculations are carried out until there is no change in solution for successive iterations.

Fig. 4.11 shows the comparison of the measured and calculated radial profiles of the mean axial velocity from EDC and FGM combustion models with RSM turbulence model at different axial locations. The profiles are presented only for small droplet class ($0 < d \leq 5$). The calculated mean axial velocity from both combustion models agree well with the measured values at x = 4 mm. However, the calculated mean axial velocity at x = 44 and 72 mm are inaccurately predicted by the FGM model. This is due to the early heat release in the FGM model which can be seen through the temperature plot along the centerline for both the combustion models in Fig. 4.12. The flow exits the mixing pipe at high velocity and leads to high mixing in the shear layer of the impinging jet and because of this the chemical reactions are strongly delayed by reason of nonequilibrium effects even at high preheating temperatures [12]. The flamelet approach is based on the concept that

chemical time scales are very much shorter than the smallest flow time scale ($Da \gg 1$). But as the chemical reactions are delayed due to mixing at high velocity, when the FGM model is applied the chemical time scales predicted by the FGM model are closer to equilibrium than they are in reality and thus predict early heat release compared to EDC model [28]. This is corroborated by low computed Damköhler numbers shown on the mid plane of the combustion chamber in Fig. 4.13. When the computed Damköhler number is located in the Borghi diagram it corresponds to distributed reaction zone and not the flamelet regime [4]. Therefore, as the finite rate effects are important in this type of combustor, the use of FGM method (the variant implemented in ANSYS FLUENT) is not suitable and further results of FGM method will not be discussed.
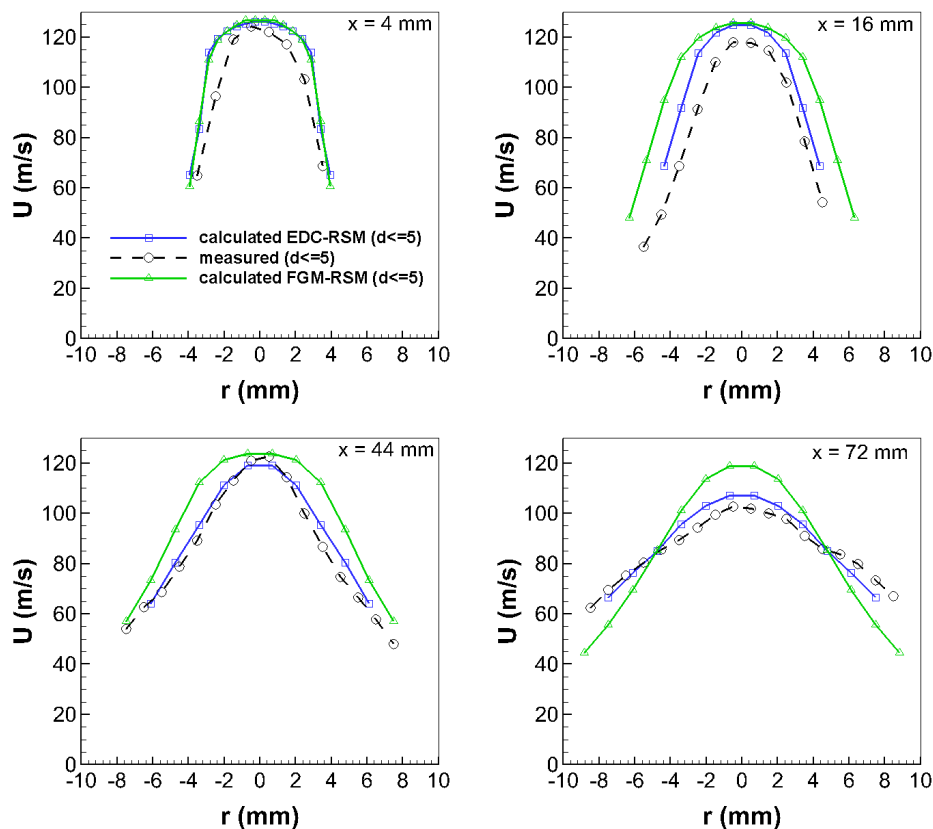

Figure 4.11: Comparison of measured and calculated radial profiles of the mean axial velocity from EDC and FGM combustion models with RSM turbulence model at different axial locations

4.3. EFFECT OF TURBULENCE TWO-WAY COUPLING

In FLUENT and SPRAYSIM, the basic form of two-way coupling only includes the exchange of mean quantities of mass, momentum and energy between continuous and discrete phase. But introduction of droplets in the carrier phase also affects the carrier phase turbulence and for accurate predictions this has to be taken into account (i.e, the droplet source terms should appear in the model equations of the employed turbulence models). In this section the effect of turbulence two-way coupling is presented with $k - \epsilon$ turbulence model as only $k - \epsilon$ models are provided with this option in FLUENT. Fig. 4.14 shows the evaporation progress with and without turbulence two-way coupling. It can be seen that the evaporation progress for without two-way coupling is higher than that with two-way coupling (from x > -90 mm). This is because of the damping of the turbulence intensity through turbulent kinetic energy by small particles in the carrier phase. When the
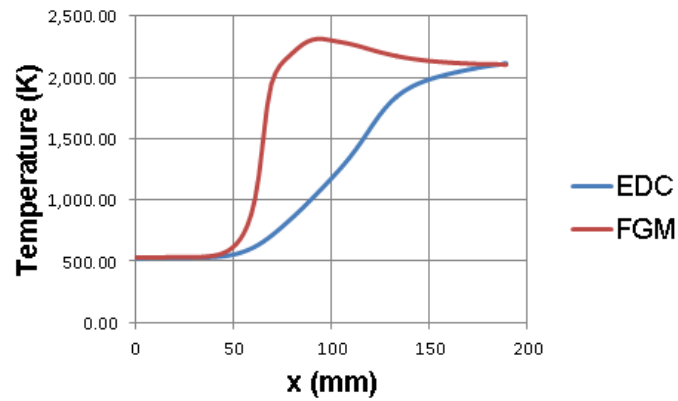
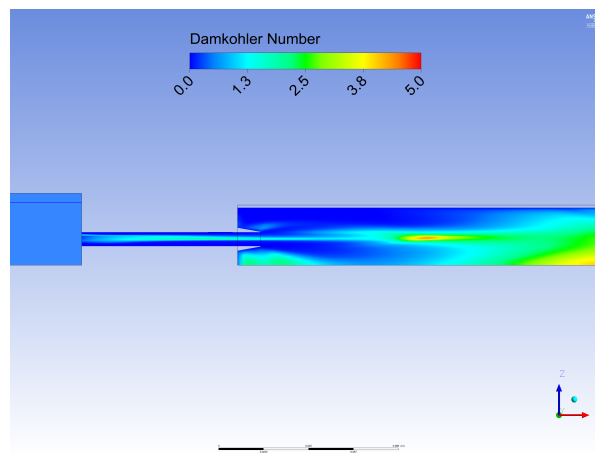Figure 4.12: Calculated temperature evolution along centerline of nozzle #6

Figure 4.13: Computed Damköhler number on the mid plane of the combustion chamber

turbulence intensity is reduced then the transport of mass from the droplet is reduced [68, 69]. The fuel vapor concentration gradient near the droplet surface is the driving force for evaporation. Reduced turbulent intensity near the droplet surface could lead to slower removal of fuel vapor near the droplet surface and thereby decrease the fuel vapor concentration gradient and evaporation rate. Reduced turbulent intensity also leads to reduced mixing in the combustion chamber (x > 0 mm) which leads to lower fine structure volume in the EDC combustion model. This leads to slower heat release as can be seen in Fig. 4.15 where temperature is plotted along the centerline of the nozzle in the combustion chamber for $k - \epsilon$ model with and without turbulence two-way coupling. For reference the temperature profile from Reynolds Stress Model is also shown to indicate that the two-way coupling is providing better prediction of Reynolds stresses and capturing of the anisotropy effect to some extent [42]. From the heat release pattern shown in previous figure it can also be expected that the velocity field will also be different for with and without two way coupling. Fig. 4.17 shows the comparison of the measured and calculated radial profiles of the mean axial velocity with $k - \epsilon$ model with and without turbulence two-way coupling for $0 < d \leq 5\mu m$ droplet class. Because of the early heat release predicted with no turbulence two-way coupling the velocity profiles are affected and at x = 72 mm higher velocity is predicted along the centerline whereas the turbulent two-way coupled $k - \epsilon$ model behaves almost similar to the RSM model due to better prediction of Reynolds stresses and anisotropy. Further, the effect of turbulent two-way coupling on rms velocity profiles is shown in Fig. 4.16 only for two axial locations and as the turbulence intensity is reduced by the droplets the magnitude of the rms values is also seen to be slightly
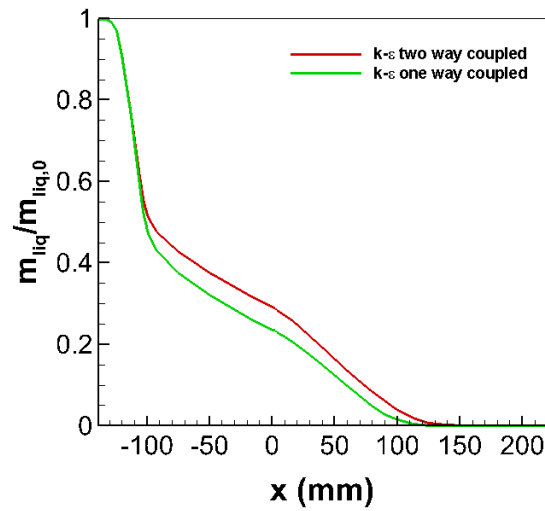
Figure 4.14: Evaporation progress for $k - \epsilon$ model with and without turbulence two-way coupling in turbulence quantities
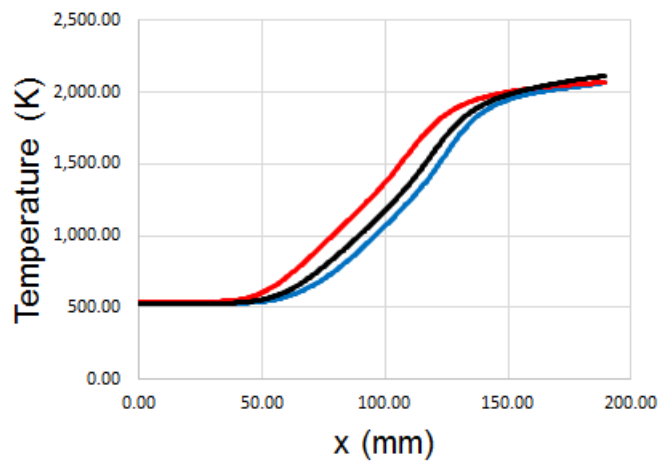
Figure 4.15: Evolution of temperature along centerline of nozzle for $k - \epsilon$ without two-way turbulence coupling: Red, with two-way turbulence coupling: Blue and RSM (without turbulence two-way coupling): Black

reduced in case of turbulent two-way coupling when compared to one-way coupled simulation. Further, the effect of turbulent two-way coupling on mean radial velocity is observed to be negligible and for rms velocity same behavior as that of axial rms values is seen.

Figure 4.16: Comparison of the measured and calculated radial profiles of the mean axial velocity with $k - \epsilon$ model with and without turbulence two-way coupling for $0 < d \leq 5\mu m$ droplet class

Figure 4.17: Comparison of the measured and calculated radial profiles of the axial rms velocity with $k - \epsilon$ model with and without turbulence two-way coupling for $0 < d \leq 5\mu m$ droplet class

4.4. Effect of Radiation

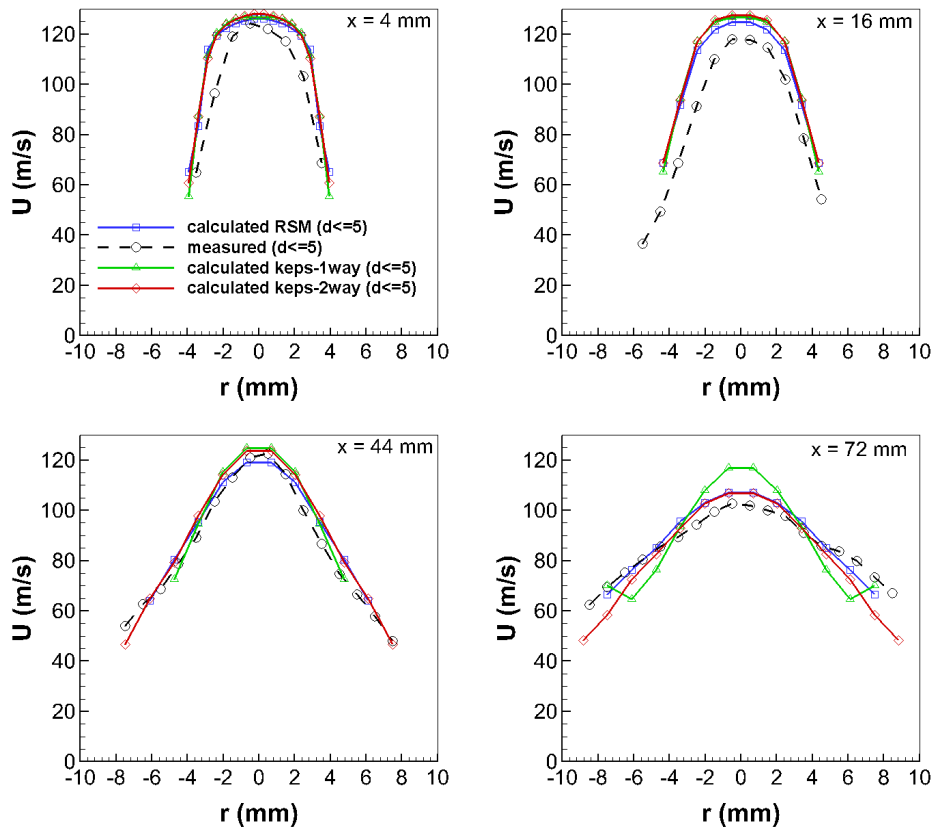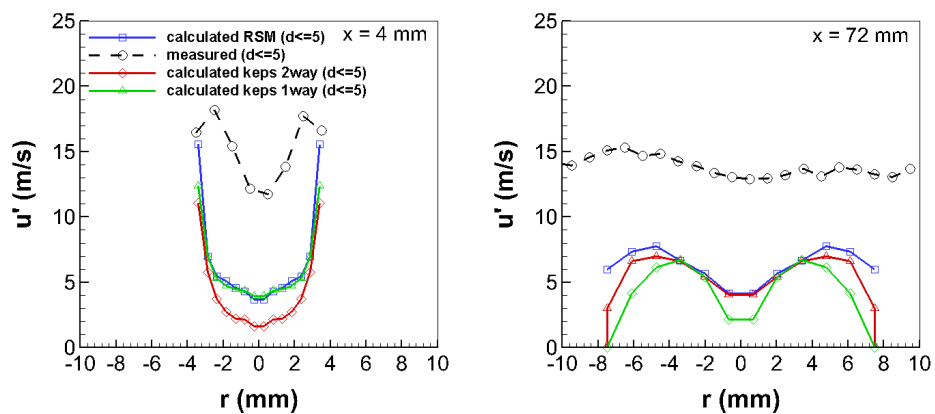Finally, the effect of radiation is considered. Generally, radiation affects the temperature field and thus the processes which are functions of temperature such as droplet evaporation, reaction also gets affected. But in this combustor where the dimension of the combustion chamber is small and is characterized by high bulk velocity and short residence times, radiation plays only a minor role in changing the temperature field [43, 69]. Considering the minor effect of radiation in this type of combustion just an approximate measure of computation of radiative transfer equation will suffice and to this end the computationally cheap and yet reasonably accurate P_1 method is applied. With the activation of P1 radiation model in FLUENT, the effect on the centerline temperature profile is negligible and only a reduction of maximum temperature in the combustion chamber by 30 K is achieved. As there is no soot emission calculation involved, the absorption of radiation energy by species such as CO_2, H_2O and CO is less compared to absorption by soot and hence the reduction in temperature is less as seen in the contour plot of temperature along the mid plane of the combustion chamber (Fig. 4.20). Therefore, the radiation effect can be neglected without loss of accuracy in the temperature profile.
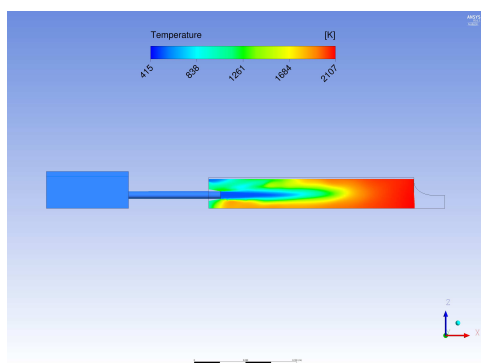

Figure 4.18: With radiation
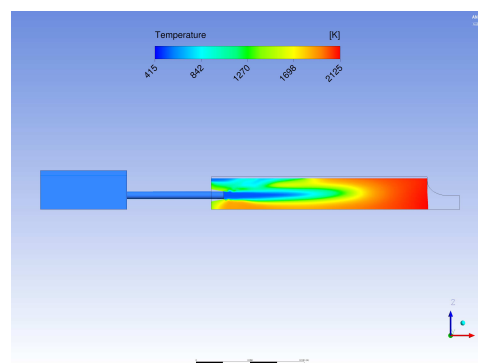
Figure 4.19: Without radiation

Figure 4.20: Contour plot of temperature on the mid plane of combustion chamber with and without radiation

4.5. Effect of Higher Air Preheat Temperature

Both experimental results and numerical results showed that the spray penetration length and thereby flame length lasts about two thirds of the combustion chamber. In going ahead with the development of the combustion chamber this long flame have to be shortened as this length influences the total length of the combustion chamber which preferentially should be small. One solution to resolve this issue is to increase the preheating temperature which will reduce the droplets' residence times in the combustion chamber and would lead to relatively shorter flames. For this purpose a simulation with EDC combustion model and RSM turbulence model was done. Mass flow boundary condition was the same as done in previous simulations. Higher air preheat temperature of 400°C was used instead of the current temperature of 300°C. Fig. 4.21 shows the comparison of evaporation progress with air preheat of 400°C and 300°C.

The evaporation progress in the mixing chamber is faster with 400°C compared to the other case as the preheat temperature is higher. The fraction of the liquid mass in this case was observed to be 0.0004 at x = 130 mm whereas with preheat of 300°C the fraction of the liquid mass present at x = 120 mm was 0.003. This
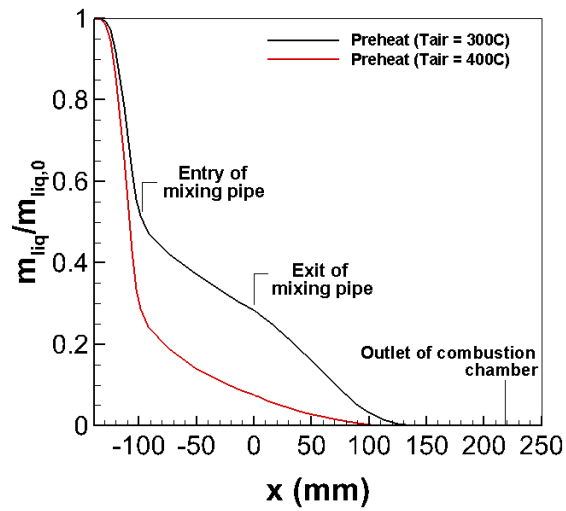
Figure 4.21: Comparison of evaporation progress with air preheat of $T_{air} = 400°C$ and air preheat of $T_{air} = 300°C$

shows that the spray penetration length is reduced considerably. The choice of increase in $100°C$ is judicious as an increase in $100°C$ can be obtained by using a recuperator to heat the combustion chamber inlet air. The result of this section provides a simple example of the use of CFD as a design tool in the development of the burner.

<div align="right">

5

</div>

CONCLUSION AND RECOMMENDATIONS

5.1. CONCLUSION

In this study, CFD simulations of the turbulent spray combustion of one of the nozzles of DLR Micro Gas Turbine was carried out in two different commercial codes: firstly, commercial code ANSYS CFX-16 coupled with the liquid phase code SPRAYSIM of DLR Institute of Combustion Technology, secondly with commercial code of ANSYS FLUENT-16 for both gas and liquid phase simulation. In the first stage of the work, for spray droplet size boundary condition a theoretical study of different empirical drop size distribution functions was made and as a result one of the widely used drop size distribution functions: Nukiyama-Tanasawa distribution function was implemented in the SPRAYSIM code of DLR Institute of Combustion Technology.

Further, the coupled two-phase steady state 3D RANS simulation was carried out using CFX and SPRAYSIM at 3.5 bar operating pressure and global equivalence ratio, $\lambda = 1.45$ with a two equation Shear Stress Transport (SST) turbulence model and with 1 step reaction kinetic. Combustion modeling was achieved through combined Eddy Dissipation and Finite Rate chemistry turbulence-chemistry interaction model and the obtained numerical results were validated with the experimental data obtained from the DLR test facility in Stuttgart. The simulation results helped in determining the amount of cooling air which is fed into the combustion chamber through a circumferential slot which was not measured during the measurement campaign. Further, the cold flow simulation showed that a large portion of evaporation happens in the mixing chamber upstream of the combustion chamber. However, it was observed that the spray penetration depth still spans almost $2/3^{rd}$ of the combustion chamber in agreement with the experimental findings. As a result of using 1-step chemistry and simple TCI model of combined eddy dissipation and finite rate chemistry (ED/FR), the simulation predicted early spatial heat release as early as in the mixing chamber and for this reason reacting flow simulation was done in the computational domain consisting only of the combustion chamber with boundary conditions for the two phases obtained from the cold flow simulation. The reacting flow simulation with simple combustion model and 1 step reaction scheme again showed early spatial heat release and mainly due to this the axial and radial velocity prediction was not sufficiently accurate compared to the experimental data.

The spray characteristics obtained with the CFX - SPRAYSIM simulation with simple combustion model pointed to the need for a better combustion model with detailed chemistry effects. Thus, in the next stage the

two-phase simulation was carried out in ANSYS FLUENT-16 with Eddy Dissipation Concept (EDC) turbulence-chemistry interaction model with detailed chemistry for gaseous phase fuel. Further, in order to isolate the effect of combustion model on spray characteristics prediction, two different turbulence models were used: 7 model equations Reynolds Stress transport Model (RSM) and 2 equation Shear Stress Transport (SST) model which was already used in the previous simulation. Results obtained from both RSM and SST model showed similar axial and radial velocity profiles at different axial locations and were in better agreement with the experimental data. However, RSM model slightly outperformed SST model in predicting better velocity profiles. The heat release from the EDC model measured through the nozzle centerline temperature profile showed that the temperature increase is gradual and spatially delayed as the chemical reactions are delayed by effect of nonequilibrium caused by the mixing of flow past nozzle at high velocity. In contrast, the combined ED/FR predicted early heat release and was unable to capture the nonequilibrium effects and as such affected the velocity profiles negatively. Further, both the calculated axial and radial rms velocity profiles agree qualitatively with the experimental data. However, the magnitude of both the calculated axial and radial rms velocity are under-predicted near the centerline of the jet and this might be due to the insufficient near wall mesh refinement of the boundary layer in the mixing pipe and also lack in predicting the transport of turbulent fluid across the centerline in a wall bounded turbulent jet flow.

Furthermore, the evaporation progress obtained through the simulations in FLUENT predicts slightly higher evaporation rate compared to the CFX-SPRAYSIM simulations. The evaporation model in FLUENT accounts for Stefan flow but without the thickening of the film around the droplet in contrast to the Abramzon-Sirignano model which is implemented in SPRAYSIM (leading to smaller Nusselt and Sherwood number and evaporation rate). Also, since the fuels used are slightly different (light heating oil- $C_{14.32}H_{25.75}$ in CFX and n-decane in FLUENT) the gas film properties may be different which will lead to different evaporation characteristics. The volume flux profiles obtained through the SST model in FLUENT emulates similar behavior as was obtained with the CFX simulation whereas with the RSM turbulence model the droplets were seen to accumulate near the centerline. This may be due to the geometry of the combustion chamber where the droplets accumulate at the center of the pipe at the pipe beginning. And since the particle fluctuation velocity is randomly sampled from the normal stresses in each direction for anisotropic turbulence, the stress in vertical direction is less compared to the axial direction and this might lead to droplet accumulation near the centerline. Lastly, the droplet characteristic diameters prediction from both the turbulence models were found to be fairly in good agreement with the experimental data but with better prediction of gas field the result could be more accurate.

Next, the application of flamelet concept was investigated by using nonpremixed Steady Flamelet Model (SFM) and partially premixed Flamelet Generated Manifold method with the Reynolds Stress Model for turbulence. With the SFM model it was observed that the combustion occurred in the mixing chamber and this was due to the inability of the SFM to capture deeper nonequilibrium effects of ignition and mixing. Consequently, the FGM method was applied which can take into account the nonequilibrium effects. Although FGM model predicted combustion only in the combustion chamber, it was however unable to predict chemical nonequlibrium effect and delayed spatial heat release resulting in higher centerline velocity. As the computed Damköhler number is close to unity (Da < 5) the finite rate chemistry effects are equally important. But the FGM model which assumes flamelet structure predicts the chemical time scale closer to the equilibrium and hence early spatial heat release. Therefore use of detailed reaction scheme with Eddy Dissipation Concept is justified in this type of FLOX combustor.

The effect of turbulent two-way coupling was investigated and it was found that the effect is not negligible and if possible it should be used. In CFX - SPRAYSIM the turbulent two way coupling was not used. In FLU-ENT turbulent two way coupling was only possible with the $k - \epsilon$ models. For this purpose two simulations

were carried out with $k - \epsilon$ turbulence model with and without turbulence two-way coupling. The two-way coupling leads to damping of carrier phase turbulent intensity by small droplets. As a result of reduced turbulence intensity the evaporation rate was reduced as it affects in the removal of the fuel vapor concentration buildup around the fuel droplet and thereby weakens the concentration gradient. Further, the $k - \epsilon$ model with no turbulent two-way coupling over-predicts turbulent kinetic energy and thus induces more mixing in the combustion chamber. Because of this well mixedness (bringing of more stoichiometric fuel/air mixtures) the heat release is enhanced and leads to higher centerline velocity. Whereas with the turbulent two-way coupled the turbulence intensity predicted is in accordance with the RSM model. Both RSM and $k - \epsilon$ predict similar centerline temperature profile leading to better velocity profiles. Additionally, the effect of radiation was included to assess its impact on combustion characteristics. As the combustion chamber is characterized by high bulk velocity and smaller residence times, in this work radiation effects play only a minor role. Thus P1 radiation model was used as it is computationally cheap and reasonably accurate. It was observed that the maximum temperature in the combustion chamber reduced by less than 30 K. Thus the effect of radiation can be neglected in this case. Finally, the spray penetration length as observed by both experiments and simulations was as long as two third of the combustion chamber. To reduce the spray penetration length higher air preheat temperatures were used in numerical simulations and it was found that the spray penetration length reduced roughly by 20 mm which is influential in having compact combustion chambers.

From this work it can be understood that the CFD simulation of turbulent spray combustion is a challenging task with lot of open ended questions which arise with different flow configurations. All the processes starting with evaporation, dispersion, turbulence, combustion and geometry are highly coupled and it is very difficult to isolate a single process and study its effect. However, for this case of FLOX combustor, a proper finite rate turbulence-chemistry interaction model with detailed chemistry is of significant importance and the choice of turbulence models does not greatly affect the result while complete two-way coupling of discrete phase and gas phase with all turbulence models can lead to more accurate results.

5.2. RECOMMENDATIONS

Finally some recommendations can be categorized into the following groups based on the work carried out in this thesis: based on accuracy, model improvement, design and experimental data.

- *Model improvement*:

  – A more generally applicable way of obtaining the spray boundary conditions based on flow parameters is necessary as the results are very much sensitive to the prescribed initial conditions. Also, the application of Maximum Entropy Formalism to define the drop size distribution is one of the avenue for further development of spray simulations and has to be looked into in more detail.

  – In this type of combustor where the particles come in contact with the walls, a droplet-wall interaction model has to be included to understand its effect on droplet trajectory.

  – In case of Reynolds Stress transport model, the current particle dispersion model is deficient in predicting the proper droplet dispersion in anisotropic turbulence. Dispersion models which are based on time and direction correlation function can be used to predict the desired dispersion of particles.

- *Accuracy*:

– Deeper understanding of the flame structure can be studied with unsteady simulations such as LES where the large scale turbulent structures are resolved and it can give better prediction of mixing, temperature fluctuations which are essential in predicting accurate flame characteristics.

- *Experimental data*:

    – Temperature measurements are very much essential for validation of physical models and this data can clearly shed some light on current uncertainty present in the numerical models.

- *Design of the burner*:

    – As seen by the numerical simulations that higher air preheat temperatures are beneficial in containing the flame length and reducing combustion chamber length. While it is also beneficial in increasing the efficiency of the combustion process. Future work can be done by including recuperator which can provide the above benefits.

A

DERIVATION OF NUKIYAMA TANASAWA VOLUME AND CUMULATIVE DISTRIBUTION

The derivation of the volume based and cumulative volume distribution for Nukiyama-Tanasawa distribution is shown here. To derive these quantities the number based distribution defined in section. 2.8.2 as eqn. 2.89 is the starting point. Firstly, the normalizing constant a_N is derived. The number based distribution should satisfy the normalizing condition given as:

$$\int_0^\infty \frac{dN}{dD} dD = 1 \tag{A.1}$$

The number based definition of Nukiyama-Tanasawa distribution (eqn. 2.89) is substituted into eqn. A.1 which results in:

$$\int_0^\infty a_N D^p \exp\left(-\left(\frac{D}{D_{ref}}\right)^q\right) = 1 \tag{A.2}$$

By making the following variable change:

$$y = \left(\frac{D}{D_{ref}}\right)^q \qquad D = D_{ref} y^{\frac{1}{q}} \qquad dD = \frac{D_{ref}}{q} y^{\frac{1-q}{q}} dy \tag{A.3}$$

Substituting eqn. A.3 into eqn. A.2 and working out:

$$\frac{a_N D_{ref}^{p+1}}{q} \int_0^\infty y^{\frac{p+1-q}{q}} \exp\left(-y\right) dy = 1 \tag{A.4}$$

The normalizing constant is obtained by exploiting the definition of complete gamma function defined as:

$$\Gamma(z) = \int_0^\infty t^{z-1} e^{-t} dt \tag{A.5}$$

Comparing eqn. A.5 with eqn. A.4 gives:

$$t - 1 = \frac{p+1-q}{q} \qquad t = \frac{p+1}{q} \tag{A.6}$$

79

Consequently, the normalizing constant a_N and the number based distribution is obtained as:

$$a_N = \frac{q}{D_{ref}^{p+1} \Gamma\left(\frac{p+1}{q}\right)} \tag{A.7}$$

$$\frac{dN}{dD} = \frac{q}{D_{ref}^{p+1} \Gamma\left(\frac{p+1}{q}\right)} D^p \exp\left(-\left(\frac{D}{D_{ref}}\right)^q\right) \tag{A.8}$$

The volume based distribution is obtained by using the following definition for number based and volume based distribution:

$$\frac{dQ}{dD} = \frac{D^3 \frac{dN}{dD}}{\int_0^\infty D^3 \frac{dN}{dD} d\tilde{D}} \tag{A.9}$$

Substituting eqn. A.8 into eqn. A.11 gives:

$$\frac{dQ}{dD} = \frac{D^3 \frac{q}{D_{ref}^{p+1} \Gamma\left(\frac{p+1}{q}\right)} D^p \exp\left(-\left(\frac{D}{D_{ref}}\right)^q\right)}{\int_0^\infty D^3 \frac{q}{D_{ref}^{p+1} \Gamma\left(\frac{p+1}{q}\right)} D^p \exp\left(-\left(\frac{D}{D_{ref}}\right)^q\right)} \tag{A.10}$$

Making use of the definition of complete gamma function and the variable changes in eqn. A.3 the volume based distribution is obtained:

$$\frac{dQ}{dD} = \frac{q}{D_{ref}^{p+4} \Gamma\left(\frac{p+1}{q}\right)} D^{p+3} \exp\left(-\left(\frac{D}{D_{ref}}\right)^q\right) \tag{A.11}$$

The cumulative volume distribution is obtained by using the relation:

$$Q(D) = \int_0^D \frac{dQ}{dD} d\tilde{D} \tag{A.12}$$

Substituting the volume distribution obtained in eqn. A.11 into eqn. A.12 gives:

$$Q(D) = \int_0^D \frac{q}{D_{ref}^{p+4} \Gamma\left(\frac{p+1}{q}\right)} D^{p+3} \exp\left(-\left(\frac{D}{D_{ref}}\right)^q\right) d\tilde{D} \tag{A.13}$$

Again, making the variable change used in eqn. A.3 and changing the limits of integration accordingly gives the following relation:

$$Q(D) = \frac{1}{\Gamma\left(\frac{p+4}{q}\right)} \int_0^{\frac{D}{D_{ref}}} y^{\frac{p+4-q}{q}} \exp\left(-y\right) dy \tag{A.14}$$

Now, making use of the incomplete gamma function which is defined as:

$$P(a, D) = \frac{1}{\Gamma(a)} \int_0^D t^{z-1} e^{-t} dt \qquad (a > 0) \tag{A.15}$$

and comparing eqn. A.14 and eqn. A.15 gives:

$$a = \frac{p+4}{q} \tag{A.16}$$

Thus, the cumulative volume distribution is determined as:

$$Q(D) = P\left(\frac{p+4}{q}, \frac{D}{D_{ref}}\right) \tag{A.17}$$

BIBLIOGRAPHY

[1] *International Energy Agency,* https://www.iea.org/publications/freepublications/publication/key-world-energy-statistics-2015.html (2015), accessed: 2016-09-08.

[2] O. Lammel, H. Schütz, G. Schmitz, R. Lückerath, M. Stöhr, B. Noll, M. Aigner, M. Hase, and W. Krebs, *FLOX® combustion at high power density and high flame temperatures,* Journal of Engineering for Gas Turbines and Power **132**, 121503 (2010).

[3] A. De, E. Oldenhof, P. Sathiah, and D. Roekaerts, *Numerical simulation of Delft-Jet-in-Hot-Coflow (DJHC) flame using the eddy dissipation concept model for turbulence-chemistry interaction,* Flow Turbulence Combustion **87**, 537 (2011).

[4] T. Poinsot and D. Veynante, *Theretical and Numerical Combustion,* 2nd ed. (R. T. Edwards, 2005).

[5] F. Christodoulou, P. Giannakakis, and A. I. Kalfas, *Performance benefits of a portable hybrid micro-gas turbine power system for automotive applications,* Journal of Engineering for Gas Turbine and Power **133** (2011).

[6] M. Ehsani, Y. Gao, S. E. Gay, and A. Emadi, *Modern Electric, Hybrid Electric and Fuel Cell Vehicles* (CRC Press, 2005).

[7] *International Energy Outlook,* http://www.eia.gov/forecasts/ieo/transportation.cfm (2016), accessed: 2016-09-08.

[8] *Driving Range for the Model S Family,* https://www.tesla.com/nl_NL/blog/driving-range-model-s-family?redirect=no.

[9] *Usage of Micro gas turbine as range extender,* http://www.greencarcongress.com/2010/11/wrightspeed-20101109.html.

[10] *Micro Gas Turbine Range Extender by Bladon Jets,* http://www.bladonjets.com/applications/automotive/.

[11] S. M. Correa, *A review of NOx formation under gas-turbine combustion conditions,* Combustion Science and Technology **87**, 329 (1991).

[12] H. Schütz, R. Lückerath, T. Kretschmer, B. Noll, and M. Aigner, *Analysis of the pollutant formation in the FLOX® combustion,* Journal of Engineering for Gas Turbines and Power **130**, 011503 (2008).

[13] *FLOX® is a trademark of WS Wärmeprozesstechnik GmbH, Renningen, Germany,* .

[14] T. Roediger, O. Lammel, M. Aigner, C. Beck, and W. Krebs, *Part-load operation of a piloted flox® combustion system,* Journal of Engineering for Gas Turbines and Power **135**, 031503 (2013).

[15] A. Zizin, O. Lammel, M. Severin, H. Ax, and M. Aigner, *Development of a jet-stabilized low-emission combustor for liquid fuels,* in *ASME Turbo Expo 2015: Turbine Technical Conference and Exposition,* 42642 (American Society of Mechanical Engineers, 2015).

[16] J. D. Gounder, A. Zizin, O. Lammel, and M. Aigner, *Spray characteristics measured in a new flox® based low emission combustor for liquid fuels using laser and optical diagnostics,* in *ASME Turbo Expo 2016: Turbomachinery Technical Conference and Exposition* (American Society of Mechanical Engineers, 2016) pp. V04AT04A036–V04AT04A036.

[17] J. Keller, M. Gebretsadik, P. Habisreuther, F. Turrini, and D. Zarzalis, N. Trimis, *Numerical and experimental investigation on droplet dynamics and dispersion of a jet engine injector,* International Journal of Multiphase Flow **75**, 144 (2015).

[18] N. Enjalbert, *Modelisation avancee de la combustion turbulente diphasique en regime de forte dilution par les gaz brules*, Ph.D. thesis, INSA de Rouen (2011).

[19] K. K. Kuo, *Principles of Combustion*, 2nd ed. (John Wiley & Sons, Inc., 2005) pp. 685–707.

[20] F. R. Menter, *Two-equation eddy-viscosity turbulence models for engineering applications,* AIAA journal **32**, 1598 (1994).

[21] S. B. Pope, *Turbulent Flows* (Cambridge University Press, 2000).

[22] B. F. Magnussen and B. H. Hjertager, *On mathematical modeling of turbulent combustion with special emphasis on soot formation and combustion,* in *Symposium (International) on Combustion*, Vol. 16 (1977) pp. 719–729.

[23] C. Yin, L. Rosendahl, S. K. Kær, S. Clausen, S. L. Hvid, and T. Hille, *Mathematical modeling and experimental study of biomass combustion in a thermal 108 MW grate-fired boiler,* Energy & Fuels **22**, 1380 (2008).

[24] *A chemical equilibrium program for Windows, version 0.79,* www.gaseq.co.uk. (2016).

[25] B. F. Magnussen, *On the structure of turbulence and a generalized eddy dissipation concept for chemical reaction in turbulent flow,* Nineteenth Aerospace Science Meeting (1981), 10.2514/6.1981-42.

[26] ANSYS, *ANSYS FUENT & CFX Theory Guide, 16.1* (SAS IP, Inc, 2016).

[27] N. Peters, *Laminar diffusion flamelet models in non-premixed turbulent combustion,* Progress in Energy Combustion and Science **10**, 319 (1984).

[28] S. Patil, J. Cooper, S. Orsino, J. Meadows, R. Valdes, and W. R. Laster, *Investigation of single-jet combustor near lean blowout conditions using Flamelet-Generated Manifold combustion model and detailed chemistry,* Journal of Engineering for Gas Turbines and Power **138**, 121503 (2016).

[29] L. Ma, *Computational Modeling of Turbulent Spray Combustion*, Ph.D. thesis, Delft University of Technology (2016).

[30] S. Zhu, D. Roekaerts, A. Pozarlik, and T. van der Meer, *Eulerian–lagrangian RANS model simulations of the NIST turbulent methanol spray flame,* Combustion Science and Technology **187**, 1110 (2015).

[31] J. Collazo, J. Porteiro, D. Patiño, J. L. Miguez, E. Granada, and J. Moran, *Simulation and experimental validation of a methanol burner,* Fuel **88**, 326 (2009).

[32] M. Lempke, P. Gerlinger, M. Rachner, and M. Aigner, *Steady and unsteady rans simulations of cryogenic rocket combustors,* in *49th AIAA Aerospace Sciences Meeting including the New Horizons Forum and Aerospace Exposition, AIAA-2011-101* (2011).

[33] L. Ma and D. Roekaerts, *Modeling of spray jet flame under MILD condition with non-adiabatic FGM and a new conditional droplet injection model,* Combustion and Flame **165**, 402 (2016).

[34] R. Clift, J. R. Grace, and M. E. Weber, *Bubbles, drops, and particles* (Academic Press, 1978).

[35] B. Abramzon and W. A. Sirignano, *Droplet vaporization model for spray combustion calculations,* International Journal of Heat and Mass Transfer **32**, 1605 (1989).

[36] S. S. Sazhin, *Advanced models of fuel droplet heating and evaporation,* Progress in energy and combustion science **32**, 162 (2006).

[37] D. R. Guildenbecher, C. Lòpez-Rivera, and P. E. Sojka, *Review on secondary atomization,* Experimental Fluids **46**, 371 (2009).

[38] F. X. Tanner, *A cascade atomization and drop breakup model for the simulation of high-pressure liquid jets,* SAE Technical Paper 2003-01-1044 , 231 (2003).

[39] J. S. Shirolkar, C. F. M. Coimbra, and M. Q. McQuay, *Fundamental aspects of modeling turbulent particle dispersion in dilute flows,* Progress in Energy Combustion Science **22**, 363 (1996).

[40] A. D. Gosman and E. Ioannides, *Aspects of computer simulation of liquid-fueled combustors,* AIAA Journal of Energy **7**, 480 (1983).

[41] E. Blümcke, M. Brandt, H. Eickhoff, and C. Hassa, *Particle dispersion in highly swirling, turbulent flows,* Part. Part. System Characterization **10**, 182 (1993).

[42] P. Jenny, D. Roekaerts, and N. Beishuizen, *Modeling of turbulent dilute spray combustion,* Progress in Energy and Combustion Science **38**, 846 (2012).

[43] R. Viskanta and M. Mengüç, *Radiation heat transfer in combustion systems,* Progress in Energy and Combustion Science **13**, 97 (1987).

[44] M. F. Modest, *Radiative heat transfer,* 3rd ed. (Academic press, 2013).

[45] L. Wang, *Detailed Chemistry, Soot and Radiation Calculations in Turbulent Reacting Flows,* Ph.D. thesis, Pennsylvania State University (2004).

[46] A. H. Lefebvre, *Atomization and Sprays,* 1st ed. (Hemisphere Publishing Corporation, 1989) pp. 79–103.

[47] P. González-Tello, F. Camacho, J. M. Vicaria, and P. A. González, *A modified Nukiyama–Tanasawa distribution function and a Rosin–Rammler model for the particle-size-distribution analysis,* Powder Technology **186**, 278 (2008).

[48] H. C. Simmons, *The correlation of drop-size distributions in fuel nozzle sprays, Part-I:the drop size/volume-fraction distribution,* Journal for Engineering for Power **99**, 309 (1977).

[49] J. S. Chin and A. H. Lefebvre, *Some comments on the characterization of drop-size distribution in sprays,* International Journal of Turbo and Jet Engines **3**, 293 (1986).

[50] J. C. Bhatia, J. Dominick, and F. Durst, *Phase-doppler-anemometry and the log-hyperbolic distribution applied to liquid sprays,* Part. Part. Sys. Charaterisation **5**, 153 (1988).

[51] E. Babinsky and P. E. Sojka, *Modeling drop size distributions,* Progress in Energy Combustion and Science **28**, 303 (2002).

[52] R. A. Mugele and H. D. Evans, *Droplet size distribution in sprays,* Industrial and Engineering Chemistry **43**, 1317 (1951).

[53] T. Paloposki, *Drop size distributions in liquid sprays* (Finnish Academy of Technology, 1994).

[54] T. Paloposki, *Drop size distribution in liquid sprays,* in *Proceedings of the 6th International Conference on Liquid Atomization and Spray Systems (ICLASS)*, ICLASS (1994) pp. 906–913.

[55] W. H. Press, S. A. Teukolsky, W. T. Vetterling, and B. P. Flannery, *Numerical Recipes in Fortran 77*, Vol. 1 (Cambridge University Press, 1997) pp. 209–213.

[56] J. Cousin, S. J. Yoon, and C. Dumouchel, *Coupling of classical linear theory and maximum entropy formalism for prediction of drop size distribution in sprays: Application to pressure swirl atomizers,* Atomization and Sprays **6**, 601 (1996).

[57] C. Dumouchel, *A new formulation of the maximum entropy formalism to model liquid spray drop-size distribution,* Part. Part. System Characterization **23**, 468 (2006).

[58] J. Zanger, T. Monz, and M. Aigner, *Experimental investigation of the combustion characteristics of a double-staged flox®-based combustor on an atmospheric and a micro gas turbine test rig,* ASME Pap. No. GT2015-42313 (2015).

[59] J. Boyde, P. Le Clercq, M. Di Domenico, M. Rachner, G. Gebel, T. Mosbach, and M. Aigner, *Validation of an ignition and flame propagation model for multiphase flows,* in *ASME 2011 Turbo Expo: Turbine Technical Conference and Exposition* (American Society of Mechanical Engineers, 2011) pp. 91–104.

[60] G. Eckel, M. Rachner, P. Le Clercq, and M. Aigner, *Semi-empirical model for the unsteady shear breakup of liquid jets in cross-flow,* Atomization and Sprays **26** (2016).

[61] B. Rauch, P. Le Clercq, M. Aigner, M. Rachner, R. Calabria, and P. Massoli, *Jet a-1 fuel spray evaporation in a turbulent flow: Experimental investigations and validation of numerical models,* in *Proceedings of the 49th AIAA Aerospace Sciences Meeting including the New Horizons Forum and Aerospace Exposition* (2011) pp. 4–7.

[62] A. H. Lefebvre and D. R. Ballal, *Gas Turbine Combustion*, 3rd ed. (CRC Press, Taylor & Francis Group, 2010) pp. 258–261.

[63] N. Ashgriz, *Handbook of Atomization and Sprays*, 1st ed. (Springer, 2011) pp. 685–707.

[64] T. Aumeier, *Die Anwendung eines probabilistischen Partikelmodells für die Modellierung der turbulenten Verbrennung in Brennkammern*, Ph.D. thesis, Universität Stuttgart, Institut für Verbrennungstechnik der Luft und Raumfahrt (2011).

[65] Y. Chang, M. Jia, Y. Liu, Y. Li, and M. Xie, *Development of a new skeletal mechanism for n-decane oxidation under engine-relevant conditions based on a decoupling methodology,* Combustion and Flame **160**, 1315 (2013).

[66] H. K. Versteeg and W. Malalasekera, *An introduction to computational fluid dynamics: the finite volume method,* 2nd ed. (Pearson Education, 2007).

[67] D. C. Vaz, A. R. Borges, J. P. van Buijtenen, and H. Spliethoff, *On the stability range of a cylindrical combustor for operation in the FLOX regime,* in *ASME Turbo Expo 2004: Power for Land, Sea, and Air* (American Society of Mechanical Engineers, 2004) pp. 511–516.

[68] M. Birouk and I. Gökalp, *Current status of droplet evaporation in turbulent flows,* Progress in Energy and Combustion Science **32**, 408 (2006).

[69] A. Sadiki, M. Chrigui, J. Janicka, and M. R. Masneshkarimi, *Modeling and simulation of effects of turbulence on vaporization, mixing and combustion of liquid-fuel sprays,* Flow, Turbulence and Combustion : **75**, 105 (2005).